ABSTRACT

Measurement of $b\bar{b}$ Production Correlations, $B^0\bar{B}^0$ Mixing, and a limit on the CP violating parameter ϵ_B in $p\bar{p}$ collisions at CDF

Intae Yu

Yale University

May 1996

In $p\bar{p}$ collisions at $\sqrt{s} = 1.8$ TeV, $b\bar{b}$ quark pairs are produced with a significant cross section. High momentum muons from semileptonic decays of bottom quarks can provide a data set for the studies of $b\bar{b}$ physics. Muons from bottom decays are distinguishable from others by their displaced trajectories resulting from the long lifetimes of bottom hadrons.

In this thesis, we have presented a measurement of correlated $b\bar{b}$ cross-sections, $\mu - \mu$ correlations, and the average $B^0\bar{B}^0$ mixing parameter $\bar{\chi}$, and a limit on the CP violating parameter ϵ_B, using dimuon events from $b\bar{b}$ double semileptonic decays. The data used were taken with the CDF detector during the 1992-1993 run of the Fermilab Tevatron and represent an integrated luminosity of $17.4 \pm 0.6pb^{-1}$.

The results concerning $b\bar{b}$ production correlations are compared to predictions of next-to-leading (NLO) order QCD computations. The normalization of the $b\bar{b}$ cross section is found to be higher than the theory prediction, which could be explained by adjusting the QCD input parameters. The distributions of the azimuthal opening angle and the muon transverse momentum obtained from the studies of $\mu - \mu$ correlations show reasonable agreement between data and NLO QCD theory.

A comparison between the number of $b\bar{b}$ events with like-sign and opposite-sign dimuons yields a value of the $B^0\bar{B}^0$ mixing parameter $\bar{\chi} = 0.131 \pm 0.020(stat) \pm 0.016(sys)$. In addition, the asymmetry between the number of $\mu^+\mu^+$ and $\mu^-\mu^-$ events is used to place a limit on the real part of ϵ_B which gives rise to CP violation in $B^0\bar{B}^0$ mixing.

Measurement of $b\bar{b}$ Production Correlations, $B^0\bar{B}^0$ Mixing, and a limit on the CP violating parameter ϵ_B in $p\bar{p}$ collisions at CDF

A Dissertation
Presented to the Faculty of the Graduate School
of
Yale University
in Candidacy for the Degree of
Doctor of Philosophy

By
Intae Yu

Dissertation Director: Michael P. Schmidt

May 1996

Acknowledgements

First of all, I would like to thank my advisor, Michael Schmidt, for all the valuable advice, help, and patience during my years at Yale.

I would also like to thank Jay Bao for everything he has given me over the years. He even taught me how to drive a car.

I thank the rest of the Yale CDF group, Karen Ohl, Randal Hans, Henry Kasha, and Steve Pappas for their support and advice.

I thank the members of my thesis committee, Charles Baltay, Steve Manly, Charles Sommerfield, and Richard Casten.

I thank many people at CDF, specifically the people who helped me to finish the thesis work: Lingfeng Song, Paris Sphicas, Jaechul Yun, Fritz Dejongh, Paul Derwent, Tae Song, William Wester, Todd Huffman, Robert Mattingly and many other people.

I thank many Korean friends at FNAL for their friendship and help.

Finally, I would like to thank my wife and my family for their love and affection during my academic carrier as a graduate student.

Contents

Acknowledgements ii

List of Figures vi

List of Tables x

1 Introduction 1

1.1 Standard Model 2

1.2 Heavy Quark Production 4

1.3 CKM Matrix 9

1.4 $B^0\bar{B}^0$ Mixing 10

1.5 CP asymmetry 12

2 The Experimental Apparatus 16

2.1 The Accelerator 16

2.2 Overview of CDF 17

2.3 Central Tracking Chamber 22

2.4 Silicon Vertex Detector 24

2.5 Central Muon Systems 27

2.6 Trigger System 32

3 Data Set 33

3.1 Data Collection 33

3.2 Sources of Muon Pairs 37

3.3 Offline Event Selection 41
3.4 Monte Carlo Data 44

4 Impact Parameter Fitting Method **45**
4.1 Impact Parameter 45
4.2 Impact Parameter Distribution 47
4.3 Two Dimensional Impact Parameter Fitting Method 57
4.4 Systematic Uncertainty in the Impact Parameter Fit 68

5 Central Muon Upgrade (CMP) Efficiency Method **72**
5.1 Principle 72
5.2 ϵ_μ 75
5.3 ϵ_f 78
5.4 Result 84

6 Total $b\bar{b}$ Cross Section **86**
6.1 $N_{b\bar{b}}$ 87
6.2 Acceptance 87
6.3 Efficiency 92
6.4 Result 94

7 $\mu - \mu$ Correlations **97**

8 Average $B^0\bar{B}^0$ Mixing Parameter **102**
8.1 Sequential Decays 102
8.2 Measurement 103

9 CP Violating Asymmetry **108**
9.1 Principle 108
9.2 Charge Asymmetry in Dimuon Data 109
9.3 Systematic Uncertainty in Charge Asymmetry 109
9.4 Result 111

10 Conclusion **115**

A Solutions of Dimuon Equations **117**

B $\mu - \mu$ Correlations from the MNR Calculation **119**

B.1 Introduction 119

B.2 Mapping 120

B.3 Result 127

Bibliography **130**

List of Figures

1.1 Feynman diagrams for the lowest order terms of heavy quark production. 6

1.2 Feynman diagrams for next-to-leading order terms of heavy quark production. 6

1.3 The differential cross section $d\sigma_{\mu\bar{b}}/dP_T(\bar{b})$ for $P_T(\mu) \geq 9$ GeV/c. . . . 7

1.4 The differential cross section $d\sigma_{\mu\bar{b}}/d\phi_(\mu\bar{b})$ for $P_T(\mu) \geq 9$ GeV/c and $E_T(\bar{b}) \geq 10$ GeV/c. 8

1.5 Feynman diagrams for $B^0\bar{B}^0$ mixing. 11

2.1 The layout of the Tevatron. 18

2.2 The CDF detector in isometric view 19

2.3 The CDF detector in cutaway view (quadrant). 20

2.4 An end view of the CTC endplate. 23

2.5 Isometric view of one barrel of the SVX detector. 25

2.6 One ladder of layer 2 of the SVX detector. 26

2.7 One wedge of the CMU detector. 28

2.8 Transverse projection of a charged particle track. 29

2.9 Coverage of the CDF muon detectors in $\eta - \phi$ space 30

3.1 Level 1 muon trigger efficiency as a function of P_T. 35

3.2 Level 2 muon trigger efficiency as a function of P_T. 36

3.3 Transverse momentum distribution for direct (dashed line) and sequential muons (solid line). 39

4.1 Definition of impact parameter. 46

4.2 The distribution of primary vertex resolution in x-y plane. 48
4.3 The SVX impact parameter distribution of jet tracks (solid line) and NoCMP muons (box) with $P_T \geq$3GeV/c. 51
4.4 The SVX impact parameter distribution of jet tracks (solid) and DIF muons (box) with $P_T \geq$3GeV/c. 52
4.5 The distribution of the SVX impact parameter resolution from jet data and Monte Carlo jet data with $P_T \geq$3GeV/c. 53
4.6 The SVX impact parameter distribution of bottom muons with $P_T \geq$3 GeV/c. 54
4.7 The SVX impact parameter distribution for direct B muons and sequential B muons with $P_T \geq$3GeV/c. 55
4.8 Impact parameter distributions of muons of various sources with $P_T \geq$ 3GeV/c. 58
4.9 Impact parameter distributions of bottom muons for each P_T bin. . . 59
4.10 Impact parameter distributions of charm muons for each P_T bin. . . 60
4.11 Impact parameter distributions of jet tracks for each P_T bin. 61
4.12 A two dimensional impact parameter distribution from dimuon data with $|d| \leq$ 1cm. 62
4.13 Two dimensional impact parameter distributions from data and each component. 64
4.14 The upper two plots are two dimensional distributions for each component. 65
4.15 The distribution from data and the contributions of each component from the fit. 66
4.16 Comparison between the projection of the data distribution (filled box) and that of sum of 3 components (solid line). 67

5.1 Normalized fractions of *real* dimuon (M) and fake dimuons (F_1 and F_2) as a function of the CMP efficiency for *fakes*, ϵ_f. 74
5.2 Distribution of dimuon invariant mass. 76
5.3 The CMP efficiency for *real* muons, ϵ_μ, as a function of P_T. 77

5.4 Invariant mass of a negatively charged muon and a positively charged track. 79
5.5 Invariant mass of a negatively charged muon and a positively charged track. 80
5.6 The CMP efficiency of pionic *fakes* from K_S^0 decays as a function of P_T. 81

6.1 Projections of the two dimensional impact parameter distributions for each data sample. 88
6.2 P_T distribution of $\bar{b}$ quarks decaying to μ with each P_T constraint on muon. 90
6.3 Rapidity, y, distribution of bottom quarks decaying to μ in the CMU/CMP fiducial region with $P_T \geq 3$ GeV/c. 91
6.4 Total $b\bar{b}$ cross section with $P_T(b) \geq 6.5$ GeV/c, $|y_b|, |y_{\bar{b}}| \leq 1$, and $P_T(\bar{b}) \geq P_T^{min}(\bar{b})$. 95

7.1 Opening angle distribution between $b\bar{b}$ muons. 98
7.2 $P_T(\mu_{\bar{b}})$ for $P_T(\mu_b) \geq 3$ GeV/c. 99
7.3 (Data-Theory)/Theory distributions of the opening angle between $b\bar{b}$ muons (top) and $P_T(\mu_{\bar{b}})$ (bottom). 100

8.1 Projections of the two dimensional impact parameter distributions in LS and OS events. 105
8.2 Comparison with measurements of $\bar{\chi}$ from other experiments. 106
8.3 χ_d vs χ_s. 107

9.1 Comparison between the data and fitted distributions in LS events. . 110
9.2 Level 1 trigger efficiency as a function of P_t. 112
9.3 Level 2 trigger efficiency as a function of P_t. 113
9.4 $\frac{Re\epsilon_d}{1+|\epsilon_d|^2}$ vs $\frac{Re\epsilon_s}{1+|\epsilon_s|^2}$. 114

B.1 The distribution of Z variable of the Peterson fragmentation. 121
B.2 Momentum of B hadron perpendicular to the quark direction. 122

B.3 Total momentum of muon in the rest frame of B hadron. 123
B.4 P_T of B hadron from the fragmentation mapping. 125
B.5 P_T of muon from the fragmentation and $B \rightarrow \mu$ decay mapping. . . . 126
B.6 Opening angle distributions between b muon and $\bar{b}$ muon with $P_T \geq$ 3 GeV/c for both muons. 128
B.7 P_T distribution for bottom muons with P_T of the other bottom muon $\geq$ 3 GeV/c. 129

List of Tables

1.1 Fundamental forces and force carriers. 3
1.2 Quarks and leptons. 3

3.1 Dimuon event selection cuts 43

4.1 Systematic uncertainties of the fit 70

5.1 Dimuon event selection cuts 73
5.2 K_S^0 reconstruction cuts 82
5.3 ϵ_{DIF} 83
5.4 Number of DIF muons after the selection 84

6.1 Fit results 87
6.2 Acceptance 89
6.3 Efficiencies 94
6.4 Systematics of the cross section measurement 94
6.5 Total $b\bar{b}$ Cross Sections 96

7.1 Dimuon cross section as a function of $\delta\phi_{\mu\mu}$ and $P_T(\mu_{\bar{b}})$. 101

8.1 Systematics of the measurement of $\bar{\chi}$ 104

Chapter 1

Introduction

The discovery of Υ in 1977 at Fermilab [1] and the realization that this meson is a $b\bar{b}$ bound state opened the field of b (bottom) physics, which since then has provided many important results for the understanding of the Standard Model of elementary particle physics. The t (top) quark, the weak isospin partner of the b quark, was recently discovered at Fermilab [2, 3], completing three generations of quarks required by the Standard Model.

At the Tevatron of the Fermi National Accelerator Laboratory (FNAL), protons collide with antiprotons with a center of mass energy ($\sqrt{s}$) of 1.8 TeV. In this range of energy, a center of mass energy for quark-antiquark collisions can be explored up to several hundred GeV, thus enabling studies of the b and t quark. In particular, $b\bar{b}$ quark pairs are produced with a large cross section ($\sim 30\mu$b) [5] and can be used to study many aspects of the Standard Model including heavy quark production, $B^0\bar{B}^0$ mixing, and CP violation.

Studies of the production of $b\bar{b}$ pairs provide an opportunity to test the perturbative theory of strong interactions. In $p\bar{p}$ collisions at $\sqrt{s} = 1.8$ TeV, the strong coupling constant, α_s, is small enough for heavy quark (c, b, t) production processes that perturbative Quantum Chromodynamics (QCD) is expected to provide reliable predictions. Measurements of $b\bar{b}$ production correlations play an important role in testing and understanding perturbative QCD.

$B\bar{B}$ hadron pairs generated by the fragmentation of $b\bar{b}$ quark pairs are expected

to exhibit many interesting phenomena via flavor-changing weak interactions, including $B^0\bar{B}^0$ mixing and CP violation. Measurements of $B^0\bar{B}^0$ mixing, where a neutral B meson transforms into its antiparticle, impose constraints on the elements of the quark mixing matrix – the Cabbibo-Kobayashi-Masakawa (CKM) matrix [4]. Studies of CP violation in the B system are of fundamental importance in understanding the origin of CP asymmetry within or beyond the Standard Model, which may explain the matter-antimatter asymmetry in current universe.

In this analysis, we report on measurements of $b\bar{b}$ production correlations, the $B^0\bar{B}^0$ mixing parameter, $\bar{\chi}$, and a limit on the real part of the CP asymmetry parameter, ϵ_B.

1.1 Standard Model

The interactions between particles are governed by four fundamental forces: strong, electromagnetic, weak, and gravitational. The strong, electromagnetic, and weak forces are all described by quantum field theories with local gauge invariance [6]. Local gauge invariance leads to a renormalizable quantum field theory where various unphysical infinities in the theory can be consistently eliminated. Gauge bosons which naturally arise in these theories are carriers of the interactions and their properties are listed in Table 1.1. A quantum field theory of gravitational forces has not been established but Einstein's field equations suggest the existence of the massless graviton, the carrier of gravity.

In addition to gauge bosons, there exist elementary fermions consisting of 6 quarks and 6 leptons. Quarks and leptons are building blocks of the universe and can be grouped into three generations (or families). The properties of quarks and leptons are listed in Table 1.2.

Electromagnetic forces are formulated by Quantum Electrodynamics (QED). QED is a local gauge theory where the symmetry group of gauge transformation is an unitary group in one dimension, $U(1)$. The gauge boson associated with an unbroken $U(1)$ symmetry is a massless spin-1 photon (γ). Weak forces are described by a gauge theory with the symmetry group $SU(2)$, an unitary unimodular group in two

Force carrier	Spin	Force	acts on
graviton	2	gravity	massive particles
photon (γ)	1	electromagnetic	electrically charged particles
$W^{\pm}$,Z	1	weak	quarks, leptons
gluon (g)	1	strong	quarks

Table 1.1: Fundamental forces and force carriers.

Charge	1st generation	2nd generation	3rd generation
		Quarks	
+2/3	up (u)	charm (c)	top (t)
−1/3	down (d)	strange (s)	bottom (b)
		Leptons	
−1	electron (e)	muon (μ)	tau (τ)
0	electron neutrino (ν_e)	muon neutrino (ν_μ)	tau neutrino (ν_τ)

Table 1.2: Quarks and leptons.

dimensions. Electromagnetic forces and weak forces are unified by the $SU(2) \times U(1)$ Glashow-Salam-Weinberg theory [7, 8, 9]. The combined symmetry is broken spontaneously in such a way as to retain renormalizability [10]. The gauge bosons resulting from the spontaneous symmetry breaking include the massive W^+, W^-, and Z bosons in addition to the massless photon.

Strong interactions are mediated by gluons (g), massless spin-1 bosons and act on quarks only. Quarks have an additional quantum number for strong interactions called *color*. There are three *colors* for quarks: red, blue, or green and three anti-*colors* for antiquarks: anti-red, anti-blue, or anti-green. Gluons have one *color* and one anti-*color* so that *color* is conserved at each quark-antiquark-gluon interaction. Colored quarks combine to form a hadron in such a way that the resulting particle is colorless (color confinement). The simplest quark configurations consist of the color singlet qqq state (baryon) and the color singlet state $q\bar{q}$ (meson), both of which correspond to physically observable particles. Quantum Chromodynamics (QCD) describes strong interactions with a local gauge theory where gauge transformations are

operating on *colors* with a SU(3) color symmetry group and the color octet of gauge bosons, the gluons, emerge.

Combining QCD and the electroweak theory, we have a $SU(3) \times SU(2) \times U(1)$ gauge invariant theory of strong and electroweak interactions, called the Standard Model. The Standard Model is the basic framework of current particle physics. For the past few decades, great progresses have been made in establishing the Standard Model, including the discovery of the W and Z bosons [11] and the recent discovery of the top quark [2, 3]. In the following sections, theoretical aspects of the Standard Model related to the analysis will be reviewed.

1.2 Heavy Quark Production

In high energy interactions of hadrons (mesons or baryons), the short distance cross section, corresponding to large momentum transfer, does not depend on the species of the incoming hadrons. The scattering process between two hadrons is the result of an interaction between the constituent quarks and gluons, which are collectively called partons. This factorization property [12] allows us to describe the cross section for heavy quark-antiquark production in hadron collisions as follows:

$$d\sigma^{h1,h2} = \sum_{i,j} \int dx_1 dx_2 d\sigma_{ij}(x_1 P_1, x_2 P_2, k_1, k_2, m, \mu) f_i^{h1}(x_1, \mu) f_j^{h2}(x_2, \mu) \qquad (1.1)$$

where x_1 and x_2 are the momentum fractions of partons in the incoming hadrons h_1 and h_2, f_i^{h1} (f_j^{h2}) is the parton distribution function for the ith (jth) parton in the incoming hadron h_1 (h_2) with momenta P_1 (P_2), $k_{1,2}$ are the momenta of the quark and antiquark, and m is the mass of the heavy quark. μ is the subtraction scale for removing divergences which arise in QCD [6]. $d\sigma_{ij}$ is the short distance parton-parton cross section for heavy quark production. The calculation of $d\sigma_{ij}$ can be performed by perturbative methods.

In QCD, the strong interactions between quarks and gluons are governed by a coupling constant, α_s. The renormalization properties of QCD reveal the coupling constant as a function of the momentum transfer of the interactions, q^2. One of the fundamental properties of QCD is the decrease of the strong coupling constant with

the momentum transfer q^2, a phenomenon known as asymptotic freedom. Specifically the coupling constant α_s can be written as:

$$\alpha_s = \frac{1}{B\log(q^2/\Lambda^2)} \tag{1.2}$$

where B is a constant and Λ is the parameter representing the scale at which the coupling constant becomes strong. In hadron collisions at sufficiently high energy ($q^2 \gg \Lambda^2$), the cross section σ_{ij} can be calculated as a power series expansion of the strong coupling constant α_s.

The heavy quark cross section has been calculated to next-to-leading order by Nason, Dawson and Ellis [13]. But their calculation has been carried out for only the inclusive production of a quark (b or $\bar{b}$) because of certain analytical difficulties arising from divergences [5]. Therefore all the information about the other quark and especially the other b quark is integrated out and lost. Mangano, Nason, and Ridolfi (MNR) [5] calculated the fully exclusive parton cross section for heavy quark-antiquark production at order of $O(\alpha_s^3)$ in QCD. The MNR method can be implemented using a Monte Carlo method, in which an event and the corresponding counter events are generated with the appropriate weight for the cancellation of the divergences [5].

The Feynman diagrams of the leading order and the next-to-leading order terms are shown in Figures 1.1 and 1.2. In the figures, we note that there are three different types of parton-parton interactions for heavy quark production : gg, gq, $q\bar{q}$. The gluon-gluon interaction (gg) is the dominant process in $b\bar{b}$ pair production and is responsible for about 90% of the total $b\bar{b}$ cross section [5].

The cross section for $b\bar{b}$ production in $p\bar{p}$ collisions has been measured by the UA1 [14] and CDF experiment [15] using various b quark decay modes. The result of the UA1 experiment ($\sqrt{s}$ = 630 GeV) agrees very well with the QCD theory at next-to-leading order. However, measurements at CDF ($\sqrt{s}$ = 1.8 TeV) [15] do not agree with the theory as shown in Figure 1.3 and 1.4. The most significant difference is the normalization of the cross section. The measured cross section is consistently higher than the theoretical prediction, which has been also observed in earlier CDF measurements of inclusive b cross section [16].

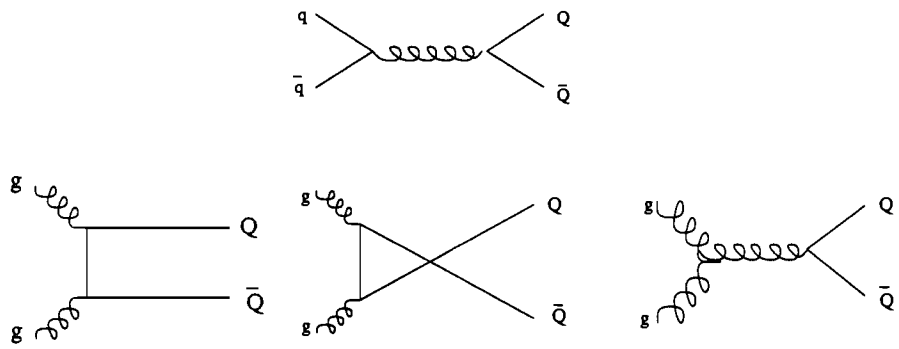

Figure 1.1: Feynman diagrams for the lowest order terms of heavy quark production.

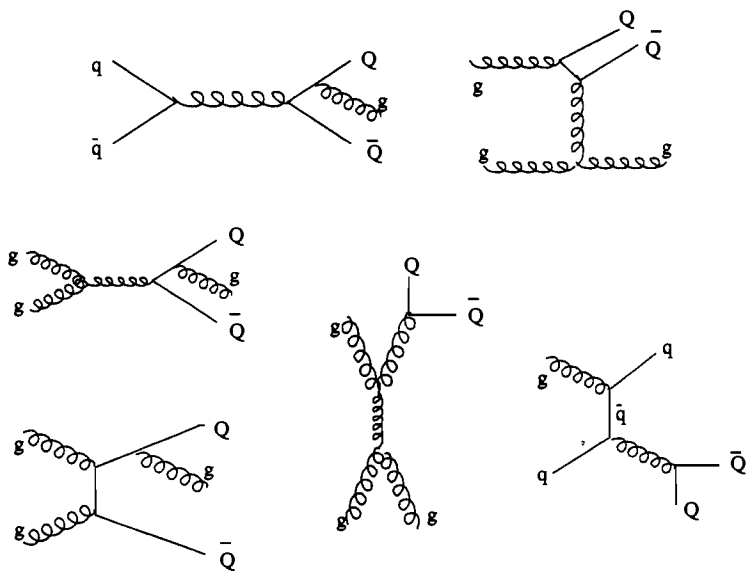

Figure 1.2: Feynman diagrams for next-to-leading order terms of heavy quark production.

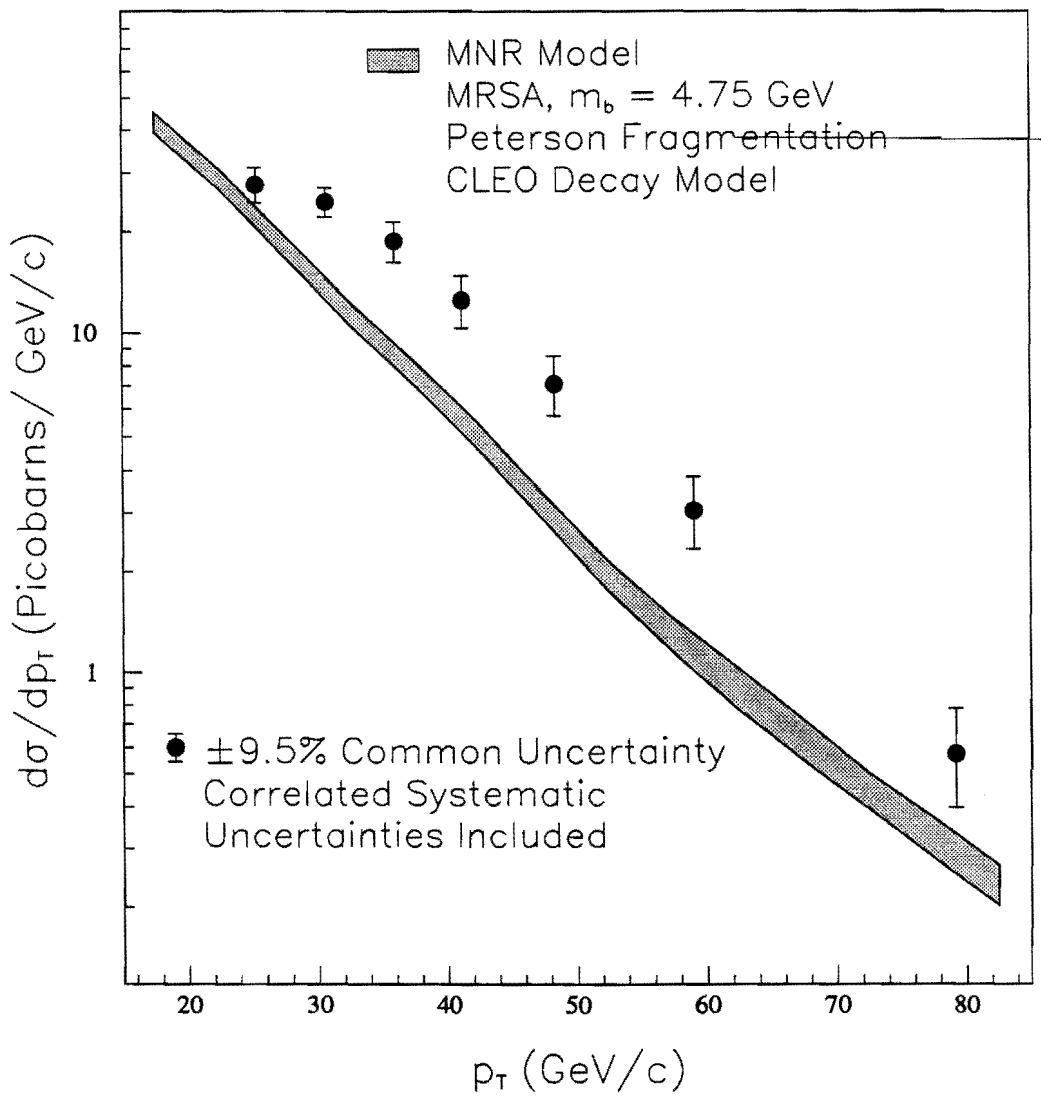

Figure 1.3: The differential cross section $d\sigma_{\bar{\mu}\bar{b}}/dP_T(\bar{b})$ for $P_T(\mu) \geq 9$ GeV/c. The uncertainty in the theoretical prediction results from the uncertainty in the branching ratio of $b \rightarrow \mu$ and the fragmentation uncertainty. The data used in the measurements was taken during the 1992-1993 CDF run at the Tevatron.

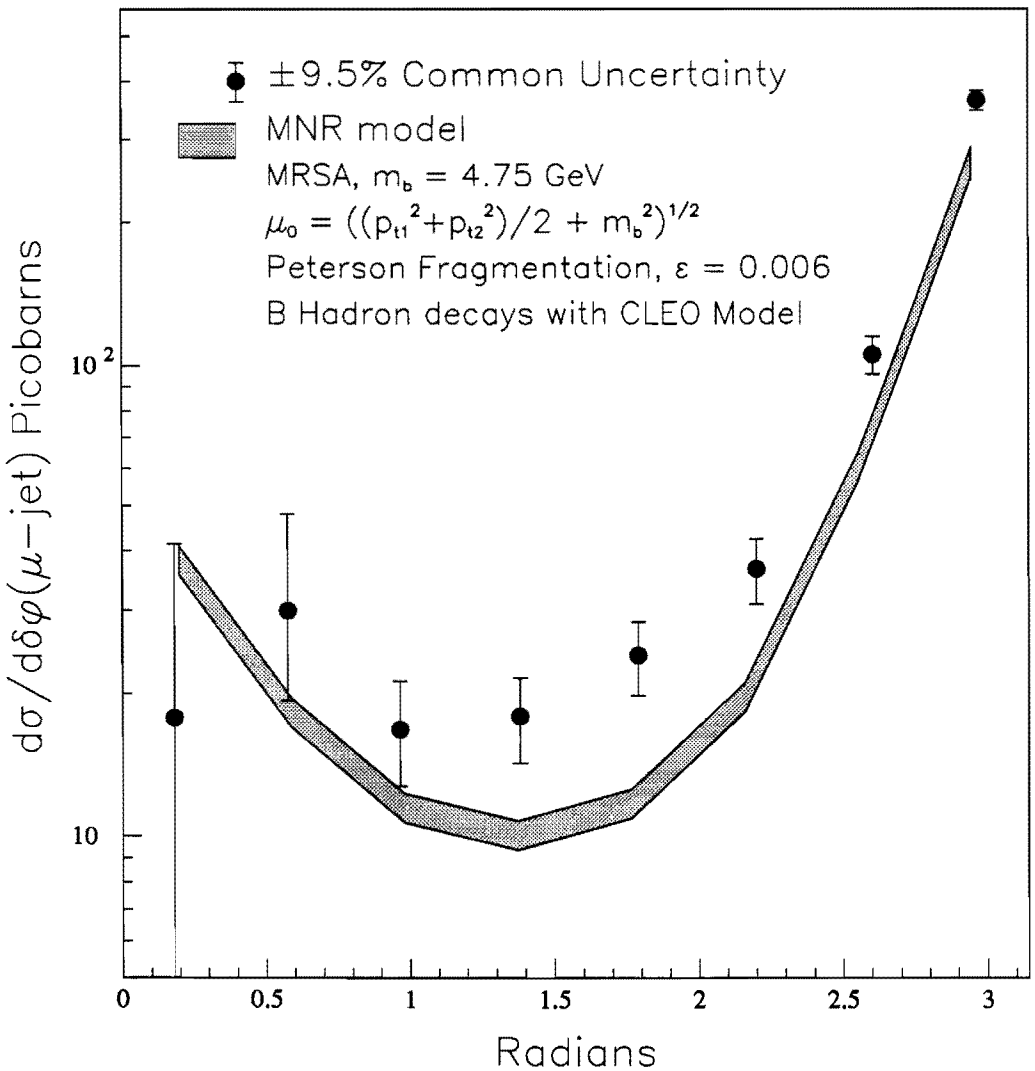

Figure 1.4: The differential cross section $d\sigma_{\mu\bar{b}}/d\phi_{(\mu\bar{b})}$ for $P_T(\mu) \geq 9$ GeV/c and $E_T(\bar{b}) \geq 10$ GeV/c. The uncertainty in the theoretical prediction results from the uncertainty in the branching ratio of $b \rightarrow \mu$ and the fragmentation uncertainty. The data used in the measurements was taken during the 1992-1993 CDF run at the Tevatron.

In this analysis, $b\bar{b}$ production in $p\bar{p}$ collisions at $\sqrt{s} = 1.8$ TeV is studied over different transverse momentum ranges for b and $\bar{b}$ quarks ($6 \sim 12$ GeV/c). The result provides important information on the production of $b\bar{b}$ pairs with relatively low transverse momentum and is complementary to previous CDF measurements [15]. The method and the results of the analysis on the $b\bar{b}$ production will be discussed in Chapters 6 and 7.

1.3 CKM Matrix

The quark mixing matrix plays a crucial role in understanding the electroweak sector of b physics including $B^0\bar{B}^0$ mixing and CP violation. In the Standard Model of three generations, the eigenstates of the weak interactions are *rotated* states of the flavor eigenstates. The unitary matrix, called the Cabbibo-Kobayashi-Maskawa (CKM) matrix [4], representing the *rotation* can be written as follows:

$$\begin{vmatrix} V_{ud} & V_{us} & V_{ub} \\ V_{cd} & V_{cs} & V_{cb} \\ V_{td} & V_{ts} & V_{tb} \end{vmatrix}$$

The nine complex matrix elements can be expressed as 18 parameters (9 real and 9 imaginary). However, unitarity and the freedom to choose the phase of the quark fields reduces the number of free parameters to four (3 real and 1 imaginary). Therefore, the CKM matrix can be parameterized as

$$\begin{vmatrix} 1-\lambda^2/2 & \lambda & A\lambda^3(\rho - i\eta) \\ -\lambda & 1-\lambda^2/2 & A\lambda^2 \\ A\lambda^3(1-\rho-i\eta) & -A\lambda^2 & 1 \end{vmatrix}$$

The above parameterization, suggested by Wolfenstein [17], is correct to terms of order λ^4 with $\lambda = \sin(\theta_c)$. The parameter θ_c, the Cabbibo angle [18], was originally proposed to account for the suppressed decay rate for $\Delta S = 1$ compared to $\Delta S = 0$ decay, where S represents the strangeness of hadrons, and is measured to be 0.2205 ± 0.0018 [19]. The determination of the other unknown parameters (A, ρ, and η) is required to fully define the Standard Model and may reveal an underlying structure

of new physics. We discuss $B^0\bar{B}^0$ mixing and CP violation which, in principle, can be used to constrain the unknown parameters of the CKM matrix.

1.4 $B^0\bar{B}^0$ Mixing

Measurements of $B^0\bar{B}^0$ mixing, where a neutral B meson transforms to its antiparticle or vice versa, provide a way to constrain the elements of the CKM matrix. The flavor eigenstates B^0 or $\bar{B}^0$ produced in strong or electromagnetic interactions are not eigenstates of weak interactions. The weak eigenstates of the neutral B mesons, B_1 and B_2, are linear combinations of B^0 and $\bar{B}^0$ as follows:

$$|B_1\rangle = \frac{1}{\sqrt{2}}(|B^0\rangle + |\bar{B}^0\rangle) \tag{1.3}$$

$$|B_2\rangle = \frac{1}{\sqrt{2}}(|B^0\rangle - |\bar{B}^0\rangle) \tag{1.4}$$

If a pure $|B^0\rangle$ state is produced at time $t = 0$, it will evolve into a new state which contains the $|\bar{B}^0\rangle$ state. The probability that $|B^0\rangle$ transforms to $|\bar{B}^0\rangle$ at time t is given by

$$P(B^0 \to \bar{B}^0)(t) = \frac{1 - \cos(\Delta M t)}{2} e^{-\Gamma t} \tag{1.5}$$

where ΔM $(= M_1 - M_2)$ is the difference between the masses of the weak eigenstates and Γ $(= (\Gamma_1 + \Gamma_2)/2)$ is the average of the widths of the two states. Integrating (1.5) over time, we obtain the time integrated mixing parameter, χ.

$$\chi = \int dt P(B^0 \to \bar{B}^0)(t) = \frac{1}{2}\frac{x^2}{1 + x^2} \tag{1.6}$$

where $x = \Delta M/\Gamma$ is the dimensionless mixing parameter.

In the Standard Model, $B^0\bar{B}^0$ mixing occurs via second-order W-exchange and the Feynman diagrams for these processes are shown in Figure 1.5. ΔM for $B^0\bar{B}^0$ mixing is calculated as

$$\Delta M_{d,s} = C_{d,s}|V_{tb}^* V_{td,ts}|^2 \tag{1.7}$$

where C represents the contributions of QCD corrections, the decay constant of the meson, the mass of top quark, and the weak coupling constant, and the subscripts d

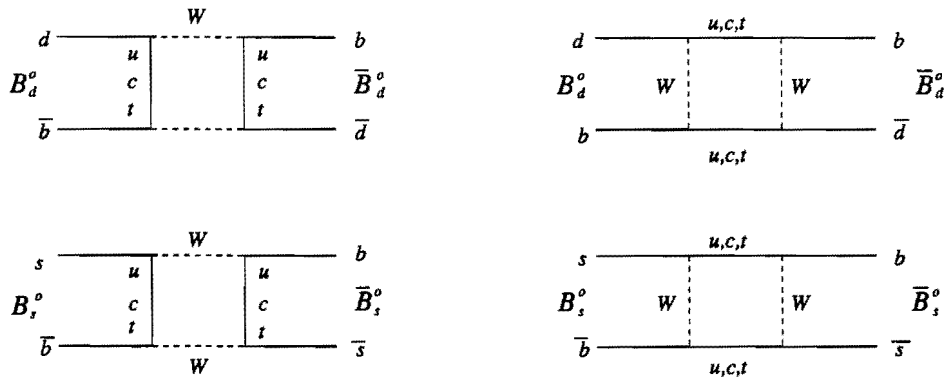

Figure 1.5: Feynman diagrams for $B^0\bar{B}^0$ mixing.

and s denotes the flavor of the neutral mesons. Since the determination of C involves poorly determined hadronic factors, a direct calculation of the CKM matrix elements V_{td} and V_{ts} from ΔM_d and ΔM_s may have large uncertainties. However, the ratio of ΔM_s and ΔM_d is expected to have a smaller uncertainty since many factors in C cancel out and the ratios of remaining factors are rather insensitive to the detailed hadronic structures. The ratio of ΔM_s and ΔM_d can be written as:

$$\frac{\Delta M_s}{\Delta M_d} = \frac{C_s}{C_d}|\frac{V_{ts}}{V_{td}}|^2 = (1.19 \pm 0.10) \times |\frac{V_{ts}}{V_{td}}|^2 \tag{1.8}$$

where the ratio of C_s and C_d has been taken from Reference [20]. Measurements of both $B_d^0\bar{B}_d^0$ and $B_s^0\bar{B}_s^0$ mixing would thus constrain the CKM matrix elements and, in turn, $|1-\rho-i\eta|$ in Wolfenstein parameterization.

The $B_d^0\bar{B}_d^0$ mixing parameter x_d has been measured in several experiments [21, 22, 23, 24, 25, 26] and is found to have the value of 0.71 ± 0.06 (world average) [27]. $B_s^0\bar{B}_s^0$ mixing has not been observed yet and is one of the goals of future high energy experiments. Several LEP experiments have obtained limits on the $B_s^0\bar{B}_s^0$ mixing parameter x_s and the most stringent limit is $x_s \geq 8.8$ from the ALEPH experiment [28].

Most of the experimental results on mixing have been reported from the study of lepton charge correlations, where leptons are from semileptonic decays of B mesons ($b \rightarrow lcX$). In the absence of mixing, the dual semileptonic decay of a $B\bar{B}$ pair results in an opposite-sign lepton pair. A $B\bar{B}$ pair where one of the mesons undergoes mixing

produces a like-sign lepton pair. Studies of the like-sign fraction in dilepton data lead to measurements of $B^0\bar{B}^0$ mixing.

In this analysis, dimuon events from double semileptonic decays of $B\bar{B}$ pairs are used to measure the time integrated mixing parameter $\bar{\chi}$, which is defined as follows:

$$\bar{\chi} = \frac{Prob(b \to \bar{B}^0 \to B^0 \to \mu^+)}{Prob(b \to \mu^\pm)} = f_d\chi_d + f_s\chi_s \tag{1.9}$$

where f_d and f_s are the fractions of B_d and B_s mesons respectively. A measurement of $\bar{\chi}$ gives a constraint on χ_s, χ_d, f_d, and f_s. The analysis and result will be discussed in Chapter 8.

1.5 CP asymmetry

CP violation, first observed in the neutral kaon system, is a fundamental phenomenon in the universe. Its origin is not well understood and many theoretical models [29] have been proposed to explain CP violation. In the Standard Model, CP violation can arise from a complex phase of the CKM matrix, η, since the Lagrangian of weak interactions between quarks is not Hermitian.

One of the consequences of CP violation expected in the B system is the different mixing probabilities for B^0 and $\bar{B}^0$, which results in a charge asymmetry of leptons from neutral B meson decays.

The proper time evolution of B^0 or $\bar{B}^0$ mesons created at time t=0 is given in the most general Pais-Treiman form [30] by

$$|B^0(t)\rangle = g_+(t)|B^0\rangle + \frac{q}{p}g_-(t)|\bar{B}^0\rangle) \tag{1.10}$$

$$|\bar{B}^0(t)\rangle = \frac{p}{q}g_-(t)|B^0\rangle + g_+(t)|\bar{B}^0\rangle) \tag{1.11}$$

$$g_\pm(t) = (e^{-i\alpha_1 t} \pm e^{-i\alpha_2 t})/2,\ q/p = (1-\epsilon_B)/(1+\epsilon_B)$$

where $\alpha_i = M_i - i\Gamma_i/2$ and ϵ_B is the CP violating parameter in the B system.

Charge correlations of leptons from neutral B meson decays can be used for the studies of CP violation in $B^0\bar{B}^0$ mixing. From (1.10) and (1.11), the amplitudes of

semileptonic decays for neutral B mesons at time t after production can be written as follows:

$$A(B^0 \to l^+) = \frac{\beta_1}{2}(e^{-i\alpha_1 t} + e^{-i\alpha_2 t}) \tag{1.12}$$

$$A(\bar{B}^0 \to l^+) = \frac{\beta_1 p}{2q}(e^{-i\alpha_1 t} - e^{-i\alpha_2 t}) \tag{1.13}$$

$$A(\bar{B}^0 \to l^-) = \frac{\beta_2}{2}(e^{-i\alpha_1 t} + e^{-i\alpha_2 t}) \tag{1.14}$$

$$A(B^0 \to l^-) = \frac{\beta_1 q}{2p}(e^{-i\alpha_1 t} - e^{-i\alpha_2 t}) \tag{1.15}$$

where β_1 and β_2 are matrix elements of the decays.

Assuming that $|\beta_1|^2 = |\beta_2|^2 = |\beta|^2$ and $(\Gamma_1 + \Gamma_2)/2 = 1/\tau$, the decay rates ($d\sigma/dt$ where $\sigma = |A|^2$) are

$$\frac{d\sigma}{dt}(B^0 \to l^+) = \frac{|\beta|^2}{2}e^{-t/\tau}(1 + cos(xt/\tau)) \tag{1.16}$$

$$\frac{d\sigma}{dt}(\bar{B}^0 \to l^+) = \frac{|\beta|^2|p|^2}{2|q|^2}e^{-t/\tau}(1 - cos(xt/\tau)) \tag{1.17}$$

$$\frac{d\sigma}{dt}(\bar{B}^0 \to l^-) = \frac{|\beta|^2}{2}e^{-t/\tau}(1 + cos(xt/\tau)) \tag{1.18}$$

$$\frac{d\sigma}{dt}(B^0 \to l^-) = \frac{|\beta|^2|q|^2}{2|p|^2}e^{-t/\tau}(1 - cos(xt/\tau)) \tag{1.19}$$

where $x = (M_1 - M_2)/\Gamma$.

Integrating the above expressions over time obtains:

$$\sigma(B^0 \to l^+) = \tau|\beta|^2(1 - \chi) \tag{1.20}$$

$$\sigma(\bar{B}^0 \to l^+) = \tau\frac{|\beta|^2|p|^2}{|q|^2}\chi \tag{1.21}$$

$$\sigma(\bar{B}^0 \to l^-) = \tau|\beta|^2(1 - \chi) \tag{1.22}$$

$$\sigma(B^0 \to l^-) = \tau\frac{|\beta|^2|q|^2}{|p|^2}\chi \tag{1.23}$$

where χ is the time integrated mixing parameter defined in Equation (1.6).

The decay probabilities for different lepton charges are expressed in the following way:

$$\sigma_+ = \tau|\beta|^2(1 + \frac{4\chi Re\epsilon_B}{1 + |\epsilon_B|^2}) \tag{1.24}$$

$$\sigma_- = \tau|\beta|^2(1 - \frac{4\chi Re\epsilon_B}{1+|\epsilon_B|^2}) \tag{1.25}$$

where $\sigma_+ = \sigma(B^0 \to l^+) + \sigma(\bar{B}^0 \to l^+)$ and $\sigma_- = \sigma(B^0 \to l^-) + \sigma(\bar{B}^0 \to l^-)$. From Equation (1.24) and (1.25), the charge asymmetry is directly calculated.

$$\frac{\sigma_+ - \sigma_-}{\sigma_+ + \sigma_-} = \frac{4\chi Re\epsilon}{1+|\epsilon|^2} \tag{1.26}$$

In real data, unless one is able to identify the flavor of B hadrons by reconstructing the daughter charm hadrons (for example, D^{*+}, D_s^+), the inclusive lepton data sample is a mixture of decays of various B hadrons. Therefore, the charge asymmetry should be written in the following way:

$$\frac{\sigma_+ - \sigma_-}{\sigma_+ + \sigma_-} = \frac{4f_d\chi_d Re\epsilon}{1+|\epsilon|^2} + \frac{4f_s\chi_s Re\epsilon}{1+|\epsilon|^2} \tag{1.27}$$

where f_d and f_s are the fractions of B_d^0 and B_s^0 and χ_d and χ_s are the corresponding mixing parameters.

In the dilepton data the charge asymmetry is expected to be larger than in the inclusive lepton sample since there are two leptons in an event. In order to obtain the correct expression of the charge asymmetry in dilepton events, we consider the sources of of l^+l^+ and l^-l^- pairs. In general, like-sign (LS) lepton pairs are from the process where one B meson is mixed and the other B meson is not mixed. If a mixed meson is $\bar{B}^0$, a l^+l^+ pair will be generated. The probability can be calculated by using Equation (1.20) and (1.21).

$$P(l^+l^+) = f_d\chi_d(1-\bar{\chi})(1 + \frac{4Re\epsilon_d}{1+|\epsilon_d|^2}) + f_s\chi_s(1-\bar{\chi})(1 + \frac{4Re\epsilon_s}{1+|\epsilon_s|^2}) \tag{1.28}$$

where $\bar{\chi} = f_d\chi_d + f_s\chi_s$ and $(1-\bar{\chi})$ is the probability of being unmixed. The above probability is normalized so that $P(l^+l^+) + P(l^-l^-) + P(l^+l^-) = 1$.
Likewise, for l^-l^- pairs,

$$P(l^-l^-) = f_d\chi_d(1-\bar{\chi})(1 - \frac{4Re\epsilon_d}{1+|\epsilon_d|^2}) + f_s\chi_s(1-\bar{\chi})(1 - \frac{4Re\epsilon_s}{1+|\epsilon_s|^2}) \tag{1.29}$$

The charge asymmetry in the dilepton data can be written in the following way:

$$\frac{P(l^+l^+) - P(l^-l^-)}{P(l^+l^+) + P(l^-l^-)} = \frac{8f_d\chi_d(1-\bar{\chi})}{D}\frac{Re\epsilon_d}{1+|\epsilon_d|^2} + \frac{8f_s\chi_s(1-\bar{\chi})}{D}\frac{Re\epsilon_s}{1+|\epsilon_s|^2} \tag{1.30}$$

$$D = 2\bar{\chi}(1 - \bar{\chi})$$

The Standard Model predicts ϵ_B to be approximately $10^{-3} \times \eta$ (the complex phase $\eta \sim O(1)$ from the Standard Model) [29]. However, some theoretical models on CP violation suggest larger values of ϵ_B [29].

A charge asymmetry in dimuons from double semileptonic decays of $B\bar{B}$ pairs is measured in this analysis. The method and the result will be described in Chapter 9. While the result obtained is not sensitive enough to reach the realm of Standard Model predictions, it serves as a search for contributions to CP violation in the B system from new physics. This study can also provide information useful for considering future studies of CP violation at hadron colliders.

Chapter 2

The Experimental Apparatus

The Collider Detector at Fermilab (CDF) [31] is one of two detectors built to study $p\bar{p}$ collisions at the Fermilab Tevatron. The Tevatron is currently the world's highest energy accelerator which collides protons with antiprotons at a center-of-mass energy of 1.8 TeV at Fermi National Accelerator Laboratory (FNAL). In this chapter, we will discuss the general features of the experimental apparatus and some details of detector components relevant to the analysis.

2.1 The Accelerator

Figure 2.1 shows the layout of the FNAL accelerator system. The proton beam begins life as a hydrogen ion beam from a magnetron surface-plasma source. Protons are accelerated by a Cockcroft-Walton preaccelerator, a linear accelerator (LINAC), and a synchrotron (Booster) in series to 8 GeV and then injected into the Main Ring [32]. The Main Ring is a proton synchrotron with a radius of 1000 m. It accelerates proton beam to 150 GeV. The boosted protons are then injected into the Tevatron, a superconducting proton synchrotron, which in turn boosts protons to 900 GeV.

Antiprotons are created by directing protons extracted from the Main Ring onto a nickel target. The Debuncher reduces the momentum spread of antiprotons and the transverse profile of the antiproton beam through stochastic cooling process [33] prior to the Accumulator. In the Accumulator, antiprotons are accumulated to make

a stack and cooled by additional stochastic cooling systems. When sufficient number of antiprotons are accumulated, they are injected into the Main Ring and then the Tevatron in the same way protons are injected, but rotating in the opposite direction.

Once protons and antiprotons are injected into the Tevatron and accelerated to 900 GeV, they continue to circulate for several hours at this energy and this is called a store. During a store, the Tevatron operates in a "six-on-six" mode where six bunches of protons and six bunches of antiprotons countercirculate in the ring. The bunch crossing time is about 3.5 μsec and the peak luminosity for 1992-1993 run was about $10^{31} sec^{-1} cm^{-2}$. There are two luminous regions (B0 and D0) where special superconducting quadrupoles squeeze the beams to $\sigma_{x,y} \sim 40\mu$m and focus them to produce $p\bar{p}$ collisions at a center-of-mass energy of 1.8 TeV. CDF is located at the B0 region as shown in Figure 2.1.

2.2 Overview of CDF

The Collider Detector at Fermilab (CDF) [31] is a general purpose detector built to measure the energy, momentum, and the identity of particles produced in $p\bar{p}$ collisions at the Tevatron Collider. Since the commissioning of the detector in 1987, it has been subsequently upgraded to study various physics such as bottom and top physics. Figures 2.2 and 2.3 show an isometric view and a quadrant view of the detector. In the CDF coordinate system, the beam axis is defined as the polar axis (or z axis). The pseudorapidity η, defined as $\eta = -\ln(\tan(\frac{\theta}{2}))$, is often used instead of the polar angle θ. Depending on η coverage, the detector is roughly divided into the central region ($|\eta| \leq 1.1$), plug region ($1.1 \leq |\eta| \leq 2.4$), and the forward region ($2.4 \leq |\eta| \leq 4.2$). In this chapter, we will briefly review the central detectors which are relevant to the analysis. The plug and forward detectors have been described in detail elsewhere [31].

Closest to the beam line, CDF has tracking detectors inside a superconducting solenoidal magnet with magnetic field of 1.4 Tesla. The tracking detectors reconstruct trajectories of charged particles within the detector. The curvature of a trajectory (to be called a track) inside a magnetic field measures the momentum of the charged

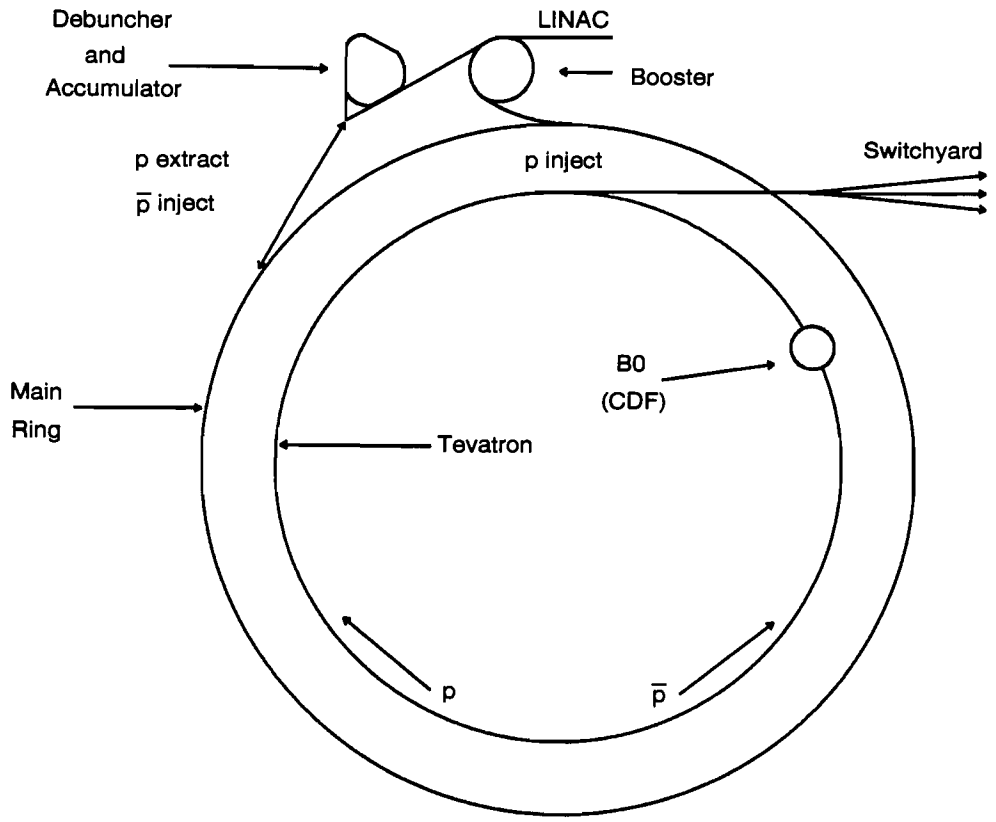

Figure 2.1: The layout of the Tevatron.

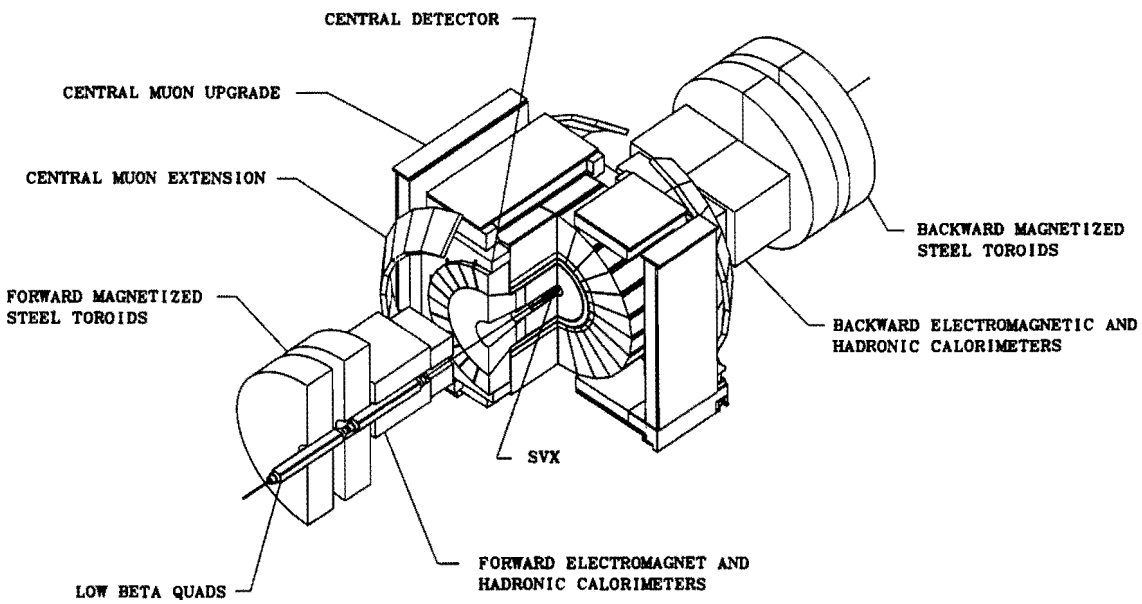

Figure 2.2: The CDF detector in isometric view

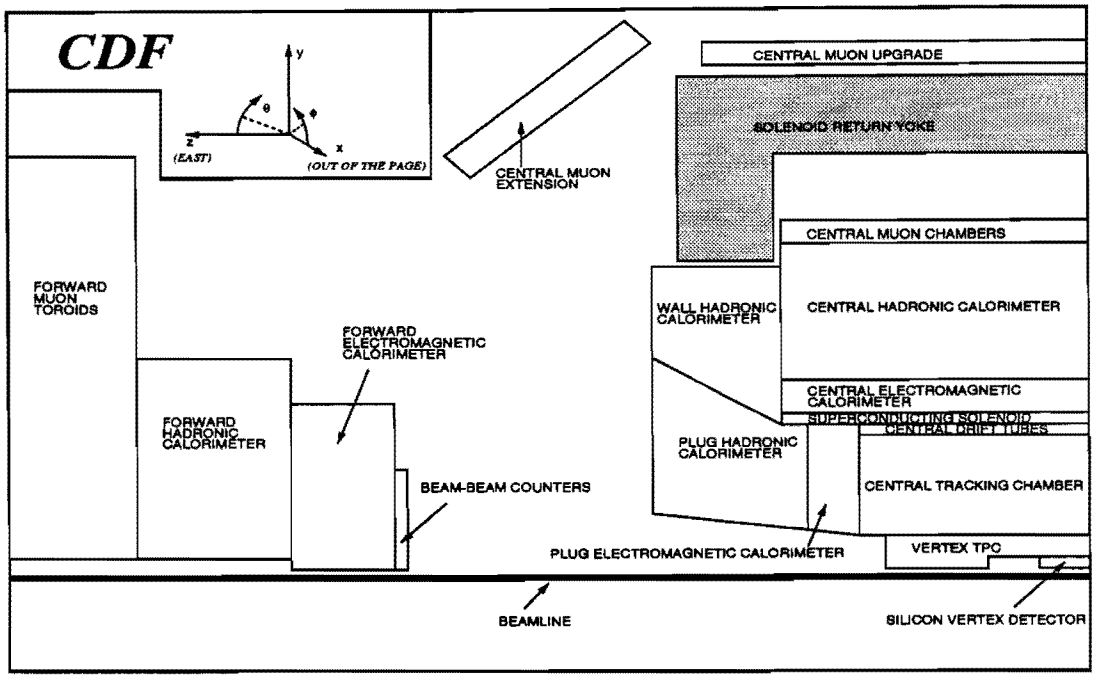

Figure 2.3: The CDF detector in cutaway view (quadrant).

particle. The central tracking system consists of 3 subdetectors: the Silicon VerteX detector (SVX) [34], the vertex tracking chamber (VTX), and the Central Tracking Chamber (CTC) [35].

The silicon vertex detector (SVX) consists of 4 layers of silicon vertex strip detectors designed to provide precision tracking in the $r - \phi$ plane. The SVX detector can be also used to find the displaced secondary vertex of B decays with good resolution (typically $\sim 20\mu$m in the $r - \phi$ plane for exclusive decays). The details of the SVX layout will be described in Chapter 2.4.

The vertex tracking chamber (VTX) is a time projection chamber consisting of 28 modules and covering the radial region from r=8cm to 50cm surrounding the SVX detector. At CDF, $p\bar{p}$ interactions are distributed along the beam axis with a Gaussian width of 26.65cm [36]. The VTX allows determination of the interaction vertex position in z with a resolution of 1mm.

The central tracking chamber (CTC) is a cylindrical drift chamber which provides a three dimensional tracking for charged particles. In CDF, the CTC is the main tracking chamber and reconstructed tracks in the CTC are extrapolated into the SVX detector to find the any corresponding tracks. The detailed description of the CTC will be found in Chapter 2.3.

Just outside the solenoid, the detector has central electromagnetic and hadronic calorimeters for a measurement of hadronic and electromagnetic energy. The calorimeters consist of projective towers uniformly segmented in $\eta - \phi$ space. Each tower points at the interaction region and is 0.1 units of η wide by 15° in ϕ in the central region.

The Central ElectroMagnetic calorimeter (CEM) [37] uses lead sheets as the absorber and scintillators as the active medium. Each tower of the electromagnetic calorimeter consists of a single longitudinal sample, where the lead sheets are interleaved with the scintillator layers. The light signal from the scintillator collected with acrylic light guides positioned at the corner of the tower is detected by photomultiplier tubes. The electromagnetic calorimeter measures electromagnetic energy of a charged particle with an energy resolution ($\sigma(E)/E$) of $13.5\%/\sqrt{E\sin(\theta)}$ (E in GeV).

The CEntral Strip chamber (CES) [37] is a proportional strip chamber used to determine the position and transverse development of electromagnetic shower. The CES chamber is located at a depth of 6 radiation length within the electromagnetic calorimeter volume in order to be sensitive to maximum shower development.

The Central HAdron calorimeter (CHA) [38] consists of 32 layers of steel plates alternated with scintillators. The total depth of the calorimeter is 4.7 absorption length and the calorimeter has a sufficient depth to contain 95% of hadronic shower at the energy of 50 GeV. For each tower light is collected by two symmetrically positioned light guides within the tower and detected by two photomultiplier tubes on opposite sides in azimuth. The hadron calorimeter measures hadronic energy with an resolution of $35\%/\sqrt{E} + 4\%$.

There are three central muon detectors in CDF, which measure muons penetrating the calorimeters. They are the Central MUon detector (CMU), the Central Muon uPgrade (CMP), and the Central Muon eXtension (CMX).

The central muon detector (CMU) [39] consists of 4 layers of drift chambers. The

chambers measure positions of a muon trajectory which serve to identify a muon and determine its momentum. The CMU detector is the primary system to detect muons in the central region ($|\eta| \leq 0.7$). Most of the muons pointing to the CMU detector are also detected by the central muon upgrade detector (CMP) [40] which was first installed just prior to the 1992-93 CDF run. Between the CMU and the CMP detector, there is a steel absorber to reduce hadronic punchthroughs in the CMP detector. The CMU and CMP detector will be described in Chapter 2.5. The central muon extension detector (CMX) covers the pseudorapidity region $0.7 \leq |\eta| \leq 1.0$.

CDF collects data using a three-level trigger system [41]. The first two levels consist of FASTBUS based trigger hardware [42] and Level 3 consists of software processor farm. The three-level CDF trigger selects events based on signatures expected from physics reducing the trigger rate at each level so that more sophisticated information can be used in the next level trigger. We will discuss the CDF trigger system in detail in Chapter 2.6.

2.3 Central Tracking Chamber

The central tracking chamber (CTC) [35] is a proportional wire chamber with an active radius of 1.4 m inside a solenoidal magnet with magnetic field of 1.4 Tesla. The CTC consists of 84 layers of sense wires grouped into 9 superlayers as shown in Figure 2.4. Five of these are axial superlayers in which the wires are parallel to the beam line.

Each axial superlayer contains 12 sense wire layers and provides $r - \phi$ information for trajectories of charged particles with a resolution of 150 μm per wire. Four stereo superlayers consisting of 6 sense wire layers are interleaved with axial superlayers, canted at $\pm 3°$ with respect to the beam line, which enables the determination of the $r - z$ position with a resolution of 3 mm.

The superlayers are divided into cells. The number of cells varies with each superlayer and is chosen so as to keep the maximum drift distance to be less than 40 mm corresponding to 800 nsec of drift time in drift field of 1350 V/cm. The cells are tilted by 45° with respect to the radial direction in order to compensate for the

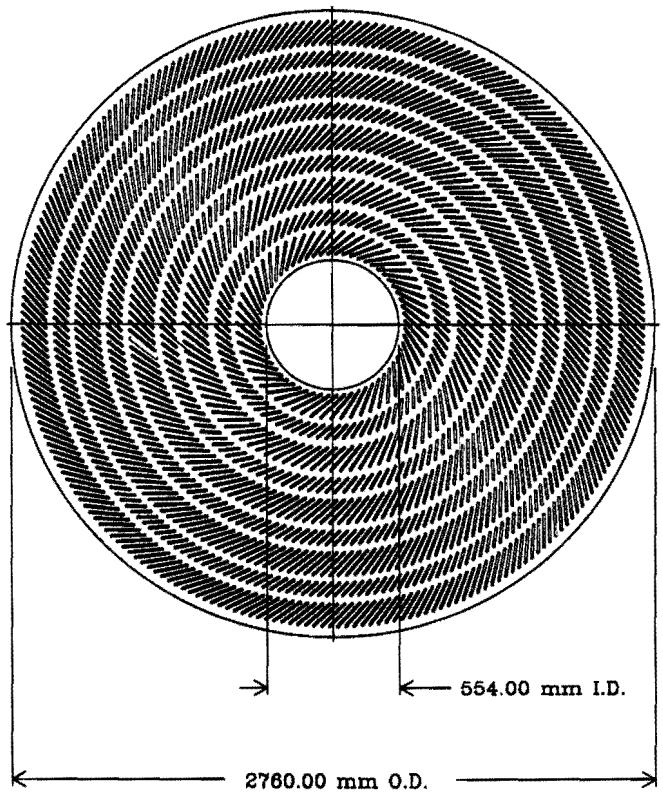

Figure 2.4: An end view of the CTC endplate.

crossed electric and magnetic fields and give the drift electrons nearly azimuthal trajectories.

The CTC provides information required for three dimensional tracking for charged particles. In an uniform magnetic field, a charged particle travels in a helical trajectory. The transverse momentum of a particle, P_T, is inversely proportional to the curvature of its trajectory in the transverse plane perpendicular to the magnetic field B as follows:

$$curvature = \frac{eB}{2P_T} \tag{2.1}$$

Tracks are reconstructed in the CTC using a pattern recognition algorithm by fitting the CTC hits to a trajectory of a helix. The transverse momentum resolution is found to be $\delta P_T/P_T \sim 0.002P_T$ (in GeV).

2.4 Silicon Vertex Detector

The silicon vertex detector (SVX) [34] is a single-sided silicon microstrip detector designed to provide precision tracking in the $r - \phi$ plane near the interaction point. The SVX detector consists of two axial barrels of equal length ($\sim$ 25.5cm) placed end to end along the beam axis with a gap of 2.15 cm between the barrels. The SVX detector contains about 60 % of $p\bar{p}$ interactions which occur along z in a Gaussian distribution with a width of 26.65cm. Each barrel consists of 4 concentric cylindrical layers covering radii from 3.005cm to 7.866cm and each layer has 12 ladders as shown in Figure 2.5. A ladder is a set of microstrip detectors which are p-n junction semiconductor devices. A charged particle generates an ionizing signal and if the junctions are reverse biased, the charge of an ionizing signal is collected on the localized strips. The strips are DC coupled to a customized readout chip at the end of the ladder (Figure 2.6). The detector in a ladder are glued to Rohacell, a lightweight polymethacrylimide foam, and carbon fiber support structures. The detector alignment with the above assembly has an rms of 4.5μm. In the innermost layer, the SVX detector can localize a hit of a charged particle with a spatial resolution of 13μm.

The track reconstruction algorithm in the SVX detector uses a *progressive method*

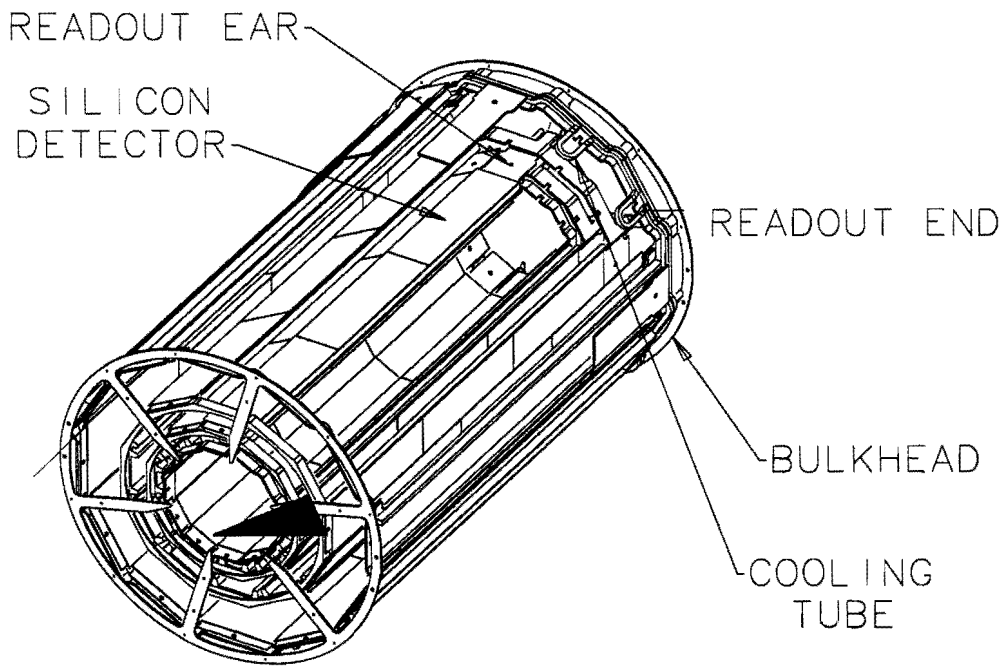

Figure 2.5: Isometric view of one barrel of the SVX detector.

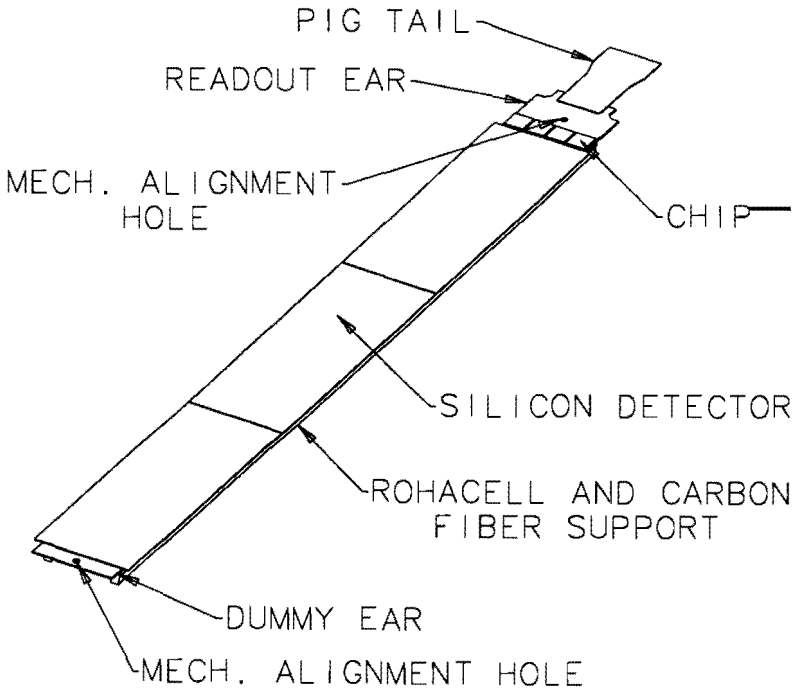

Figure 2.6: One ladder of layer 2 of the SVX detector.

[43] which starts from the CTC track fit results and improves the track fit progressively by adding SVX hit information and refitting as information is added from each of the 4 SVX layers. A reconstructed track in the CTC is extrapolated to the SVX detector along a road accounting for Coulomb multiple scattering and ionization loss. Within the road, a cluster of SVX hits is searched for and if a hit is found, the track parameters, the track error matrix, and the track χ^2 are updated. Track parameters representing a helical track are customarily $\cot(\theta)$, impact parameter, z, ϕ, and curvature. The track χ^2 of a SVX track is defined as

$$\chi^2 = \chi^2_{CTC} + (\vec{p}_{SVX} - \vec{p}_{CTC})^T C^{-1} (\vec{p}_{SVX} - \vec{p}_{CTC}) + \sum_{layer} \frac{(x_{track} - x_{cluster})^2}{\sigma^2_{cluster}} \quad (2.2)$$

where $\vec{p}$ is the vector of track parameters, C is the track covariance matrix including multiple scattering and ionization loss, x is the local coordinate on the SVX layer, and χ^2_{CTC} represents the χ^2 of the CTC track fit. The procedure is iterated until all SVX hits within the road are used. The best track candidate is selected based on the χ^2 of the final track fit. The errors of the track parameters are calculated from the error matrix. The uncertainty of the track parameters results from the intrinsic detector resolution, Coulomb multiple scattering, and the uncertainty of the beam position. The performance characteristics of the SVX detector relevant to the analysis will be described in detail in Chapter 4.1.

2.5 Central Muon Systems

The central muon detector (CMU) [39] is a drift chamber used to identify and determine the momentum of muons in the central region $|\eta| \leq 0.7$. The CMU is located at radius of 3.5 m just outside the central hadron calorimeter, separated from the interaction region by 4.9 hadronic absorption lengths. Muons are identified by their penetration of the central hadron calorimeter since they are minimum ionizing particles.

The CMU is segmented in 15° wedges in ϕ and each wedge is further segmented in ϕ into three modules as shown in Figure 2.7. Each wedge consists of 4 layers of 4 drift cells. A steel resistive sense wire with a radius of 50 μm is located at the center

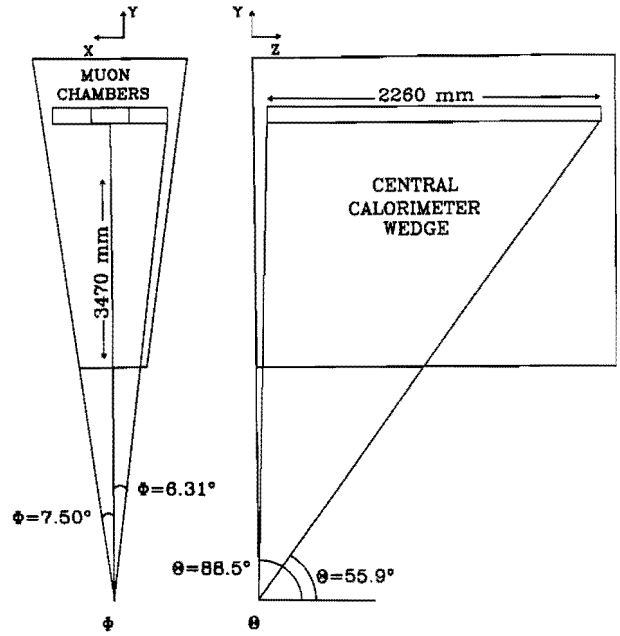

Figure 2.7: One wedge of the CMU detector.

of each cell.

The CMU uses drift time difference between layers for the measurement of $r - \phi$ information and charge division along the sense wires to determine z position. Figure 2.8 shows a transverse projection of a muon track. The angle α between a muon track and the radial line and β, the angle of deflection due to the magnetic field is related by the following equation.

$$D \sin(\alpha) = L \sin(\beta/2) \tag{2.3}$$

where $D = 3470$ mm is the distance from the interaction point to the bottom of the CMU and $L = 1440$ mm is the radius of the solenoidal magnetic field. The angle β can be related to the curvature of a track, 1/R, which in turn is related to the transverse momentum P_T as follows.

$$\sin(\beta/2) = \frac{L}{R} = \frac{eLB}{2P_T} \tag{2.4}$$

where B is the magnetic field. Combining the above two equations, the angle α can

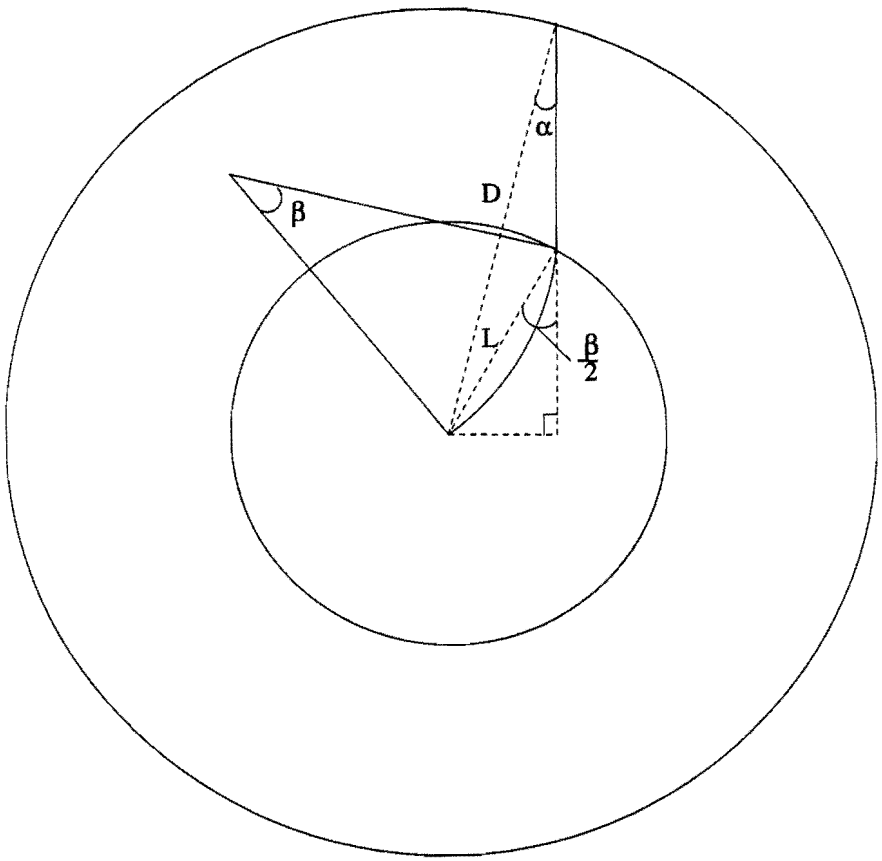

Figure 2.8: Transverse projection of a charged particle track. Within the inner circle of radius L = 1440mm is a 1.4T magnetic field. The outer circle of radius D = 3470 mm represents the bottom sense wire plane of the muon chamber.

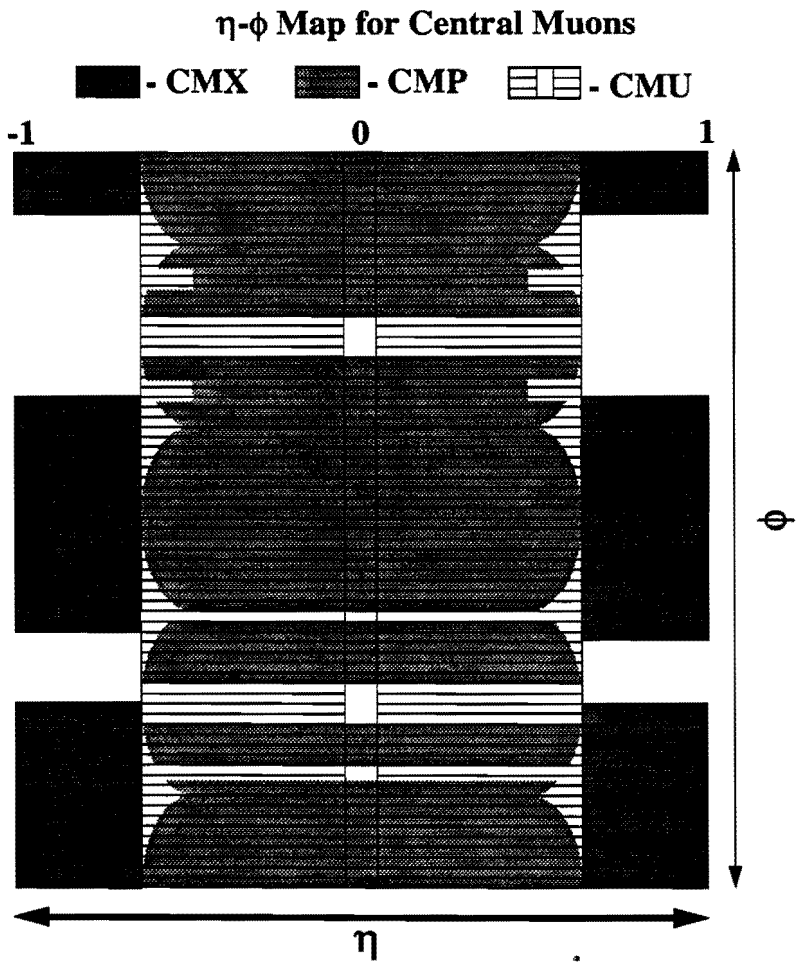

Figure 2.9: Coverage of the CDF muon detectors in $\eta - \phi$ space

be expressed as a function of P_T.

$$\alpha \approx \sin(\alpha) = \frac{eL^2B}{2DP_T} \tag{2.5}$$

The drift time difference for two sense wires in alternating layers, δt, is given by

$$\delta t = \frac{H\alpha}{v} \approx \frac{eL^2BH}{2DvP_T} \tag{2.6}$$

where $H = 55$ mm is the separation between the sense wires and v is the drift velocity of the ionization electrons. Therefore from the measurement of the drift time difference δt, the transverse momentum of a muon (P_T) can be measured. The CMU detector can measure muon P_T down to 1.4 GeV/c. The momentum resolution of the CMU detector is very crude ($\delta P_T/P_T \approx 0.6$) but adequate for triggers. If δt is less than a preset value in the trigger, a trigger signal is generated.

The central muon upgrade (CMP) [40] detects muons penetrating an additional 60 cm steel absorber ($\sim$ 3 absorption lengths) after the CMU detector. The CMU detector has an average of 5 absorption lengths from the interaction point and about 0.5% of hadrons traverses the calorimeters without interaction and fakes a muon in the CMU detector. The additional material between the CMU and the CMP detector reduces muon background from hadronic punchthroughs by a factor of 20. Therefore we can enhance the purity of reconstructed muon candidates with the CMP confirmation.

The CMP consists of rectangular drift chambers configured in 4 layers. The chambers are of fixed length in z ($\sim$ 6.4 m) and form a four sided box around the central detector, the pseudorapidity coverage varying with ϕ as shown in Figure 2.9. Because of additional multiple scattering, the minimum detectable muon P_T is 2.2 GeV in the CMP detector.

In CDF, muon candidates are identified by matching a track found in the CTC and a muon stub in the CMU or CMP detector. A track in the CTC is extrapolated to the muon chambers and associated with a muon stub with a set of matching requirements in $r - \phi$ and z which will be discussed in Chapter 3.3. The momentum of a muon candidate is determined by the kinematics of the associated CTC track.

2.6 Trigger System

The CDF trigger system [41] is designed to select interesting events resulting from physics processes. The interaction rate at the typical luminosity of $5 \times 10^{30} cm^{-2} sec^{-1}$ in the 1992-93 run is approximately 100 KHz with a particle multiplicity of 50 or more. In order to pick out events of interest, CDF uses a sophisticated three level trigger system. At each level, the trigger rate is reduced so that more information can be used for trigger decisions at the next level.

The first two levels consisting of sophisticated hardware systems make the trigger decision which initiates the readout of the full detector. The trigger hardware makes use of a FASTBUS system [42], mainly consisting of FASTBUS slaves.

The Level 1 system makes a decision in 3.5 μsec between beam crossings thereby incurring no deadtime. The trigger decision at Level 1 is based on information including total transverse energy ($E_T = E\sin(\theta)$), the existence of muon stubs in the muon detectors, and presence of beam-beam interactions. Specifically, as explained in Chapter 2.5, muon P_T thresholds can be applied to muon stubs at Level 1. Level 1 trigger signals from each part of the detector are combined to generate a global Level 1 trigger signal delivering a rate of a few KHz to the Level 2 system.

In Level 2, the trigger decision is made based upon information on energy clusters in the calorimeters, stiff tracks in the CTC associated with muon stubs, and transverse energy imbalance integrated over the detector. A set of Level 2 processors are used to calculate the above parameters. Specifically, a track processor, known as the central fast tracker (CFT) [44], calculates the P_T of a track using the CTC hit pattern. The Level 2 trigger delivers a rate of 10 Hz to the next level.

After an event passes Level 2, the readout of the detector components by the data acquisition system is initiated to reconstruct the event. The hardware Event Builder [45] collects the data from front-end electronics and writes complete event records to VME based processors in Level 3. The Level 3 system applies FORTRAN 77 based filter algorithms to fully reconstructed events and selects events of interest which are to be written to tape for subsequent physics analyses.

Chapter 3

Data Set

The data used in this analysis was taken with CDF during the 1992-1993 run of the Fermilab Tevatron Collider, called Run 1A. The total integrated luminosity of the data recorded at CDF during that period is about 20 pb^{-1}. The data has been processed for the reconstruction of events and classified into several standard data sets according to various physics purposes. The data we use for this analysis is a dimuon data set which contains events with low P_T dimuons. In this chapter, we will discuss the dimuon data set, starting from data collection, and ending with the restricted sample used in the analysis.

3.1 Data Collection

All of the CDF data originates from $p\bar{p}$ collisions at the Tevatron. The rate of $p\bar{p}$ interaction is represented by the instantaneous luminosity L, which is defined as follows:

$$L = \frac{BN_pN_{\bar{p}}}{4\pi\sigma^2} \tag{3.1}$$

where N_p and $N_{\bar{p}}$ are the number of protons and antiprotons per bunch and B is the bunch crossing rate, and σ is the width of the beam. The instantaneous luminosity L at CDF is measured with the Beam-Beam Counter (BBC) [46]. The BBC consists of two planes of scintillation counters covering the angular range of 0.32° to 4.47° in both the forward and backward directions as shown in Figure 2.3. Coincident hits in

both counters, in time with the passage of the bunches, serves as the primary luminosity monitor. The rate (number) of coincidences in these counters, divided by the effective cross section of the counters (σ_{BBC}), gives the instantaneous (integrated) luminosity. We measure the luminosity with a 3.6% uncertainty, which comes from the uncertainties in the measurements of σ_{BBC} and the luminosity-dependent performance of the BBC [47].

The CDF multi-level trigger system [41], as discussed in Chapter 2.6, selects events at an acceptable rate at each level so that CDF can analyze data without significant loss of events of interests. There are several different triggers at each trigger level for the selection of events for a variety of physics interests. A dimuon trigger is used to collect dimuon events from $p\bar{p}$ collisions.

The Level 1 dimuon trigger requires two muon segments to be found in the central muon detector (CMU) and the P_T of each segment to be greater than 3 GeV/c. At Level 1, the P_T of a muon segment is crudely measured using the drift time difference between layers in the CMU detector as explained in Chapter 2.5. Since the measurement of the transverse momentum of a muon with the CMU detector is not precise and the triggering is not perfect, some events which should be kept are lost. Figure 3.1 shows the Level 1 trigger efficiency as a function of muon P_T [48]. The efficiency is rising asymptotically and saturating at about 91.8 % for $P_T \geq 3$ GeV/c.

The Level 2 dimuon trigger requires at least one of two muon segments to match a track in the Central Tracking Chamber (CTC) found by the Central Fast Tracker (CFT) [44]. The CFT, a hardware track processor, uses fast hit information from the CTC and calculates the P_T of a track in the CTC with a resolution of $\delta P_T/P_T = 0.035P_T$. The Level 2 requires a match between a muon segment and a CTC track to be within 15° in ϕ and this matching requirement for a muon is almost 100 % efficient. Therefore the Level 2 dimuon trigger efficiency is entirely dependent upon the CFT efficiency which is plotted as a function of track P_T in Figure 3.2 [48]. The CFT efficiency shows a similar shape as the Level 1 trigger efficiency and has a saturation value of 92.5 % for $P_T \geq 3$ GeV/c. The trigger also requires the P_T of the muon segment matched by the CFT to a CTC track greater than 3 GeV/c.

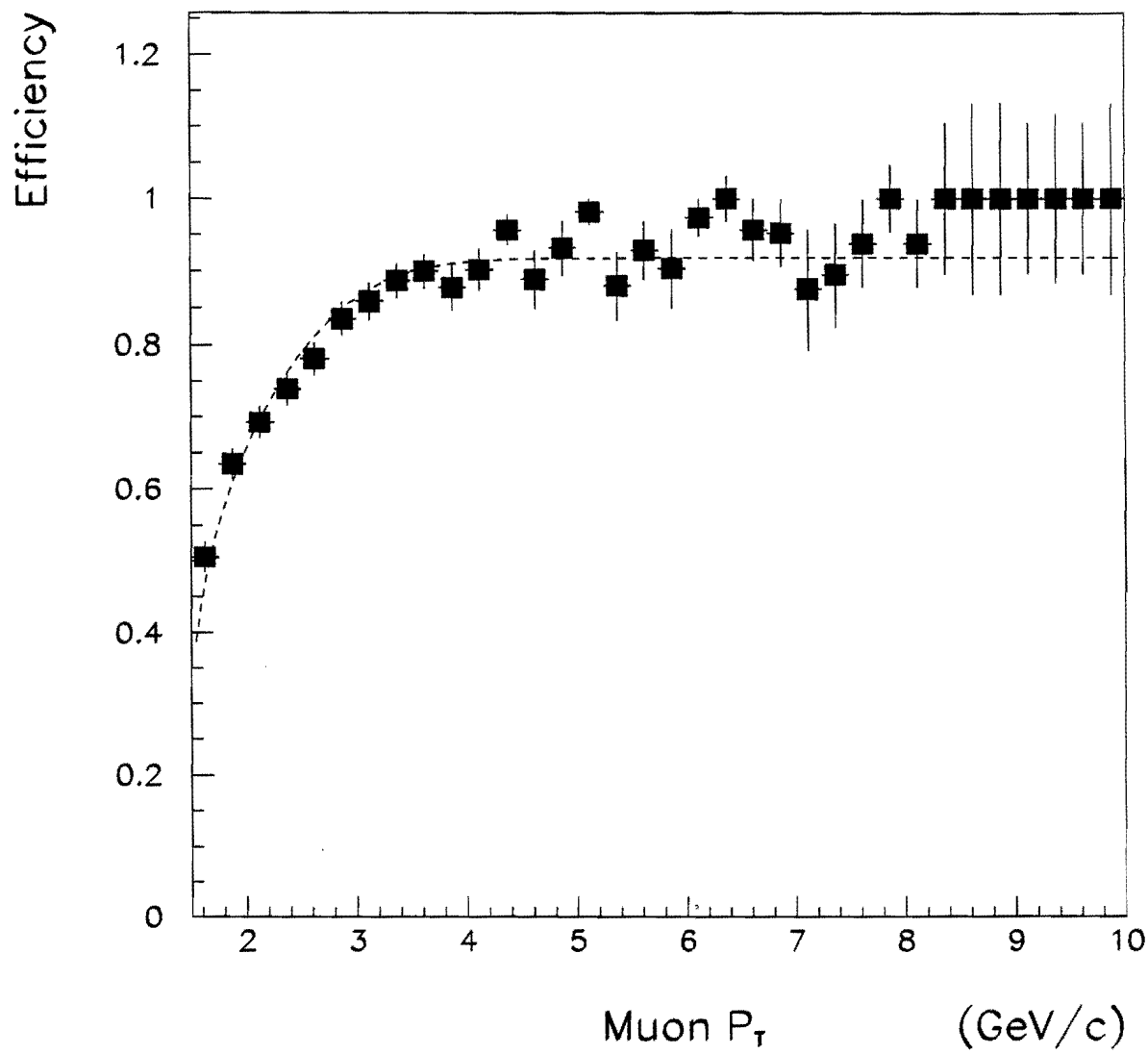

Figure 3.1: Level 1 muon trigger efficiency as a function of P_T.

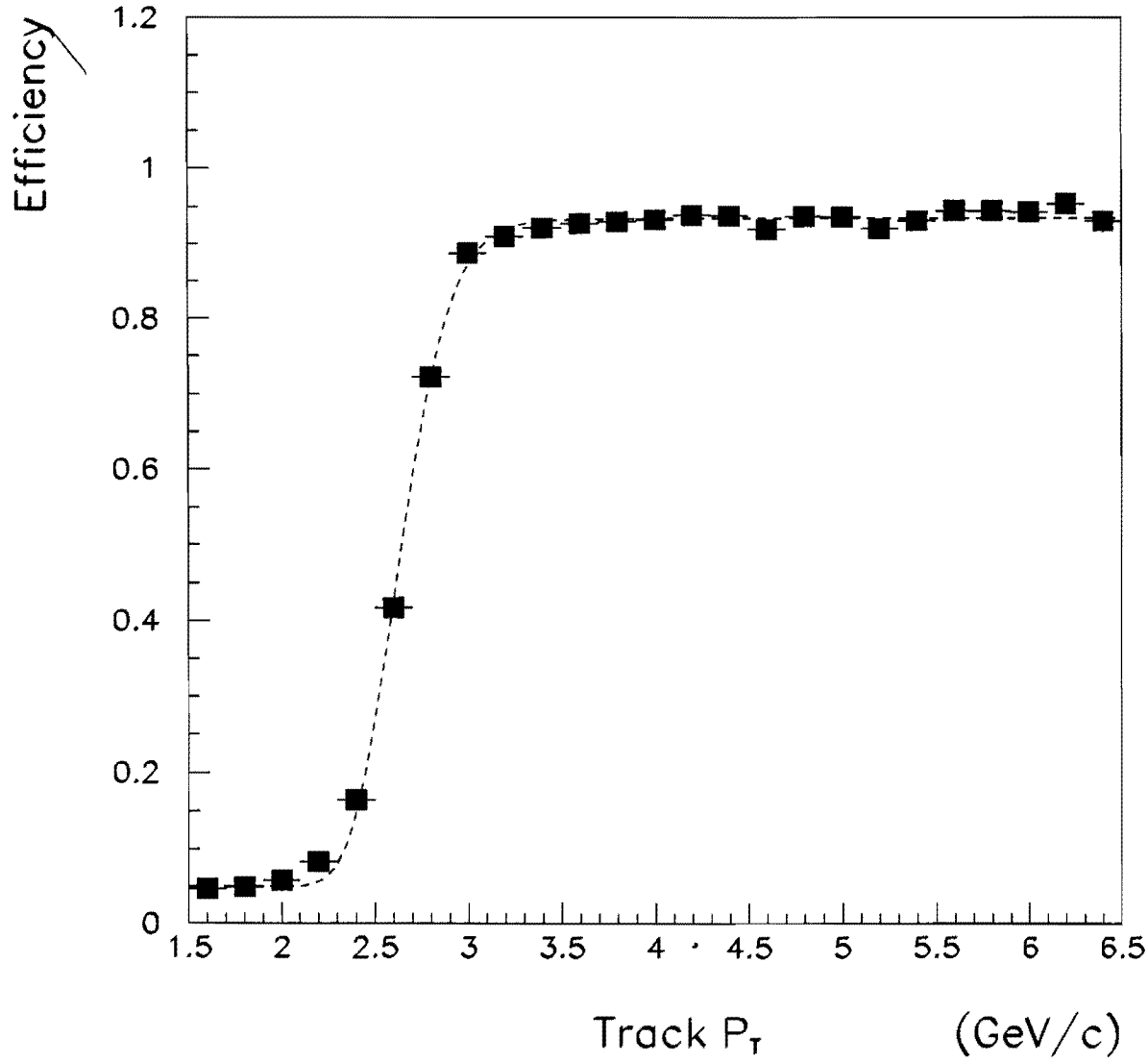

Figure 3.2: Level 2 muon trigger efficiency as a function of P_T.

After an event passes the Level 1 and Level 2 triggers, the data aquisition system [45] initiates the readout of the detector, processes the readout information, and reconstructs the event. The Level 3 dimuon trigger, a software filter, selects events with more sophisticated information on muons. The trigger requires at least two muon segments, each of which is required to match a reconstructed track in the CTC. The CDF online tracking algorithm, which is used for the full 3-dimensional reconstruction of CTC tracks, can measure the P_T of a track with a resolution of $\delta P_T/P_T = 0.002 P_T$. The goodness of the matching between a muon segment and a CTC track is determined by a matching χ^2, described in Chapter 3.3. The Level 3 dimuon trigger requires that the P_T of each muon matched to a CTC track be greater than 2 GeV/c and that the matching χ^2 be less than 16 in both the $r-\phi$ plane and z.

Events passing the three-level CDF trigger are written to a tape. The data written to a tape is relatively low level information such as signal magnitudes in many detector channels. This raw information is converted to physics quantities such as momentum of tracks and energy of jets in the offline event reconstruction. This offline reconstruction uses similar algorithms as the online reconstruction but with more accurate information on the detector calibration and performance. The SVX tracking reconstruction is carried out at this stage. The reconstructed data is separated into a variety of data sets according to its physics content. The parent data set from which we select events for this analysis is the high mass dimuon data, where the invariant mass of a muon pair is required to be greater than 4 GeV/c^2. For the analysis of $b\bar{b}$ events, we improve the $b\bar{b}$ purity of dimuon events with a set of event selection criteria, called cuts, which will be described in Chapter 3.3. In the next section, we briefly review the sources of high mass dimuon events for an understanding of the cuts used in the analysis.

3.2 Sources of Muon Pairs

In high mass dimuon data, there are several different types of events according to their origins. Physics processes such as light meson decays (π, K), $c\bar{c}$ decays, the Drell

Yan process, and Υ decays can produce muon pairs and constitute main backgrounds for $b\bar{b}$ events. Also, there are events which are falsely identified as dimuon events by CDF. Punchthrough and cosmic ray events are typical examples. In this section, the origins of reconstructed muon pairs in the main sources will be discussed.

A. Bottom Decay

The semileptonic decay of bottom hadrons $b \rightarrow \mu\nu_\mu X$, producing direct decay muons, occurs with a branching ratio of 10% [49]. Muons also come from the semileptonic decay of daughter charm hadrons $b \rightarrow c \rightarrow \mu\nu_\mu X$ and are called sequential decay muons. The branching ratio of sequential decay is measured to be about 10%[50]. Although the branching ratios of direct and sequential decays are almost same, muons from direct decays are usually dominant with a minimum P_T cut applied to muons since the P_T distribution of sequential muons is much softer than that of direct muons as shown in Figure 3.3. Events of interests in this analysis are those in which a muon pair comes from the double semileptonic decays of a $b\bar{b}$ pair as follows:

$$b \rightarrow \mu_1, \bar{b} \rightarrow \mu_2$$
$$b \rightarrow c \rightarrow \mu_1, \bar{b} \rightarrow \mu_2 \text{ or } b \rightarrow \mu_1, \bar{b} \rightarrow \bar{c} \rightarrow \mu_2$$
$$b \rightarrow c \rightarrow \mu_1, \bar{b} \rightarrow \bar{c} \rightarrow \mu_2$$

The contribution of the second and the third decay modes are small compared to that of the first one. Dimuons may also come from the cascade decays of a single bottom quark.

$$b \rightarrow \mu_1 c X, c \rightarrow \mu_2$$

They can be easily removed from a data set by requiring that the dimuon invariant mass be greater than the mass of bottom quark.

B. Decay-in-Flight (DIF) and Punchthrough of π and K

Pions and kaons decay to muons with the branching ratio of 99.99% and 63.5% respectively [51, 52]. Since pions and kaons constitute the majority of particles produced in

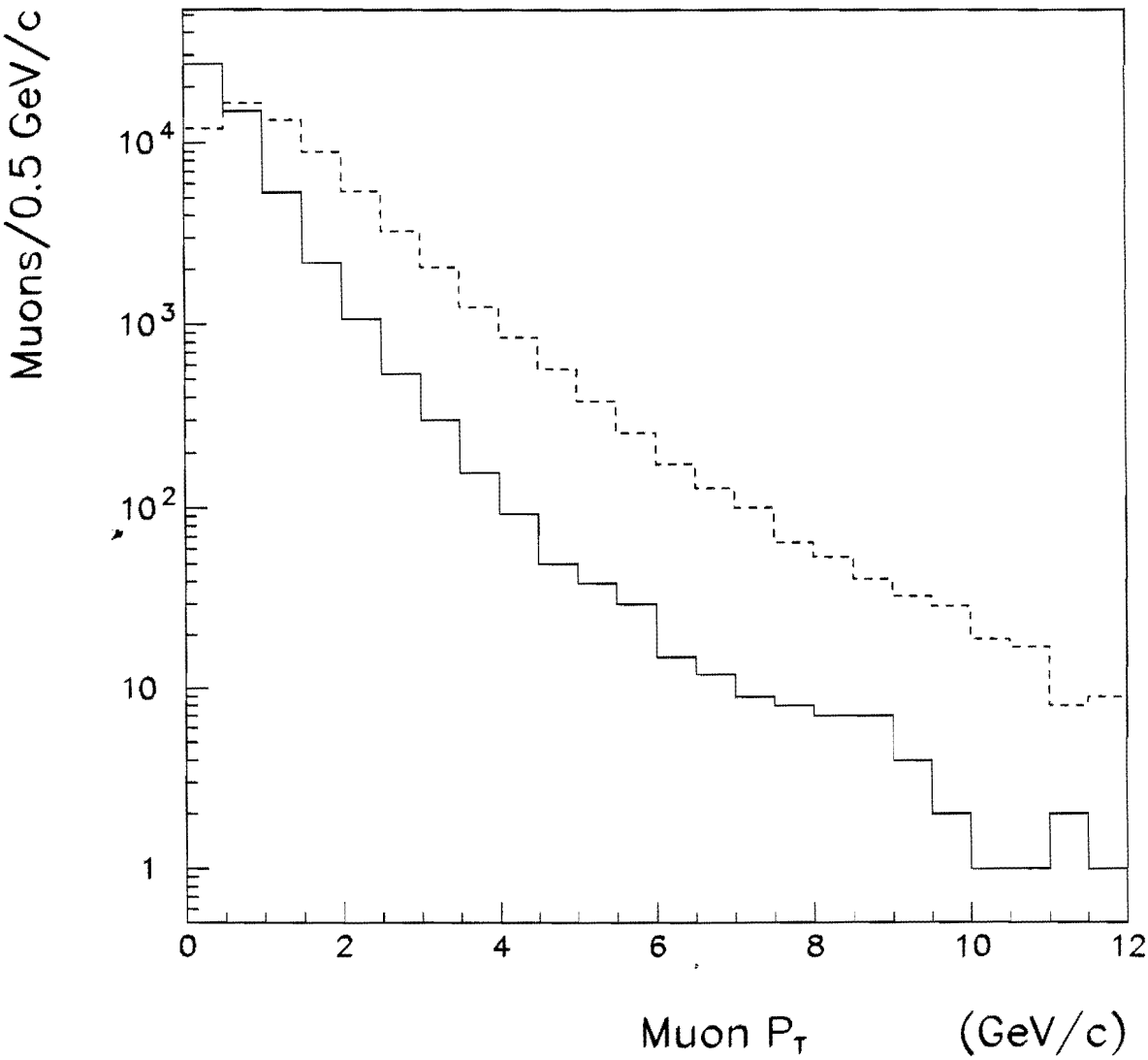

Figure 3.3: Transverse momentum distribution for direct (dashed line) and sequential muons (solid line). The distributions are generated by a Monte Carlo simulation based on NLO QCD and the CLEO decay model.

$p\bar{p}$ collisions, a significant number of these decay muons, called decay-in-flight (DIF), are reconstructed as muons and become one of the main backgrounds in the analysis. Muon signals can be also produced by kaons and pions which pass through the calorimeter and reach the muon chamber or by secondary hadrons produced in interactions within the calorimeter. These are called hadronic punchthrough. They are not real muons but hadrons which fake muon signals. Since there are only 5 interaction lengths of the calorimeter between the interaction point and the central muon detector (CMU), hadronic punchthroughs are expected to exist abundantly in muon data.

C. Combined Process of bottom decay and DIF or punchthrough

In $b\bar{b}$ events, pions and kaons are produced from bottom decays or underlying collision process. A muon from DIF or punchthrough and a muon from bottom decays can also make a muon pair. These dimuon events are not negligible compared to those from other sources and their contribution to the data will be discussed in Chapters 4 and 5.

D. Electroweak Processes

In $p\bar{p}$ collisions, muons are pair-produced when quarks and antiquarks annihilate to produce a virtual photon (the Drell Yan process) [56] or a Z^0 which decays to a muon pair. In Z events, the invariant mass of the two muons can be reconstructed and the mass distribution has a peak at the value of Z mass [53].

E. Υ Decay

Bottomonium states $\Upsilon(1S)$, $\Upsilon(2S)$, and $\Upsilon(3S)$ can produce muon pairs via the decay $\Upsilon \rightarrow \mu^+\mu^-$. Muon pairs from the Υ decays can be easily identified by observing a peak of the dimuon invariant mass at the value of the Υ mass [54].

F. Charm Decay

Dimuons can be produced by the semileptonic decays of $c\bar{c}$ pairs as follows:

$$c \rightarrow \mu^+, \bar{c} \rightarrow \mu^-$$

The semileptonic decay $c \rightarrow \mu\nu_\mu X$ occurs in 9% of all charm decays [55]. The P_T spectrum of muons from charm decays is found to be much softer than that for bottom decays due to softer fragmentation of the charm quark and smaller Q values of charm decay process. In the previous CDF analysis using high mass $e\mu$ data for the 1988-89 run, it has been shown that the fraction of $c\bar{c}$ events relative to $b\bar{b}$ events is 0.07 ± 0.07 [57].

G. Cosmic Ray

A cosmic ray accidently passing through the detector volume is identified and reconstructed by the CDF detector as two separate back-to-back tracks of opposite charges. Reconstructed muon pairs from cosmic rays have a few distinct features which can be used for their identification. First, since cosmic rays are not from $p\bar{p}$ collisions, the distribution of cosmic rays along the beam axis is flat, unlike the Gaussian distribution for muon pairs from $p\bar{p}$ collisions. Secondly, muons are kinematically correlated to each other (e.g., same track parameters) since they are from the same cosmic ray.

3.3 Offline Event Selection

Based on the information on the sources of muons in the dimuon data, we apply a set of offline cuts designed to reject backgrounds and to keep most of the $b\bar{b}$ events.

First, we choose *good* dimuon data for the analysis. We drop events recorded during *bad* runs, in which the CDF detector, especially muon detector systems, did not function properly. The total integrated luminosity representing *good* runs is determined to be $17.4 \pm 0.6\ pb^{-1}$.

As mentioned in Chapter 3.1, a matching χ^2 between a muon segment and a CTC

track is used to identify a muon candidate. The CTC track of the muon candidate is extrapolated to the muon chambers and compared to the muon segment. The difference in the slope (ΔS) and the intercept (ΔI) between the corresponding muon segment and the extrapolated track are combined to form a matching χ^2 as follows:

$$\chi^2=(\Delta I\ \Delta S)\begin{pmatrix} \sigma_I^2 & \delta \\ \delta & \sigma_S^2 \end{pmatrix}^{-1}\begin{pmatrix} \Delta I \\ \Delta S \end{pmatrix}$$

where σ is the P_T-dependent resolution including multiple scattering and energy loss and δ represents the correlation between ΔS and ΔI [58]. The square root of the χ^2 has a Gaussian distribution with $\sigma = 1$, and is independent of P_T. The matching χ^2 can be defined in each muon detector and each coordinate axis. In the CMU detector, we require the matching χ^2 of muons to be less than 9 in the $r - \phi$ plane and less than 12 along the z axis. In the CMP detector, the χ^2 in the $r - \phi$ plane is required to be less than 9.

Hadronic punchthrough, as explained in Chapter 3.2, may be identified as a muon in the CMU detector. To reduce the background events from punchthrough, we use the CMU muons which are also detected by the CMP detector. The additional 3 absorption lengths of material between the CMU and the CMP detector absorbs about 95% of the CMU muons resulting from punchthrough as discussed in Chapter 2.5. On the other hand, the CMP detector is found to be 94% efficient for bottom muons with $P_T \geq 3$ GeV/c. Measurements of the CMP efficiency will be described in detail in Chapter 5.

We use a minimum P_T threshold of 3 GeV/c for muons. This P_T threshold is chosen since the trigger efficiencies, as shown in Figures 3.1 and 3.2, are almost flat above 3 GeV/c, and the systematic uncertainty from the trigger can be minimized. This value is also well above the minimum detectable muon P_T of the CMP detector ($\sim$ 2.2 GeV/c. see Chapter 5).

Since we are going to use the muon impact parameter, we make use of the precision tracking of the SVX detector for muon tracks. To select *good* muon tracks, a set of standard track quality cuts are generally used in CDF analyses. These cuts are designed to reject poorly reconstructed tracks (mainly resulting from the degraded SVX performance due to radiation damage). We require at least 2 *good* hits for a

muon	$p_T \geq 3.0 GeV/c$ CMU $\chi^2_{r-\phi} \leq 9.0$ CMU $\chi^2_z \leq 12.0$ CMP $\chi^2_{r-\phi} \leq 9.0$ CMU-CMP muon segment SVX track track quality cuts on the SVX tracking |impact parameter| $\leq$ 0.06 cm
event	Dimuon Trigger event vertex $\|z\| \leq$ 30.0cm dimuon mass$\geq 5.0 GeV/c^2$

Table 3.1: Dimuon event selection cuts

SVX track and the χ^2 of the SVX tracking per degree of freedom to be less than 6. A *good* hit is defined as a hit which is not shared with another track, which includes no dead channels, and for which the charge is shared over 4 or less channels.

Since the impact parameter distribution for cosmic rays is uniform, most cosmic ray muons can be removed by requiring the absolute value of muon impact parameter to be less than 0.06cm. In Chapter 6, it will be shown that only about 10 % of $b\bar{b}$ dimuons are removed by the impact parameter cut.

If there are more than two muons which pass all the above cuts, we select the two muons with the highest P_T since the P_T spectrum for bottom muons is usually harder than those for muons from other sources. It is found that the relative fraction of events with more than 2 muons to those with two muons is less than 1% and the effect of this muon selection on the analysis is negligible.

In the standard dimuon data, the z vertex of muon tracks is required to be within 30 cm, around the $p\bar{p}$ interaction point, which roughly corresponds to 1σ of the Gaussian distribution of the $p\bar{p}$ interactions [36]. This cut also serves as a preliminary cut for the SVX tracking for muons since the SVX detector covers the region $|z| \leq$ 25cm.

Finally, we require the dimuon invariant mass to be greater than 5 GeV/c^2. This cut is expected to remove dimuon events from the cascade decays of single bottom

quark as explained in Chapter 3.2.

The cuts used to select dimuon events are summarized in Table 3.1. After the data selection, we have 4750 events from the data with an integrated luminosity of $17.4 \pm 0.6 pb^{-1}$.

3.4 Monte Carlo Data

The study of simulated data gives very useful information and guidance for the analysis. In this analysis, impact parameter distributions for bottom muons, charm muons, and decay-in-flights are obtained by a Monte Carlo simulation. The Monte Carlo simulation uses ISAJET 6.43 [59] as an event generator. For the generation, two partons picked from both a proton beam and an anti-proton beam make a hard collision with each other and the cross section for this hard collision is calculated using the lowest order perturbation theory of QCD. The generated heavy quarks are fragmented into hadrons by the Peterson fragmentation function [60] as follows:

$$P(Z) = \frac{constant}{Z(1 - 1/Z - \epsilon/(1 - Z^2))} \tag{3.2}$$

$$Z = \frac{(E + P_L)_{had}}{(E + P_L)_Q} \tag{3.3}$$

where $P(Z)$ represents a probability that a hadron will be fragmented from a heavy quark Q with the fraction, Z, and E and P_L are the energy and longitudinal momentum respectively. The parameter, ϵ, is defined to be $(m^2 + P_T^2)_q/(m^2 + P_T^2)_Q$ where a heavy quark Q and a quark q are combined to a heavy hadron $Q\bar{q}$. We use $\epsilon = 0.006$ [61] in the Monte Carlo simulation. In the case of bottom production, the CLEO Monte Carlo program [62] is used to select decay products of bottom hadrons. As a final step, we perform the detector simulation using the standard CDF package called CDFSIM [63]. The simulated data processed by the same offline reconstruction algorithm used for the dimuon data is selected by the cuts described in Chapter 3.3. Bottom and charm Monte Carlo data are generated by using an average B lifetime of $c\tau = 438\mu$m [64], a D^0 lifetime of $c\tau = 124\mu$m [65], a $D^{\pm}$ lifetime of $c\tau = 317\mu$m [66], and a $D_s^{\pm}$ lifetime of $c\tau = 140\mu$m [67], and a $\Lambda_c^{\pm}$ lifetime of $c\tau = 60\mu$m [68].

Chapter 4

Impact Parameter Fitting Method

In the CDF experiment, dimuon data is one of the most copious sources of $b\bar{b}$ events and constitute a large fraction of triggered events. Reconstructed dimuon events result from decays of heavy quark pairs ($t\bar{t}$, $b\bar{b}$, and $c\bar{c}$), the Drell Yan process, bottomonium decays, decays of π or K, and hadronic punchthrough as explained in Chapter 3.2.

We make use of the precision tracking provided by the CDF silicon vertex detector (SVX) for the identification of muons from B decays. The long lifetime of B hadron, coupled with the SVX tracking, enables the separation of $b\bar{b}$ events from the background events. Specifically, the impact parameter of displaced muon tracks from B decays is used to determine the $b\bar{b}$ content of dimuon events in this analysis. The procedure is to fit the observed impact parameter distributions from the dimuon data with the template distributions of the various known sources. We also present another independent method to measure the $b\bar{b}$ fraction of the data in Chapter 5 for a comparison.

4.1 Impact Parameter

The impact parameter, d, of the track of a decay product is defined as the distance of closest approach to the interaction point (called the primary vertex) in the $r - \phi$ plane as shown in Figure 4.1.

$$d = \beta\gamma ct \sin(\delta) \tag{4.1}$$

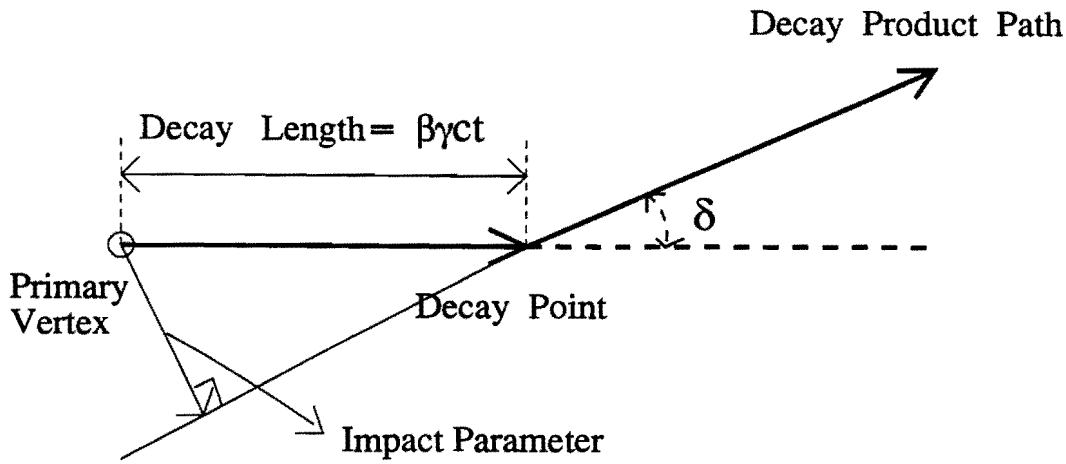

Figure 4.1: Definition of impact parameter.

where ct is the proper decay length of the parent particle from which the track originates, $\beta\gamma$ is the Lorentz boost factor from the relativistic kinematics, and δ is the decay angle of the daughter track with respect to the direction of the parent particle. In the above expression, we note that the impact parameter of a daughter muon is directly proportional to the decay length of the parent particle so that the impact parameter distributions for bottom muons and other background muons are expected to be very different due to the much longer lifetime of bottom hadrons. In principle, the impact parameter distribution of a daughter muon can be formulated [69] as:

$$\frac{dN}{d\Delta} = \frac{1}{2}\int \sin(2\tan^{-1}\frac{y}{z})\frac{2}{1+(\frac{y}{z})^2}\frac{1}{cz\tau}e^{-z}dz \tag{4.2}$$

where Δ is the impact parameter, t is the proper decay time, τ is the lifetime of the parent particle, $z{=}t/\tau$, and $y{=}\Delta/c\tau$. We can obtain the impact parameter distribution of muons from the formula once the lifetime of the parent particle is known. However, the measured impact parameter distribution includes the effects of tracking errors in the detector and an uncertainty in the position of the primary vertex.

The primary vertex is obtained by fitting the beam position using an algorithm based on SVX track information [70]. In the algorithm, the impact parameter of a track coming from the primary vertex is parameterized with the position of the beam

at $z = 0$ (x_0, y_0) and the beam slope (S_x, S_y) in x and y direction as follows:

$$d(\phi_0, Z_0) = (x_0 + S_x Z_0)\sin(\phi_0) - (y_0 + S_x Z_0)\cos(\phi_0) \tag{4.3}$$

where ϕ_0 is the azimuthal angle and Z_0 is the z vertex of the track. The χ^2 of the fit is defined as

$$\chi^2 = \sum_i \frac{(d_i - d(\phi_0^i, Z_0^i))^2}{\sigma_i^2} \tag{4.4}$$

where d_i is the measured impact parameter of the track. Then the beam parameters (x_0, y_0, S_x, and S_y) can be obtained by minimizing the χ^2 of the measured impact parameters of the SVX tracks. Figure 4.2 shows the resolution of primary vertex measurements. In Figure 4.2, we note that the algorithm can measure the x and y position of the primary vertex with a resolution of 22μm.

From the expression for the impact parameter, we expect the impact parameter of bottom decay products to be distributed up to several hundred microns. The precision tracking information from the SVX detector allows the impact parameter of bottom muons to be measured with a resolution of a few tens of microns. The measured impact parameter resolution for SVX tracks is parameterized as a function of P_T as follows:

$$\sigma_d = \sqrt{\sigma_0^2 + (\frac{\sigma_1}{P_T})^2} \tag{4.5}$$

where σ_0 and σ_1 are measured to be 23μm and 34μm respectively [71]. The expression for the impact parameter resolution includes the contributions of the intrinsic resolution of the SVX detector, multiple scattering, and the primary vertex resolution. The intrinsic impact parameter resolution of the SVX detector depends on geometry and the resolution of the silicon microstrips only and is found to be an order of 10μm. The effect of multiple scattering becomes dominant at low P_T and for $P_T \geq 3$ GeV/c, the contribution is negligible.

4.2 Impact Parameter Distribution

Before we discuss the impact parameter fitting method, we briefly review the impact parameter distributions expected for muons from the known sources. As discussed in

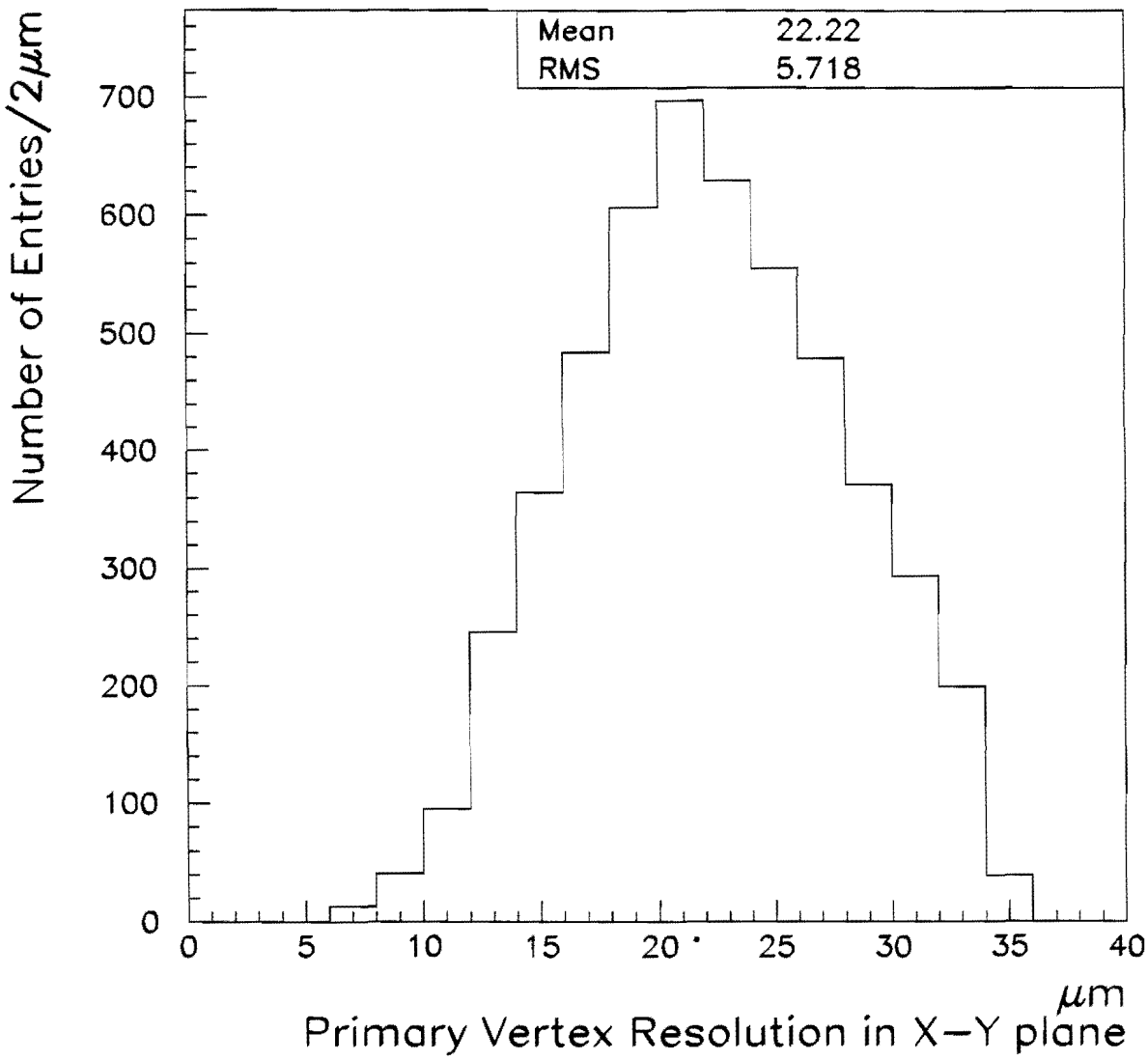

Figure 4.2: The distribution of primary vertex resolution in x-y plane.

Chapter 4.1, the main factors determining the impact parameter distribution of SVX muon tracks are the lifetime of the parent particle and the SVX resolution. Depending on which factor is dominant, impact parameter distributions are obtained either from a Monte Carlo simulation or CDF data. The impact parameter distributions of muons from different sources (see Chapter 3.2) are classified into those for prompt muons, DIF muons, bottom muons, and charm muons according to the lifetime of the parent particle in the following way (Figure 4.8).

• Muons from prompt decays

This category includes muons from Υ decays and the Drell Yan process a s well as hadrons misidentified as muons which are called hadronic punchthroughs. Since these muons are of prompt origin, the generic impact parameter is expected to be zero. However the measured SVX impact parameter includes the effects of the detector such as multiple scattering, tracking resolution, and the primary vertex finding error and thus the distribution is smeared out. In order to obtain the impact parameter distribution for prompt muons, we use CDF data samples instead of a Monte Carlo simulated data since the effect of the SVX resolution is dominant in this case and the actual detector resolution should be included for the distribution for prompt muons.

There are two different control data samples which can be used to obtain the impact parameter distribution of prompt muons. The first sample consists of particle trajectories which go through the region geometrically covered by the central muon upgrade detector (CMP) but do not make a CMP muon segment (to be called NoCMP muons from now on). These are mostly hadronic punchthroughs which showered inside the iron absorber between the central muon detector (CMU) and central muon upgrade detector (CMP). The fraction of bottom or charm muons is estimated to be less than 1% in this sample since these muons make hits in the CMP detector with a high efficiency ($\sim$ 94%), as will be shown in Chapter 5. Since decay-in-flight (DIF) muons are not 100% CMP efficient (see Chapter 5), there may be some DIF muons in the NoCMP data. The effect of DIF muons on the impact parameter distribution of NoCMP muons is negligible as will be shown below.

The second sample is jet data where the P_T of a jet is required to be greater than 20 GeV/c. This sample is chosen because tracks in the jet data are mostly of prompt origin and the content of heavy flavour is small [72]. The fraction of bottom tracks and charm tracks are found to be $1.35 \pm 0.01\%$ and $3.36 \pm 0.80\%$ respectively [72]. Figure 4.3 shows the impact parameter distribution of tracks with $P_T \geq 3$GeV/c from the jet sample and compared to the distribution of muons in NoCMP data. The distributions seem to be very similar to each other within statistical fluctuations. Since the jet data provide us with greater statistics, we use the jet sample to obtain the impact parameter distribution of prompt muons.

- Decay-in-Flight muons (DIF)

Some of the background muons in dimuon events are decay-in-flight muons from pions or kaons as discussed in Chapter 3.2. From Equation (4.1), DIF muons are expected to have a very broad impact parameter distribution due to the long lifetime of a pion or a kaon ($c\tau_\pi = 7.8$m and $c\tau_K = 3.7$m). However, the CDF offline reconstruction significantly changes the impact parameter distribution for DIF muons.

If these mesons decay inside the CTC, some of the trajectories will have large kinks at the point of the decay which, in most cases, is far from the primary vertex. The CDF offline tracking algorithm reconstructs smooth helical trajectories from sets of CTC hits and rejects trajectories with a measurable kink. After the CDF offline reconstruction, most DIF muons are removed and remaining muons show an impact parameter distribution similar to that for prompt muons (or tracks in the jet data).

Figure 4.4 shows the SVX impact parameter distributions which are simulated by a Monte Carlo method for pion and kaon DIF muons and for tracks in the jet data. In the Monte Carlo simulation, the same CDF offline reconstruction package is used to generate the impact parameter distribution for DIF muons. The K to π ratio is set to be 1/3 in the simulation based on the experimental results [73]. The impact parameter distribution for DIF muons is slightly broader than that for jet tracks. Since they are very similar to each other, we can model the impact parameter distribution of DIF muons using tracks in the jet data. As far as the SVX impact parameter is concerned, DIF muons can be regarded as prompt muons.

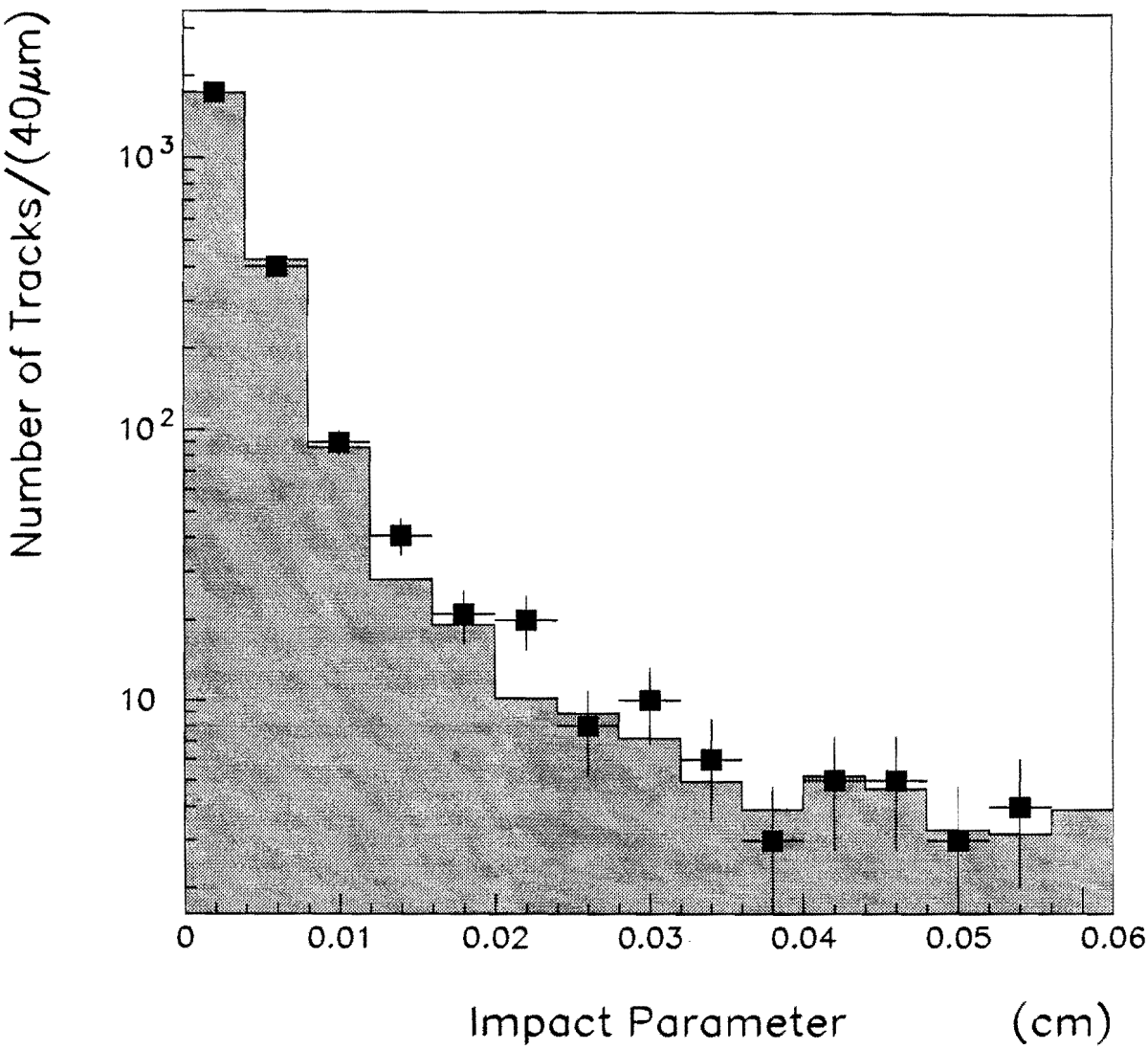

Figure 4.3: The SVX impact parameter distribution of jet tracks (solid line) and NoCMP muons (box) with $P_T \geq$3GeV/c.

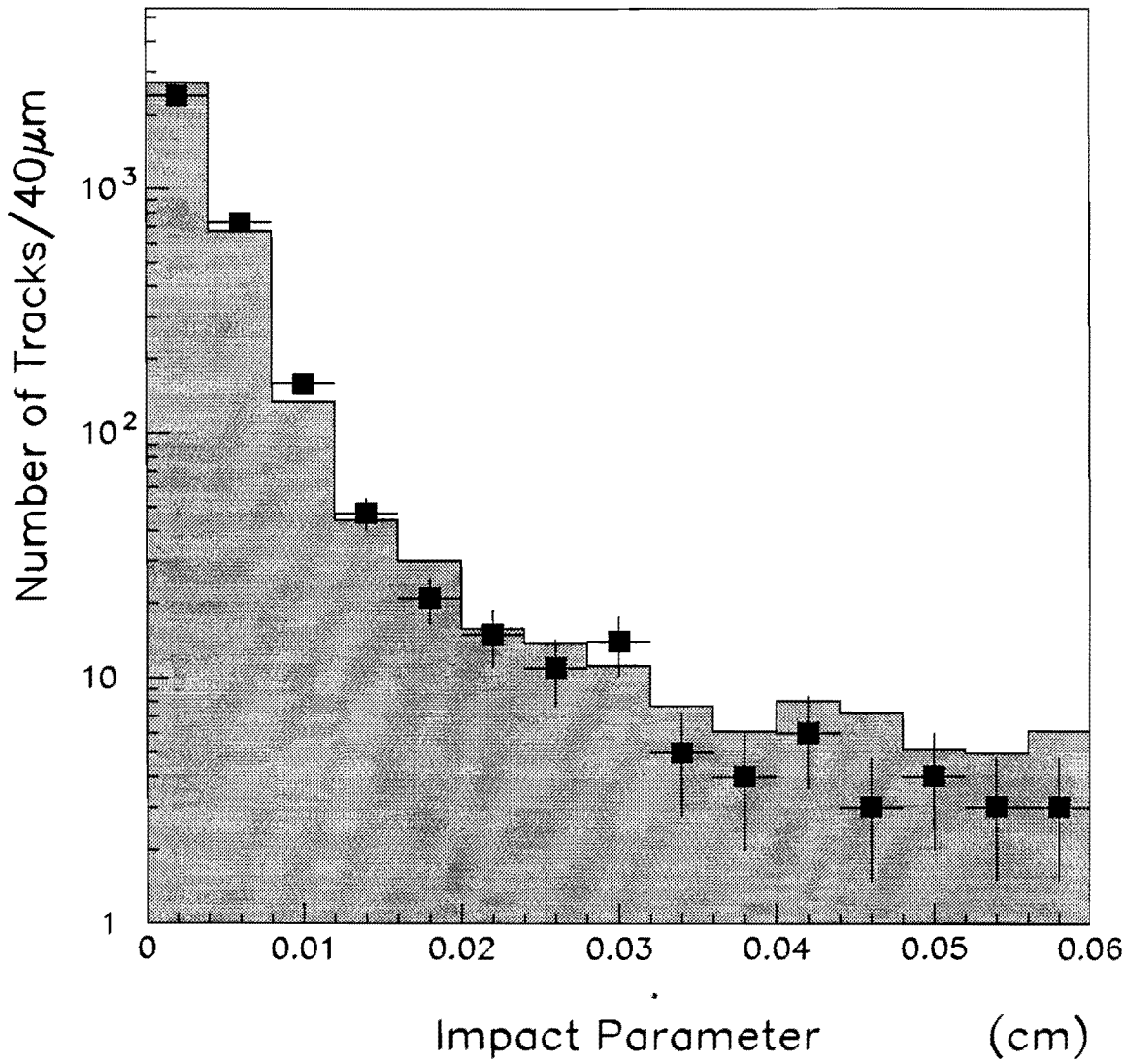

Figure 4.4: The SVX impact parameter distribution of jet tracks (solid) and DIF muons (box) with $P_T \geq$3GeV/c. The Monte Carlo (ISAJET+CDFSIM) simulation is used to generate these distributions. The ratio of K to π is 1/3 in this plot.

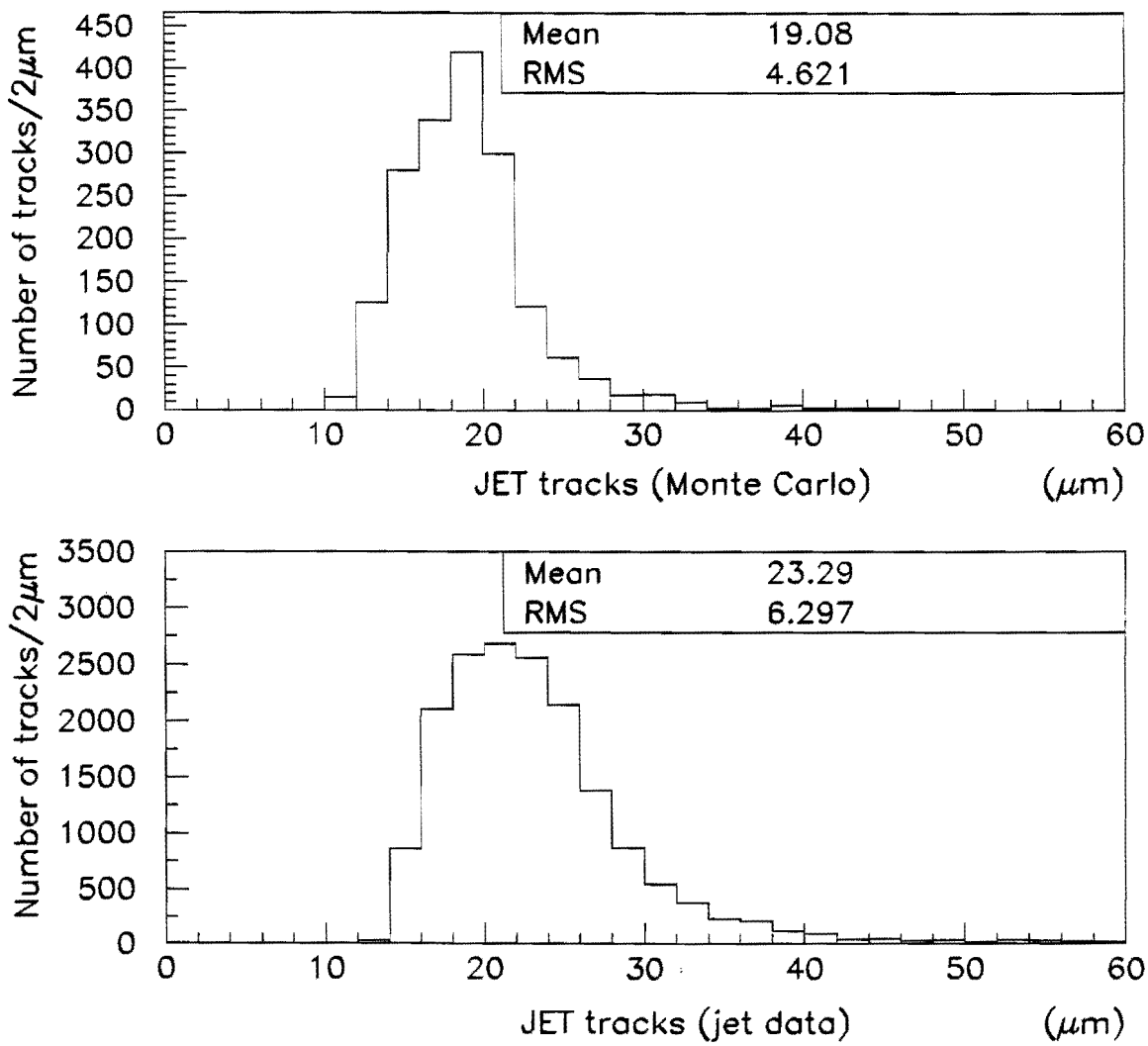

Figure 4.5: The distribution of the SVX impact parameter resolution from jet data and Monte Carlo jet data with $P_T \geq$3GeV/c.

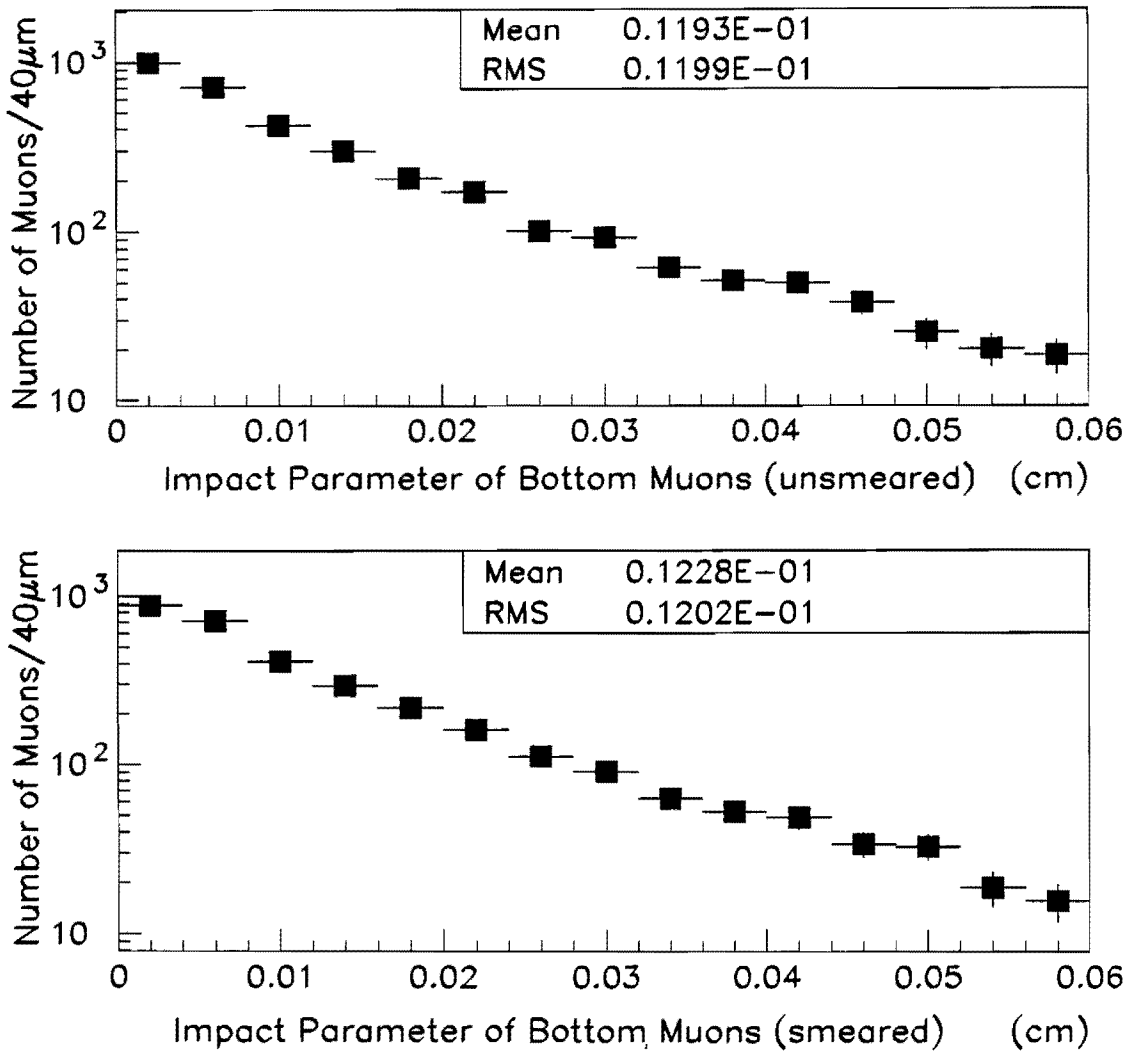

Figure 4.6: The SVX impact parameter distribution of bottom muons with $P_T \geq 3$ GeV/c. The unsmeared distribution is from the Monte Carlo simulation (ISAJET+CDFSIM). The smeared distribution is obtained by fluctuating the impact parameter with a Gaussian distribution with a width of 13μm.

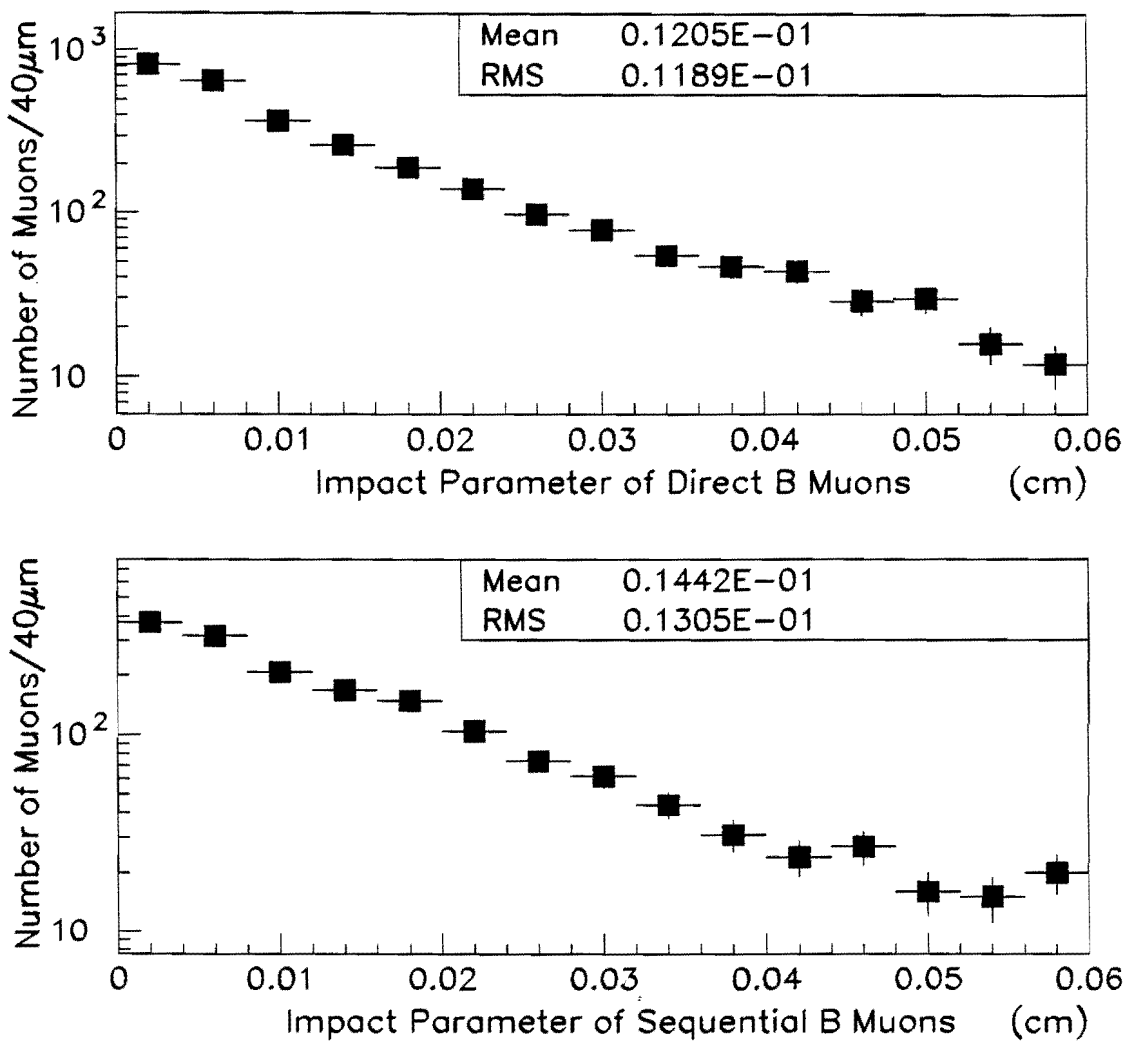

Figure 4.7: The SVX impact parameter distribution for direct B muons and sequential B muons with $P_T \geq$3GeV/c. A Monte Carlo simulation is used to generate these distributions.

• Bottom and Charm Muons

Monte Carlo methods are used to establish the impact parameter distributions for muons from bottom and charm decays. The Monte Carlo simulation used is discussed in detail in Chapter 3.4. Since lifetimes of bottom and charm hadrons are much greater than the impact parameter resolution of the SVX detector ($\sim 20\mu$m), the dominant factor affecting the impact parameter distributions of charm and bottom muons is the kinematics of the semileptonic decays, which the Monte Carlo simulation is expected to describe well.

Monte Carlo simulations, in general, underestimate the detector resolution since they may not fully take into account the actual performance of the detector. Figure 4.5 shows the impact parameter resolution distribution for jet tracks from the jet data and the Monte Carlo simulation. The difference of the average values is about 13μm, which is small compared to the B lifetime. To account for the resolution difference, we smear the Monte Carlo simulated impact parameter distributions for bottom and charm muons by a Gaussian distribution with a width equal to the resolution difference. Original and smeared distributions for bottom muons are shown in Figure 4.6. The effect of the smearing procedure will be included as a systematic in Chapter 4.4.

The impact parameter distribution for muons from sequential decays ($b \rightarrow c \rightarrow \mu$) is expected to be broader than that for muons from direct decays ($b \rightarrow \mu$) due to an additional decay chain with a finite life time. The impact parameter distributions for direct and sequential muons are shown in Figure 4.7. Since they are highly correlated, we can not use the impact parameter distributions separately in the fit in order to obtain the fraction of direct or sequential muons. The relative fraction of sequential muons to direct muons is determined by the Monte Carlo simulation and found to be 0.123 ± 0.015 for $P_T \geq 3$GeV/c. The sequential fraction will be discussed in detail in Chapter 8.

• Cosmic rays

In the CDF offline reconstruction, a cosmic ray track may appear as a pair of

muons of opposite sign. The impact parameters of these muons must be same. We clearly see such an effect in Figure 4.12, a plot of a two dimensional SVX impact parameter distribution of the data. Along the diagonal axis in the two dimensional impact parameter space, the uniform distribution from cosmic ray muons is observed. In this analysis, we require the SVX impact parameter of muons to be less than 0.06cm, thus removing most of the cosmic ray events. The number of residual cosmic ray events can be estimated by extrapolating the uniform distribution along the diagonal axis into the region where the analysis is carried out. We estimate the number of residual cosmic ray events to be 5.1 ± 1.3 and this contribution is negligible (0.1% of the data).

Finally, we discuss the P_T dependence of the impact parameter distributions. The expression for the impact parameter distribution (4.2) indicates that in principle, the impact parameter distribution does not depend on the P_T of daughter products but on the proper lifetime. Also, the impact parameter resolution is very weakly dependent upon P_T for $P_T \geq 3$ GeV/c as shown in the expression. Figures 4.9, 4.10, and 4.11 show the impact parameter distributions for bottom muons, charm muons, and jet tracks respectively over different P_T ranges. The distributions are found to be very insensitive to P_T.

The impact parameter distribution from the dimuon data (Figure 4.8) clearly shows that there are two main components in the distribution: one with a long lifetime and one of prompt origin. The impact parameter distributions of muons from the different sources are distinctively different as shown in Figure 4.8, which allows the parent fractions to be determined by the impact parameter fitting method.

4.3 Two Dimensional Impact Parameter Fitting Method

Since there are two muons in an event, an impact parameter fit is performed in the two dimensional space of impact parameters. Each axis represents the impact parameter of one of the two muons. The two dimensional impact parameter fitting

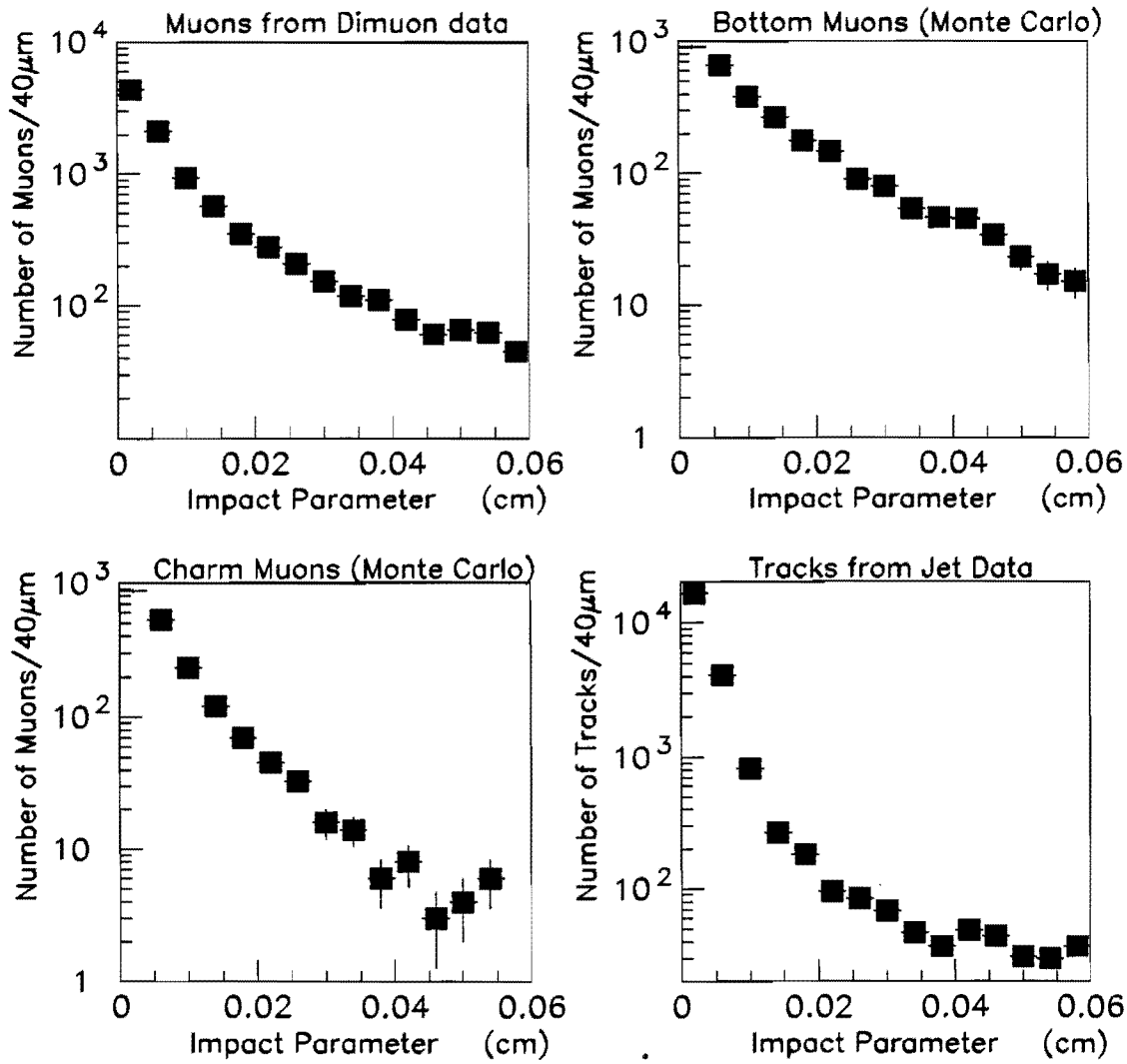

Figure 4.8: Impact parameter distributions of muons of various sources with $P_T \geq$ 3GeV/c. The distributions for bottom muons and of charm muons are generated from the Monte Carlo simulation with the average $c\tau^B = 438\mu$m and $c\tau^D = 183\mu$m.

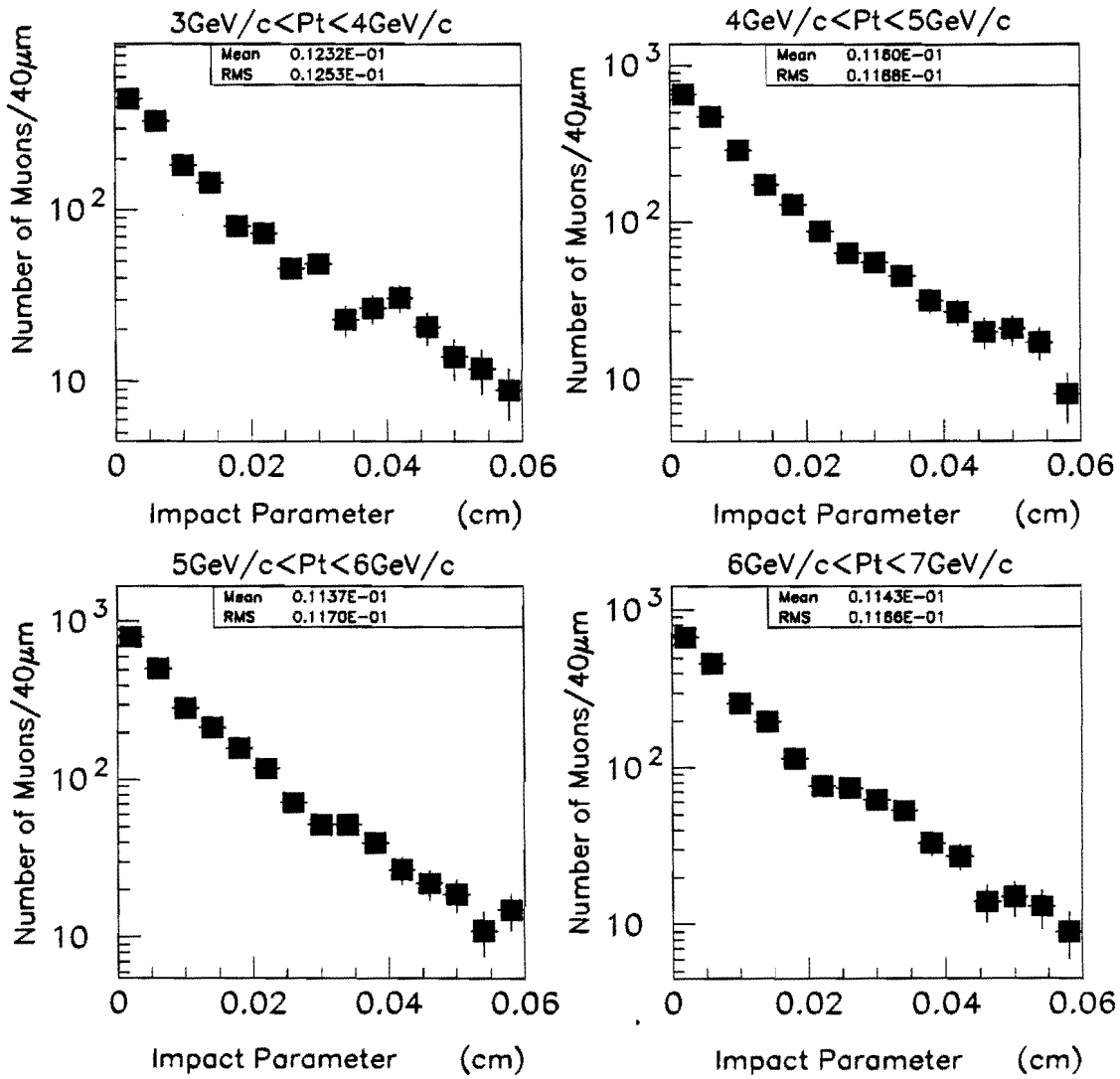

Figure 4.9: Impact parameter distributions of bottom muons for each P_T bin. These distributions are from the Monte Carlo simulation (ISAJET+CDFSIM) with the average $c\tau = 438\mu$m.

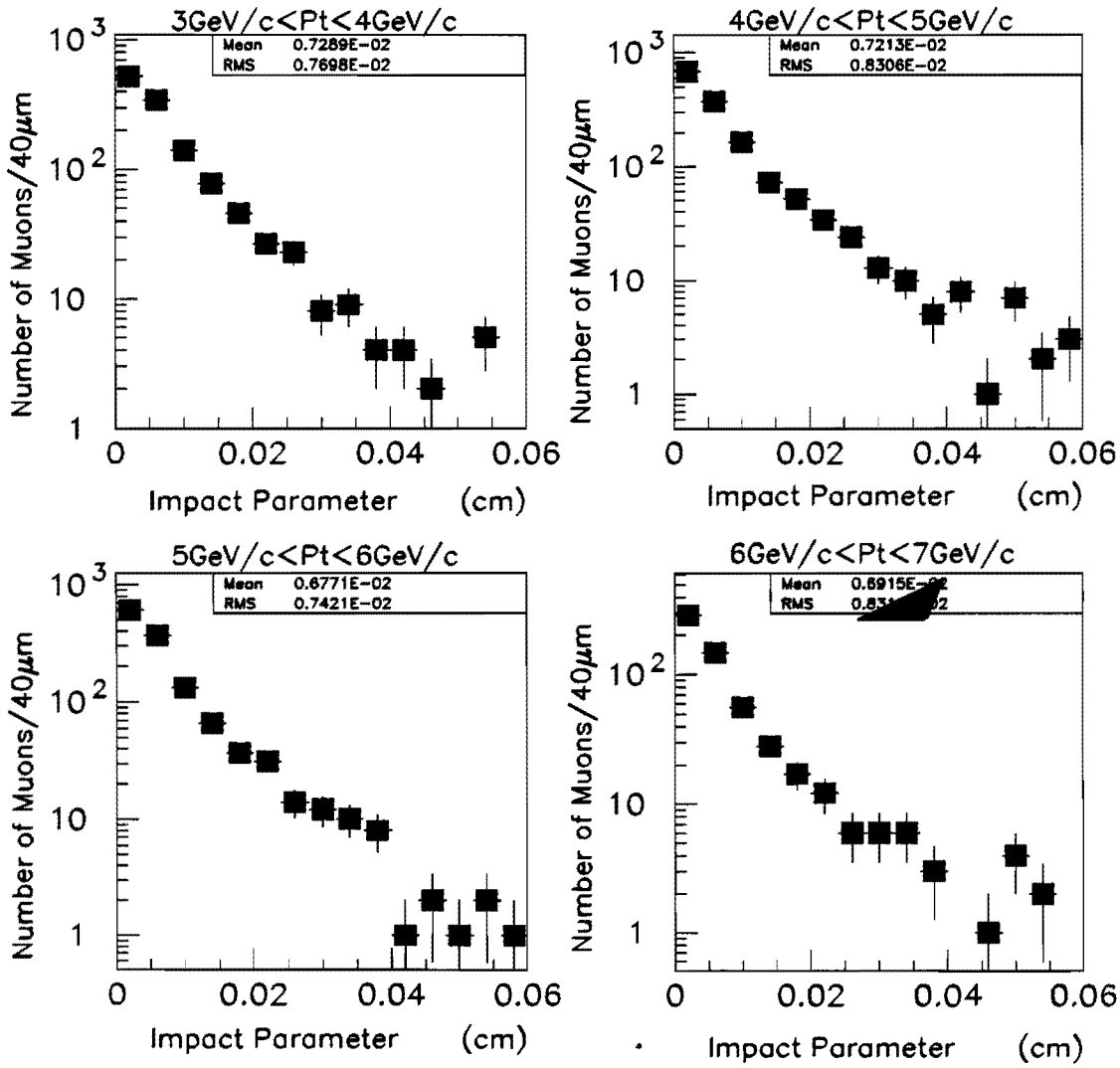

Figure 4.10: Impact parameter distributions of charm muons for each P_T bin. These distributions are from the Monte Carlo simulation (ISAJET+CDFSIM) with the average $c\tau = 183\mu$m.

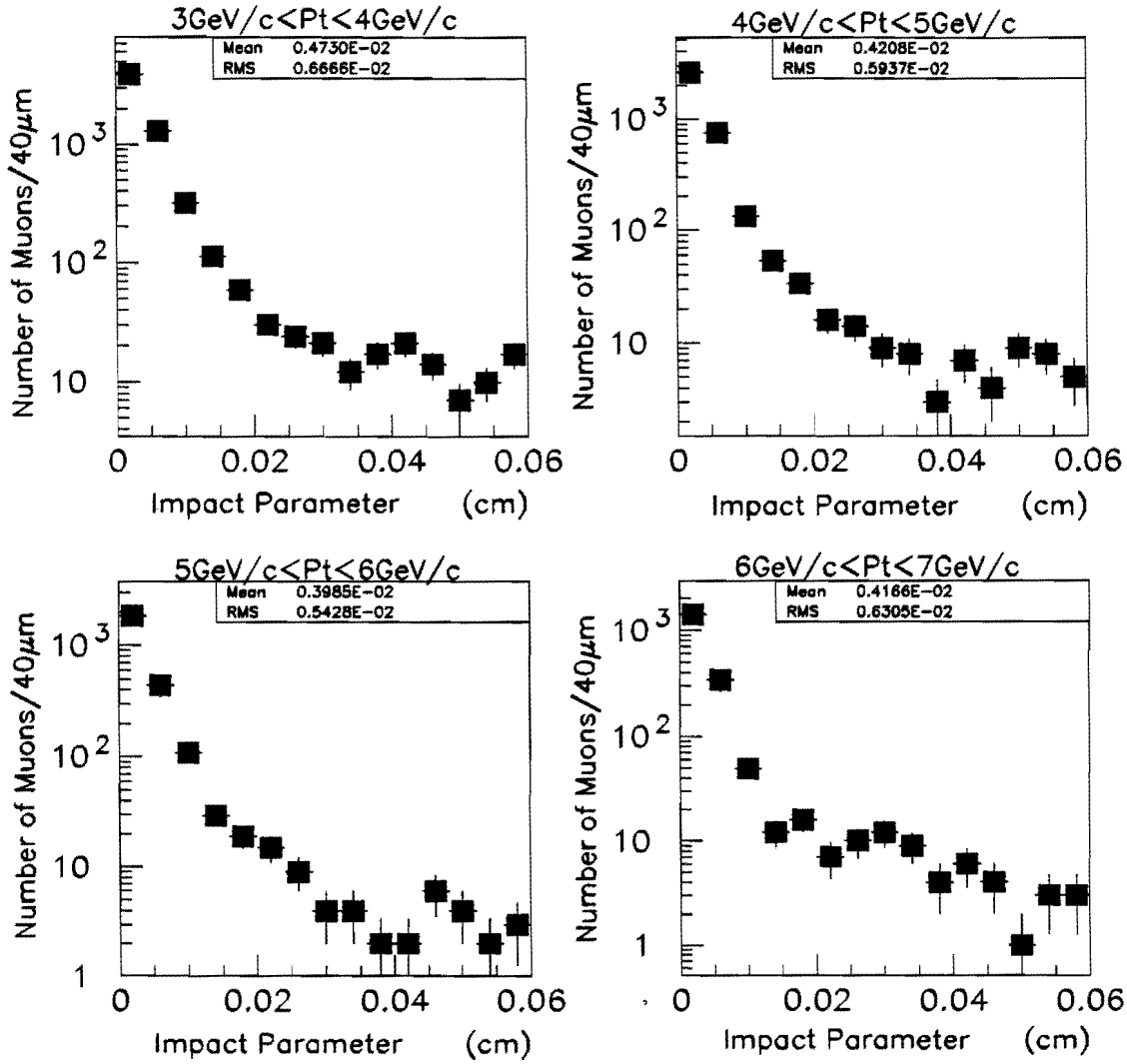

Figure 4.11: Impact parameter distributions of jet tracks for each P_T bin. These distributions are from jet data.

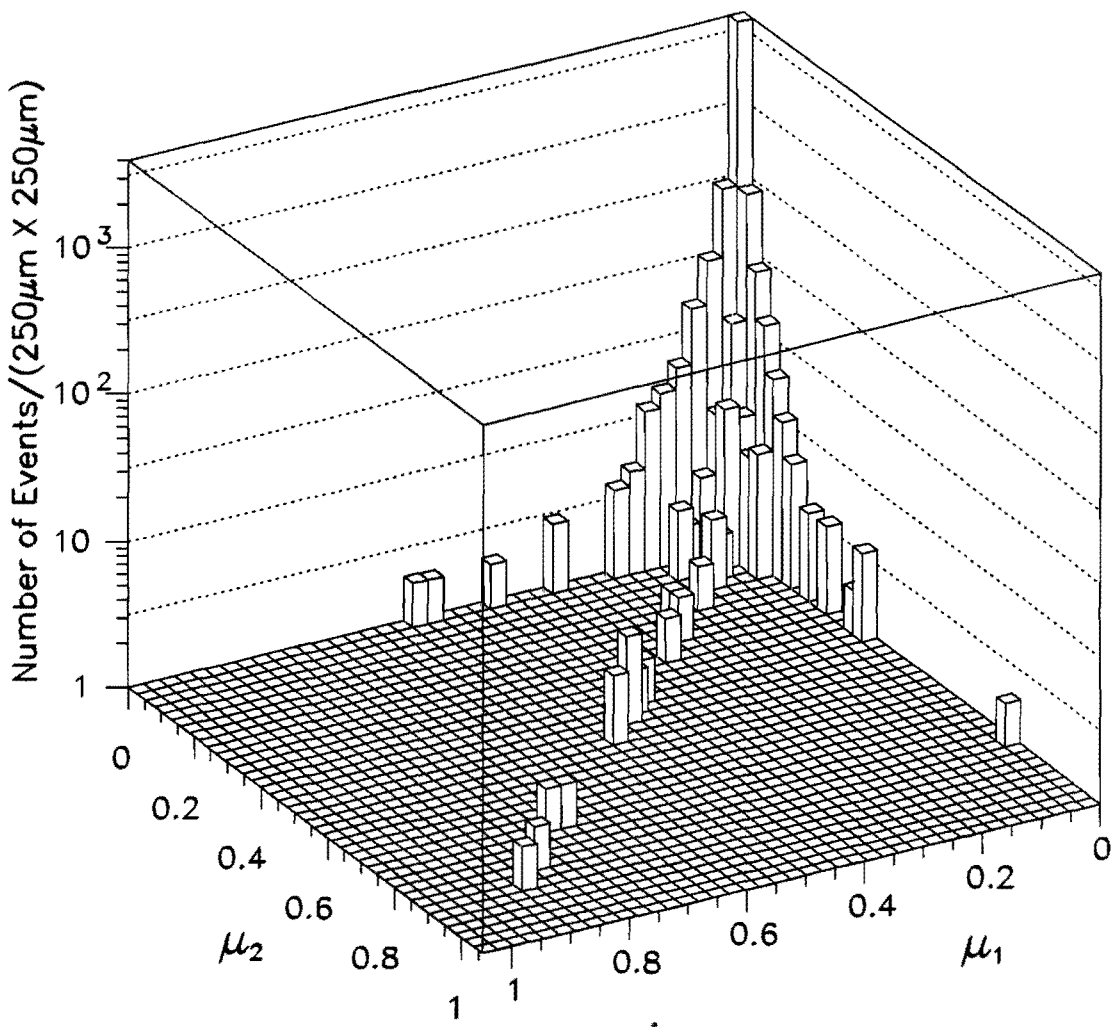

Figure 4.12: A two dimensional impact parameter distribution from dimuon data with $|d| \leq 1$cm. Along the diagonal axis, dimuon events from cosmic rays are observed.

method exploits the fact that the impact parameter for each muon is an independent uncorrelated variable. The 2-dimensional template distributions for each type of dimuon event are made by convoluting the relevant one dimensional distributions.

A binned maximum log likelihood method is used in the fit. The fitted values of variables are found by maximizing a likelihood function with the fitting program MINUIT [74]. The likelihood L can be defined as follows:

$$L = \Pi_i \Pi_j (l_{ij}^{n(i,j)} e^{-l_{ij}} / n(i,j)!)$$

$$l_{ij} = f_{bb} H_{bb}(i,j) + f_{pp} H_{pp}(i,j) + f_{cc} H_{cc}(i,j) + f_{bp} H_{bp}(i,j)$$

where i, j are bin indices and $n(i,j)$ is the number of events in the (i,j)th bin. H_{bb}, H_{cc} and H_{pp} represent normalized two dimensional impact parameter distributions for $b\bar{b}$, $c\bar{c}$, and prompt dimuon events and the f's are the corresponding fractions of each component. The template distribution, H_{bd}, represents events with one prompt muon from a π or a K and one bottom muon. The two dimensional template histograms for each component in the likelihood are shown in Figure 4.13.

The two dimensional distributions of H_{bp} and H_{cc} are very similar to each other as plotted in Figure 4.14 so that the fractions of the two components can not be extracted separately from a simultaneous fit. If we include all the components in the fit, the fitting becomes unstable. In order to overcome this problem, we fix the relative fractions of the $c\bar{c}$ events and the events with a bottom muon and a prompt muon and make a new template histogram, H_{sum}, which is a linear combination of H_{bp} and H_{sum}. In this case, the likelihood function l_{ij} can be rewritten as follows:

$$l_{ij} = f_{bb} H_{bb}(i,j) + f_{sum} H_{sum}(i,j) + f_{pp} H_{pp}(i,j)$$

$$H_{sum}(i,j) = A_1 H_{bp}(i,j) + A_2 H_{cc}(i,j)$$

where A_1 and A_2 are the normalized fractions of each component. For convenience, we assume that the two components contribute equally ($A_1 = A_2 = 1/2$) in H_{sum}. The variations of f_{bb} due to different values of A_1 and A_2 will be included in the systematic uncertainty, as described in the next section.

We perform the fit to the data requiring $P_T \geq 3$ GeV/c for both muons and

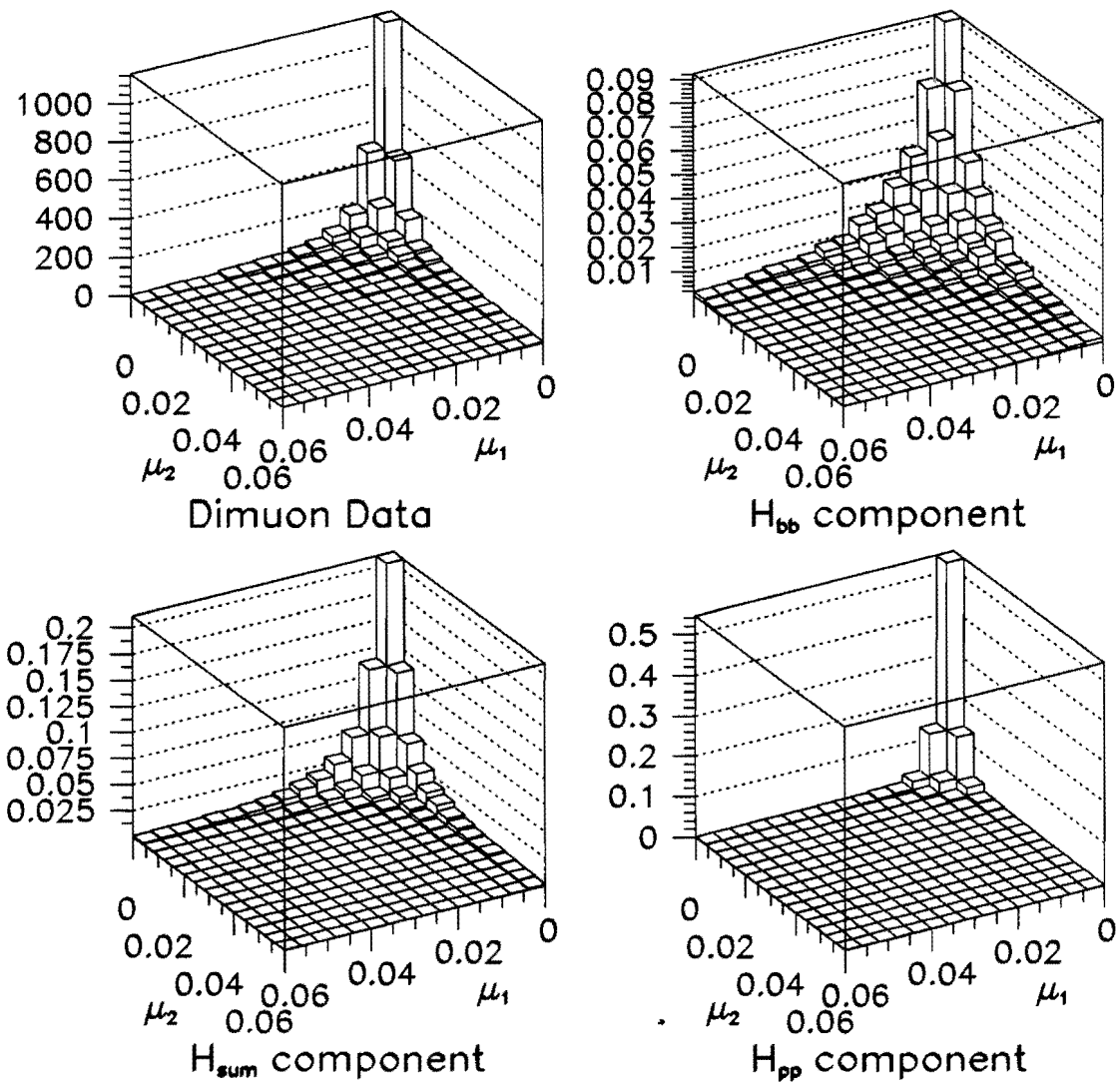

Figure 4.13: Two dimensional impact parameter distributions from data and each component. The template histograms for each component are normalized so that total sum of entries is 1.

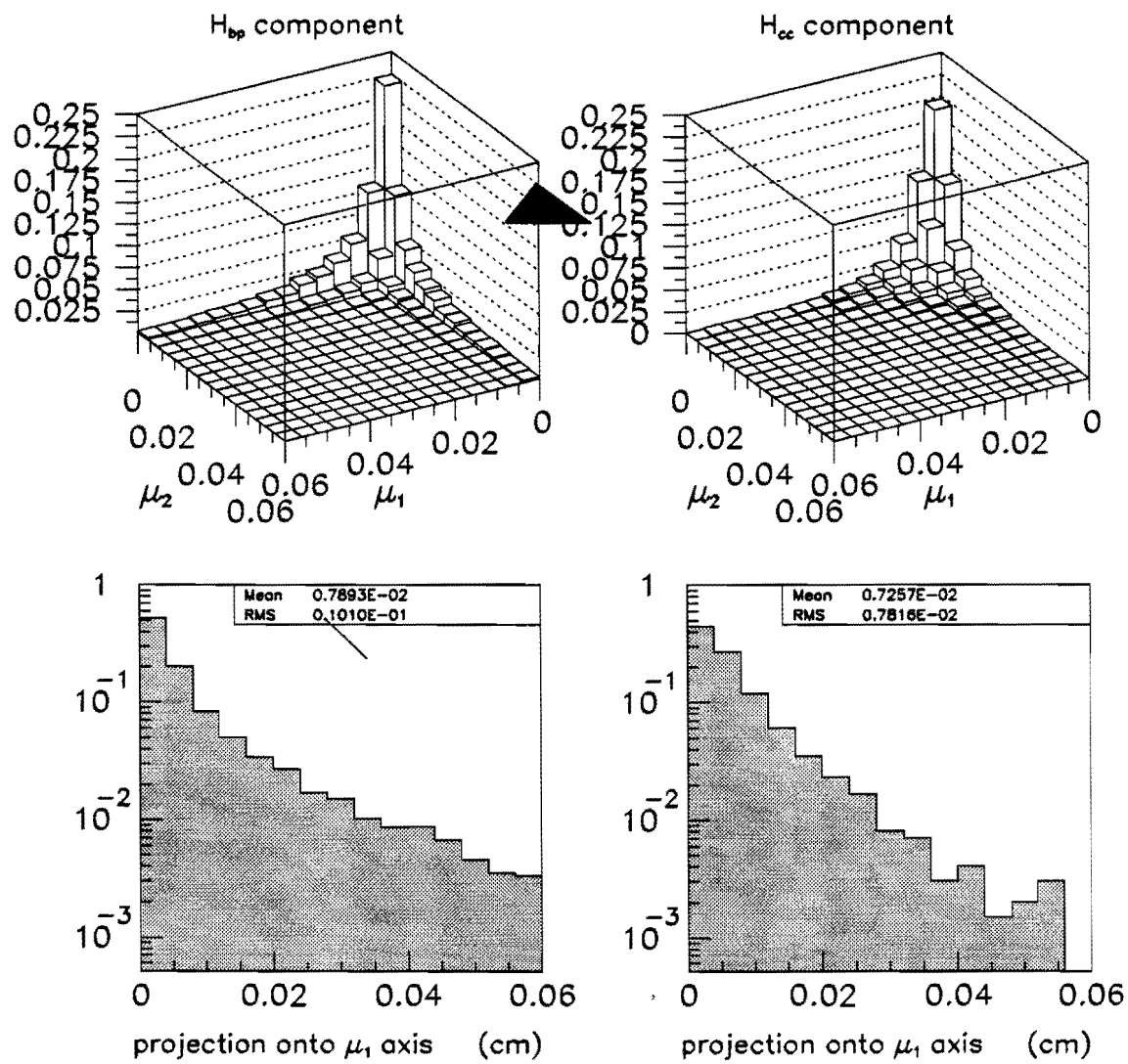

Figure 4.14: The upper two plots are two dimensional distributions for each component. The lower plots are projections of these histograms onto μ_1 axis.

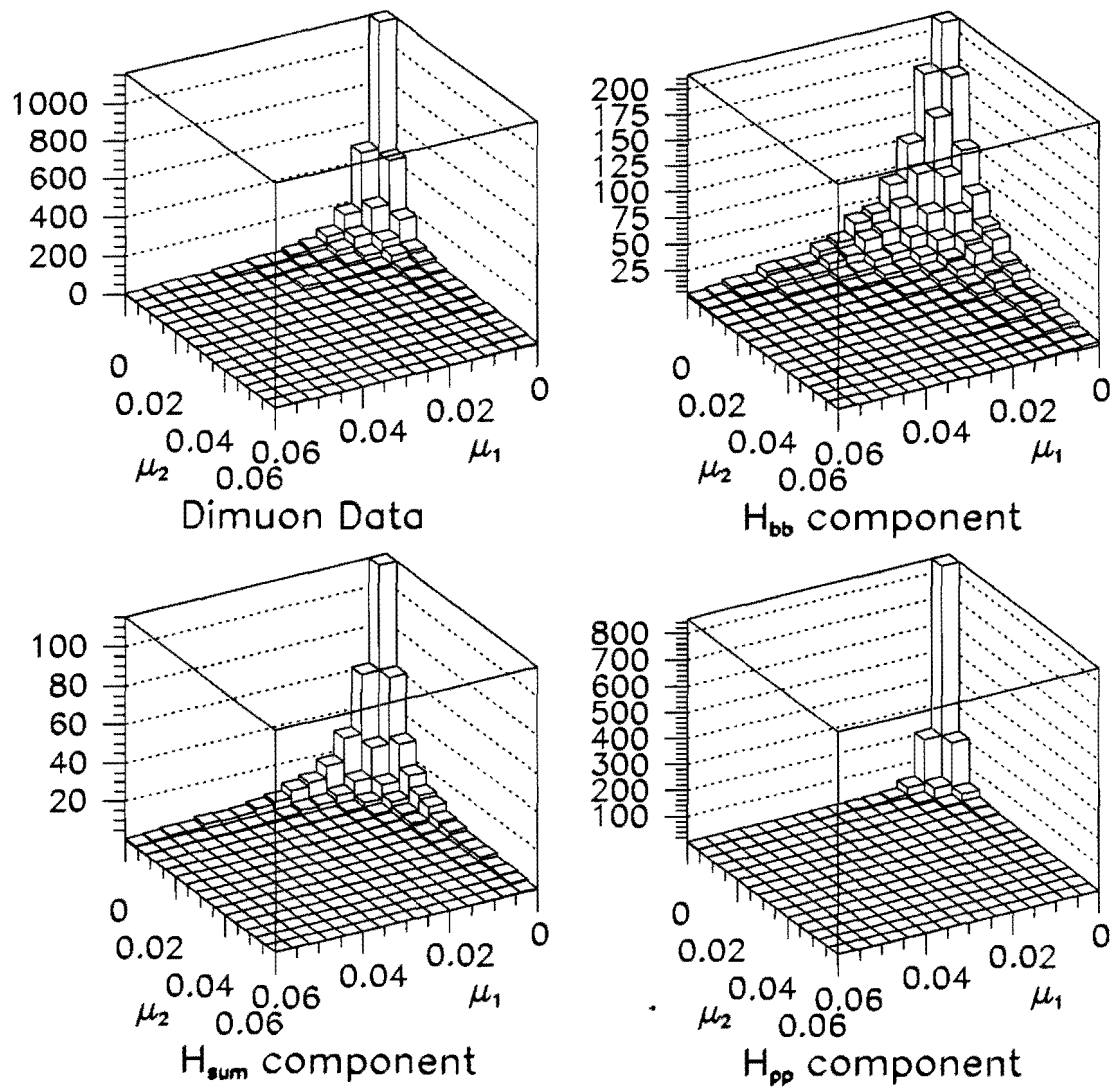

Figure 4.15: The distribution from data and the contributions of each component from the fit.

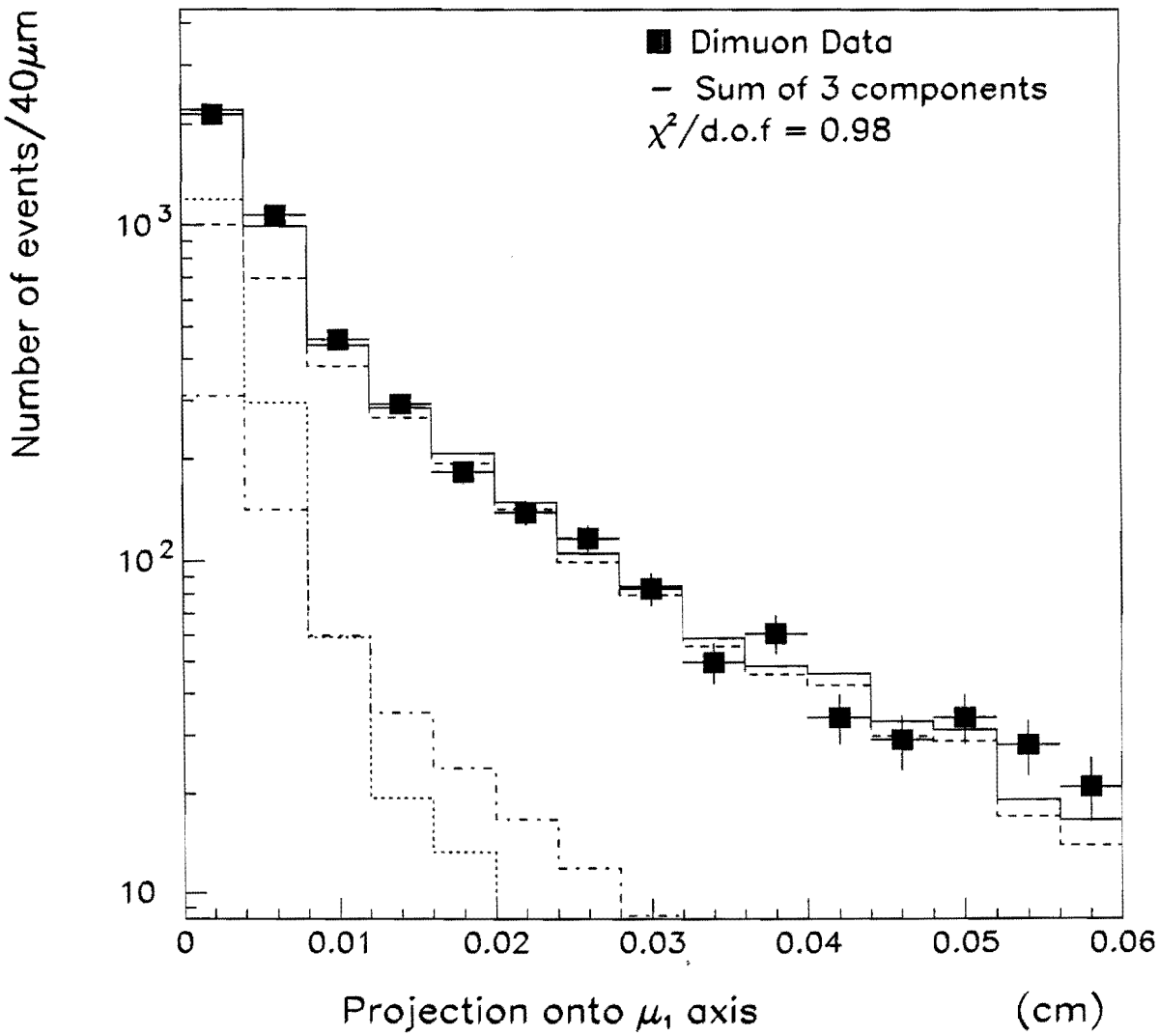

Figure 4.16: Comparison between the projection of the data distribution (filled box) and that of sum of 3 components (solid line). Each component is denoted by dashed line (H_{bb}), dotted line (H_{pp}), and dash-dotted line (H_{sum}) respectively.

obtain 2471 ± 104 $b\bar{b}$ events ($f_{bb} = 0.520 \pm 0.022$), 1628 ± 188 prompt dimuon events ($f_{pp} = 0.343 \pm 0.040$) and 652 ± 157 H_{sum} events ($f_{sum} = 0.137 \pm 0.033$) for a total of 4751 events, where the errors represent the 1σ uncertainty of the fit. Figure 4.15 shows the distribution from data and the contributions of each component obtained from the two dimensional fitting. For a comparison of the data and the fit result, projections of the two dimensional impact parameter distributions onto one axis are plotted in Figure 4.16. The fit χ^2 between the distribution from data and the summed distribution of template histograms from the fit is found to be 0.98. In Figure 4.16 we note that in the region with $|d| \geq 0.03$cm, the contribution of the $b\bar{b}$ component is dominant and it is this region which determines the $b\bar{b}$ fraction.

The fit can be performed for like-sign (LS) and opposite-sign (OS) dimuon events separately. In LS events, there is no contribution from $c\bar{c}$ decays since $c\bar{c}$ decays produce muons pairs of opposite sign if we neglect $D\bar{D}$ mixing. Therefore the log likelihood function l_{ij} is rewritten as

$$l_{ij} = f_{bb}H_{bb}(i,j) + f_{pp}H_{pp}(i,j) + f_{bp}H_{bp}(i,j)$$

where only three components ($b\bar{b}$ events, prompt dimuon events, and events with a bottom muon and a prompt muon) are included in the likelihood. From the fit with the different likelihood functions, we obtain 838 ± 53 LS events and 1669 ± 88 OS events where the errors come from the fit. These results will be used for the $B^0\bar{B}^0$ mixing analysis in Chapter 8.

4.4 Systematic Uncertainty in the Impact Parameter Fit

In this section, we discuss the systematic uncertainty in the two dimensional impact parameter fitting method. The systematic uncertainty mainly results from the uncertainties in the shapes of the impact parameter distributions for bottom and prompt muons and the contribution of the physics backgrounds such as charm muons. The impact parameter distribution for bottom muons is subject to change according to input parameters to the Monte Carlo simulations such as the lifetime of B hadrons,

the impact parameter resolution, and the fraction of sequential muons.

• Lifetime of B hadron

The Monte Carlo data for bottom muons is simulated using the average B lifetime of 1.46 psec ($c\tau = 438\mu$m). We take into account the effect of the uncertainty of the measured lifetime on the impact parameter distribution. From the CDF analysis [64], we assign the $\pm 6\%$ ($\pm 25\mu$m) uncertainty to the average B lifetime. By performing the fit with the impact parameter distributions generated for different B lifetimes, we obtain a $\pm 5.0\%$ fractional change on $f_{b\bar{b}}$.

• Resolution difference between a Monte Carlo and data

We use the Monte Carlo model for the SVX impact parameter resolution for bottom muons and charm muons. In addition, the Monte Carlo resolution for the SVX impact parameter is corrected for the resolution difference between the Monte Carlo jet data and CDF jet data as discussed in Chapter 4.2. To study the systematic due to the resolution difference for bottom muons, we take the original Monte Carlo resolution as a lower bound for the CDF resolution and determine the $b\bar{b}$ fraction using the unsmeared impact parameter distribution (Figure 4.6) for bottom muons. The $b\bar{b}$ fraction is found to be 0.557 ± 0.024 and we assign a $+7.1\%$ systematic uncertainty.

• Fraction of sequential muons

In Chapter 8.2, the fraction of sequential muons is estimated to be 0.123 ± 0.015 where the uncertainty comes from the b fragmentation and the branching ratios of semileptonic decays of charm and bottom hadrons. As explained in Chapter 4.2, we include sequential muons in the impact parameter distribution for bottom muons. By varying the sequential fraction in the distribution, the $b\bar{b}$ fraction changes by $\pm 0.3\%$ due to the resemblance of the impact distribution for direct and sequential muons.

• Impact parameter distributions for prompt and DIF muons

We use jet data to model the impact parameter distributions of prompt and DIF muons. As shown in Figure 4.4, the representative impact parameter distribution of

jet tracks is slightly different from that of DIF muons. To study the effect of DIF muons, we measure $b\bar{b}$ fractions with the distribution of DIF muons and jet tracks respectively and compare the results. For $P_T \geq 3\text{GeV/c}$, we obtain 0.515 ± 0.020 for

Source	Systematic Uncertainty
B lifetime	$\pm 5.0\%$
resolution difference	$+7.1\%$
sequential fraction	$\pm 0.3\%$
jet tracks	$+0.5 - 1.0\%$
charm muons	$+4.7\%$
Total	$+9.9 - 7.0\%$

Table 4.1: Systematic uncertainties of the fit

$f_{b\bar{b}}$ with DIF muons and 0.520 ± 0.022 with jet tracks. As discussed in Chapter 4.2, there are some tracks from bottom and charm decays in the jet data. We subtract the contribution of charm and bottom tracks from the jet data and perform the fit with the subtracted distribution for prompt muons. The variation of the $b\bar{b}$ fraction is found to be $+0.5\%$. These small systematic errors from the uncertainties in the impact parameter distribution for prompt muons can be explained by the fact that the $b\bar{b}$ fraction is mainly determined in the large impact parameter region as shown in Figure 4.16 and in this region where the contribution of prompt muons is small, the variations of the distribution for prompt muons do not affect the $b\bar{b}$ fraction significantly.

- Charm muons

In the two dimensional fitting method, we assume that the $c\bar{c}$ events and the events with a bottom muon and a prompt muon contribute equally. For the study of the systematics, we study the two extreme cases. In the first case, we include only $c\bar{c}$ component in H_{sum} and perform the fit ($A_1 = 0$). In the other case, we include only dimuon events with a bottom muon and a prompt muon in H_{sum} ($A_2 = 0$). The fractional change of $f_{b\bar{b}}$ is found to be $\pm 4.7\%$. In the likelihood function, we do not include the events with a charm muon and a prompt muon. The inclusion of

this component in the likelihood function negligibly affects the $b\bar{b}$ fraction since the two-dimensional distribution for these events is very similar to that of the events with two prompt muons. For example, the $b\bar{b}$ fraction changes by 0.3% even if we set the fraction of such events to be 20% in the fit.

To summarize, Table 4.1 lists the systematic uncertainties from various sources. The total systematic uncertainty is estimated to be $+9.9\% - 7.0\%$.

Chapter 5

Central Muon Upgrade (CMP) Efficiency Method

In this chapter, we present another independent method to obtain the $b\bar{b}$ fraction in order to check the result of the impact parameter fit. It gives the $b\bar{b}$ fraction in like-sign (LS) dimuon events only and is not used in the measurements presented in the following sections.

5.1 Principle

Reconstructed muons in the central muon detector (CMU) [39] consist of *real* muons and *fakes*. *Real* muons are defined as muons from b or c semileptonic decays, the Drell Yan process, and Υ decay. *Fakes* are defined to be not *real* and include muons from π or K decays (DIF) and hadronic punchthroughs identified as muons. Reconstructed muons in the CMU detector pass through an additional 3 absorption lengths of material (iron) and may or may not make muon segments in the central muon upgrade detector (CMP) [40]. The probability of making a muon segment in the CMP detector, called the CMP efficiency, is different for *real* muons and *fakes*. For *real* muons, it is expected to be close to 100% due to the small absorption rate of muons for $P_T \geq 3$ GeV/c. For *fakes*, most of the hadronic punchthroughs are absorbed inside the iron as explained in Chapter 2.5 and most of DIF muons pass

through the iron to the CMP detector. The CMP efficiency for *fakes* may be very different from that for *real* muons, depending on the relative fractions of DIF muons and hadronic punchthroughs. The principle of this method is to fully exploit the difference of the CMP efficiencies between *real* muons and *fakes* in order to obtain the fraction of *real* dimuons in like-sign(LS) dimuon events. In like-sign events, only $b\bar{b}$ pairs can generate *real* dimuon events via sequential decay ($b \rightarrow c \rightarrow \mu$) or $B^0\bar{B}^0$ mixing and we directly obtain the $b\bar{b}$ fraction from the fraction of *real* dimuon events.

The data sample for the CMP efficiency method is different from the data sample used in the impact parameter fitting method. We require neither a SVX track nor a muon segment in the CMP detector for muons and only $\mu^-\mu^-$ events are used.

muon	$P_T \geq 3.0 GeV/c$
	CMU $\chi^2_{r-\phi} \leq 9.0$
	CMU $\chi^2_z \leq 12.0$
	CMP $\chi^2_{r-\phi} \leq 9.0$
	CMU muon segment
	Geometrical coverage by the CMP detector
event	Dimuon trigger
	event vertex $\lvert z \rvert \leq 30.0$cm
	dimuon mass$\geq 5.0 GeV/c^2$
	$\mu^-\mu^-$ events

Table 5.1: Dimuon event selection cuts

In addition, in order to apply the CMP efficiency method, a muon is required to be covered geometrically by the CMP detector. The event selection cuts used in the CMP efficiency method are listed in Table 5.1.

We count the number of dimuon events with both muons having a muon segment in the CMP detector (N_{2cmp}), events with only one of muons having a muon segment in the CMP detector (N_{1cmp}), and events with neither of muons having a muon segment in the CMP detector (N_{0cmp}). With the CMP efficiency for *real* muons (ϵ_μ) and the CMP efficiency for *fakes* (ϵ_f), we construct three equations

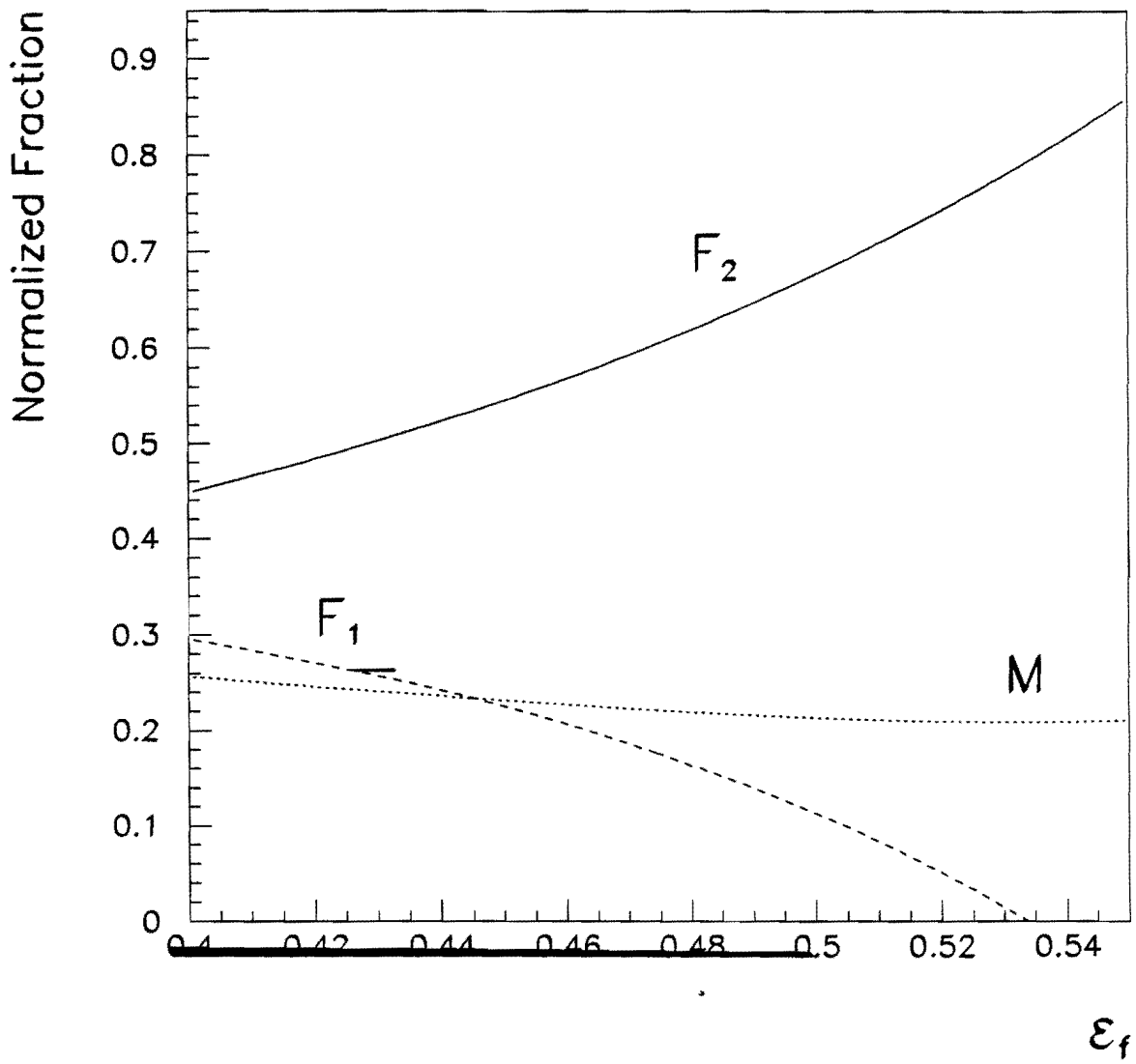

Figure 5.1: Normalized fractions of *real* dimuon (M) and fake dimuons (F_1 and F_2) as a function of the CMP efficiency for *fakes*, ϵ_f. There exists an upper bound (~ 0.53) on ϵ_f in order to have $F_1 \geq 0$.

for the above three different types of dimuon events (to be called dimuon equations) :

$$N_{0cmp} = (1-\epsilon_\mu)^2 M + (1-\epsilon_\mu)(1-\epsilon_f)F_1 + (1-\epsilon_f)^2 F_2 \tag{5.1}$$

$$N_{1cmp} = 2\epsilon_\mu(1-\epsilon_\mu)M + \{\epsilon_\mu(1-\epsilon_f) + \epsilon_f(1-\epsilon_\mu)\}F_1 + 2\epsilon_f(1-\epsilon_f)F_2 \tag{5.2}$$

$$N_{2cmp} = \epsilon_\mu^2 M + \epsilon_\mu\epsilon_f F_1 + \epsilon_f^2 F_2 \tag{5.3}$$

where the number of *real* dimuon events (*i.e.* $b\bar{b}$ dimuon events) is represented by M and the number of *fake* dimuon events by F. The subscript of F denotes the number of *fakes* in an event. The meaning of the above equations is straightforward once we recall the definition of CMP efficiencies. In the second equation, the factor 2 is due to combinatorics.

From the data we have a total of 3423 $\mu^-\mu^-$ events consisting of 592 events for N_{0cmp}, 1430 events for N_{1cmp}, and 1401 events for N_{2cmp}. There are 5 unknowns in the above 3 equations: ϵ_μ, ϵ_f, M, F_1, and F_2. The CMP efficiency for *real* muons, ϵ_μ, is measured to be 0.94 ± 0.01 using dimuon events from $J/\psi \rightarrow \mu^+\mu^-$ decay, which will be discussed in the next section.

By solving the equations given the numbers available M, F_1, and F_2 can be expressed as a function of ϵ_f as shown in Figure 5.1 (see appendix A). As shown in Figure 5.1, M is very insensitive to ϵ_f while F_1 and F_2 change rapidly. It also shows that there exists an upper bound on ϵ_f in order to have a physical solution for F_1. The CMP efficiency for *fakes*, ϵ_f, is bounded from above analytically (~ 0.53). In Chapter 5.3, we will discuss a determination of a lower bound for ϵ_f.

5.2 ϵ_μ

For a measurement of ϵ_μ, we use a dimuon data sample from $J/\psi \rightarrow \mu^+\mu^-$ decay, which is one of the standard data sets for CDF analyses. For the selection of J/ψ data for the measurement, we apply a dimuon invariant mass cut, $2.9GeV/c^2 < M_{\mu\mu} < 3.3GeV/c^2$, and the other cuts listed in Table 5.1. Consequently about 15,000 J/ψs are selected as shown in Figure 5.2. The signal band ($3.0GeV/c^2 < M_{\mu\mu} < 3.2GeV/c^2$) and two side bands ($2.9GeV/c^2 < M_{\mu\mu} < 3.0GeV/c^2$, $3.2GeV/c^2 < M_{\mu\mu} < 3.3GeV/c^2$

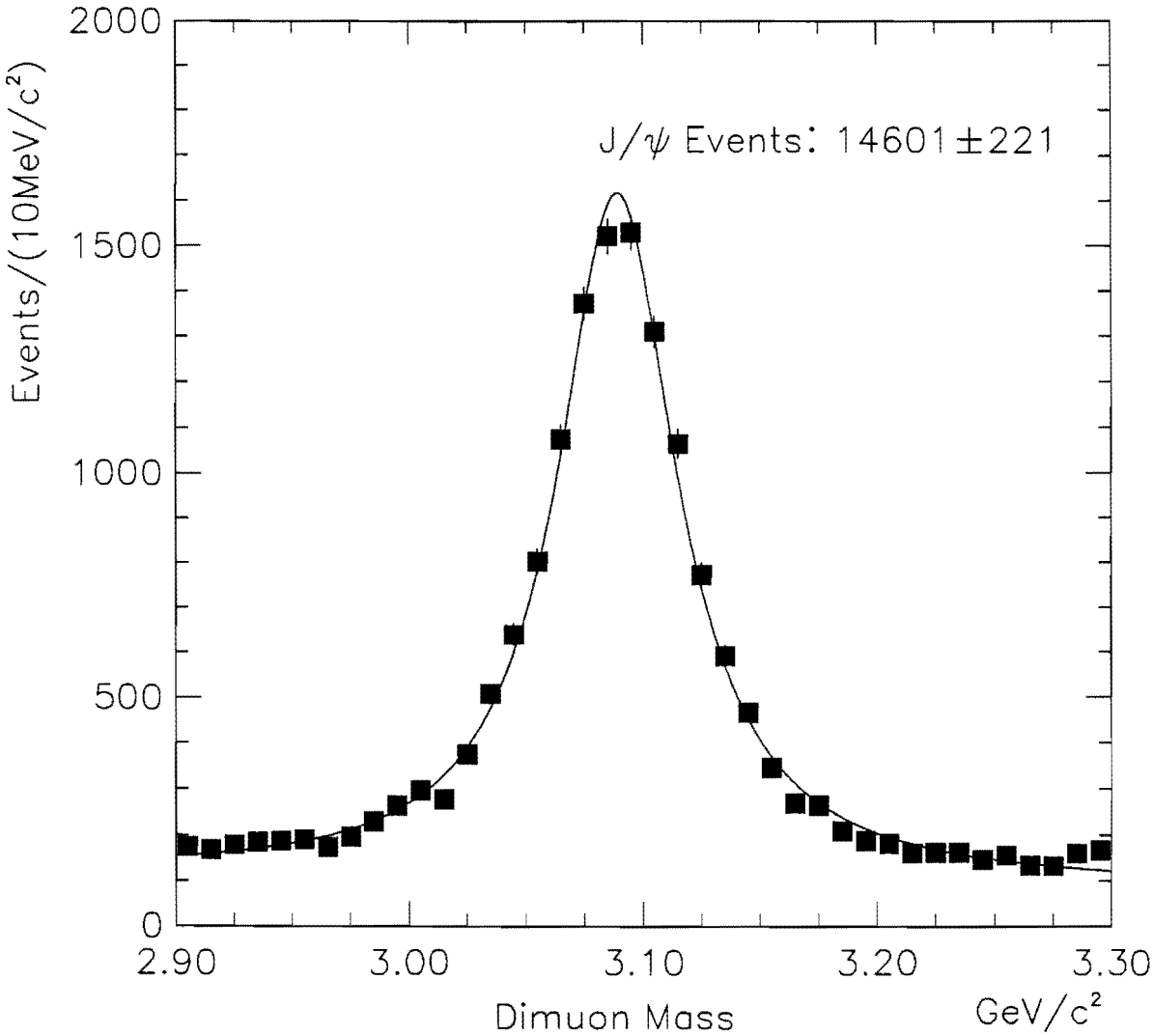

Figure 5.2: Distribution of dimuon invariant mass. We fit the data with a Gaussian function and a flat background.

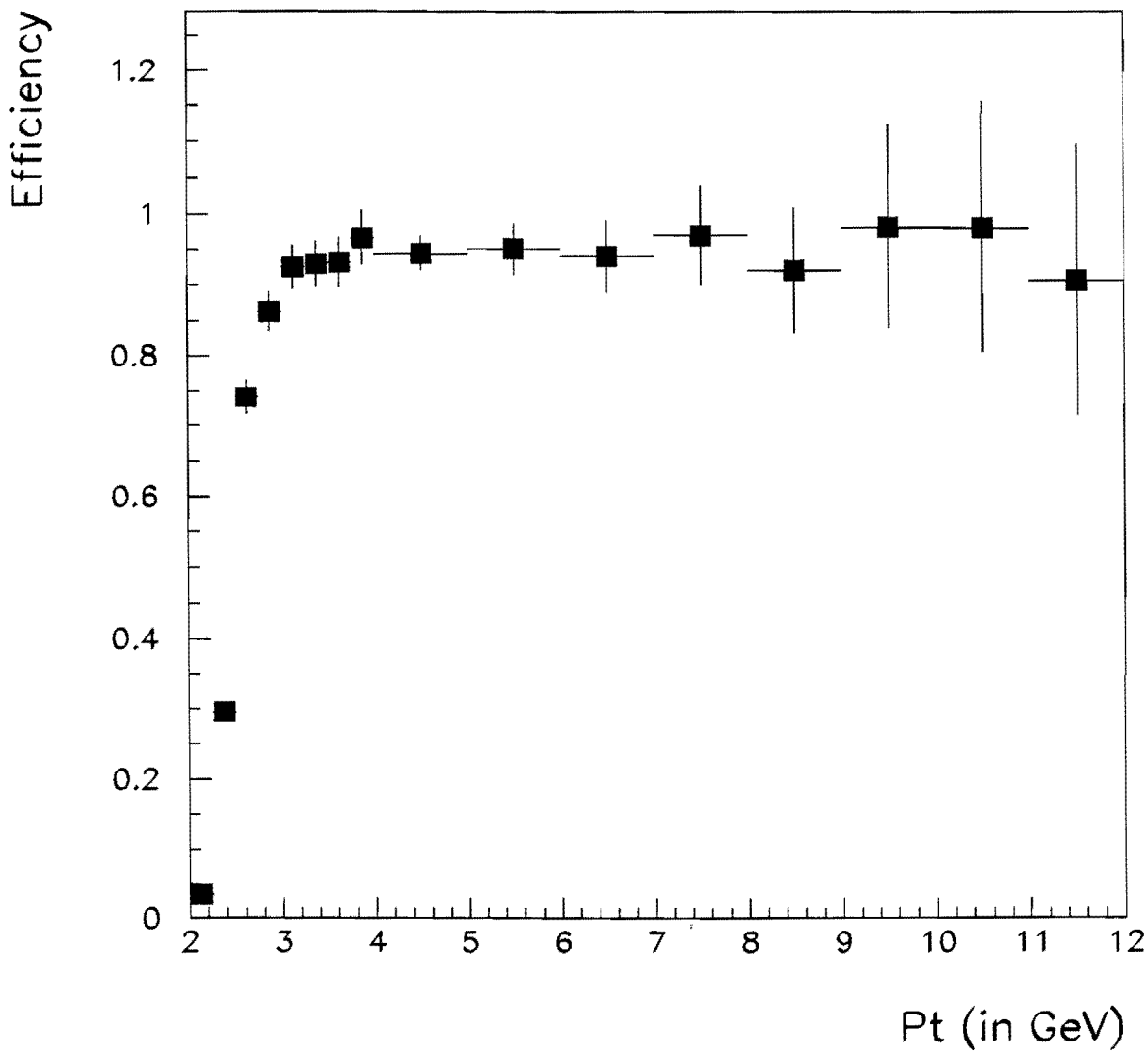

Figure 5.3: The CMP efficiency for *real* muons, ϵ_μ, as a function of P_T.

) are defined. The numbers of J/ψ muons for various constraints are determined by subtracting the number of side band muons from that of the signal band muons as follows:

$$\epsilon_\mu = \frac{N^{cmp}_{signal} - N^{cmp}_{side}}{N_{signal} - N_{side}} \tag{5.4}$$

N^{cmp}_{signal} = Number of Muons having a CMP segment in signal band
N^{cmp}_{side} = Number of Muons having a CMP segment in side bands
N_{signal} = Number of Muons in signal band
N_{side} = Number of Muons in side bands

The CMP efficiency, ϵ_μ is shown as a function of P_T in Figure 5.3. We note that ϵ_μ is nearly independent of P_T above 3 GeV/c. We take the average efficiency above 3 GeV/c as ϵ_μ. The effect of the initial rise of efficiency curve is negligible. For $P_T \geq$ 3GeV/c, we obtain $\epsilon_\mu = 0.94 \pm 0.01$ where the error comes from the statistics of the J/ψ data. The P_T independence of the CMP efficiency is also valid for *fakes* as will be shown in the next section. Therefore the dimuon equations are independent of P_T for $P_T \geq$ 3GeV/c.

5.3 ϵ_f

In this section, we try to set a lower bound for ϵ_f using a sample of *fakes* and a Monte Carlo simulation.

In order to obtain a sample consisting of *fakes*, we consider $K^0_S \rightarrow \pi^+\pi^-$ decay. One of the daughter pions may generate a muon signal in the muon detector via DIF or punchthrough. If there is another muon in the same event from the processes listed in Chapter 3.2, the event may be reconstructed as a dimuon event. We select a sample of pionic *fakes* from dimuon data by reconstructing K^0_S events with a negatively charged muon candidate and a positively charged track. Clearly a muon leg of a K^0_S event is a pure *fake* originated from pions.

The cuts used for the reconstruction of K^0_S events are listed in Table 5.2. By requiring the decay length of K^0_S vertex to be less than the inner radius of the CTC (~30cm), we avoid the decays of K^0_S to pions inside the CTC volume and thus select

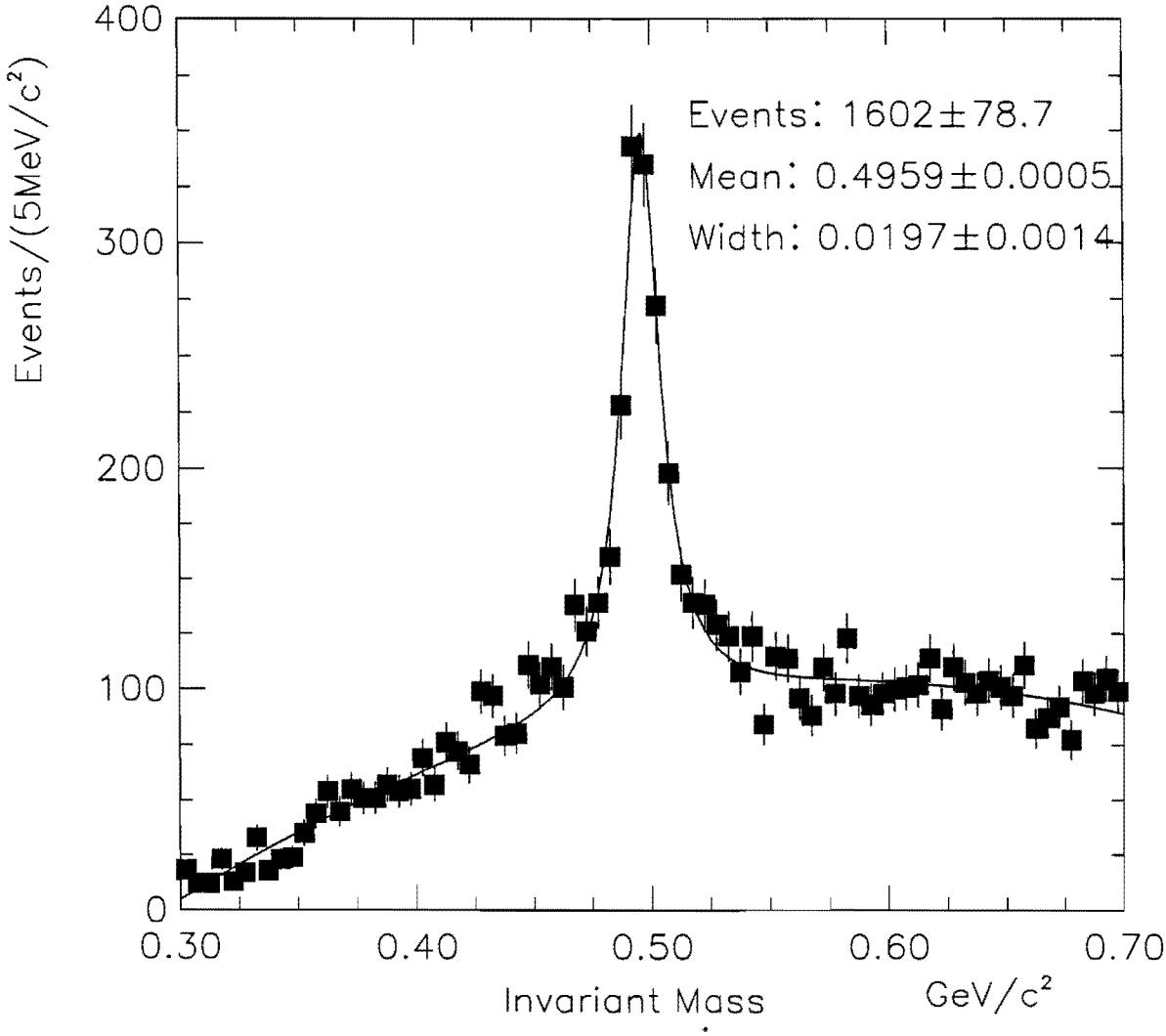

Figure 5.4: Invariant mass of a negatively charged muon and a positively charged track.

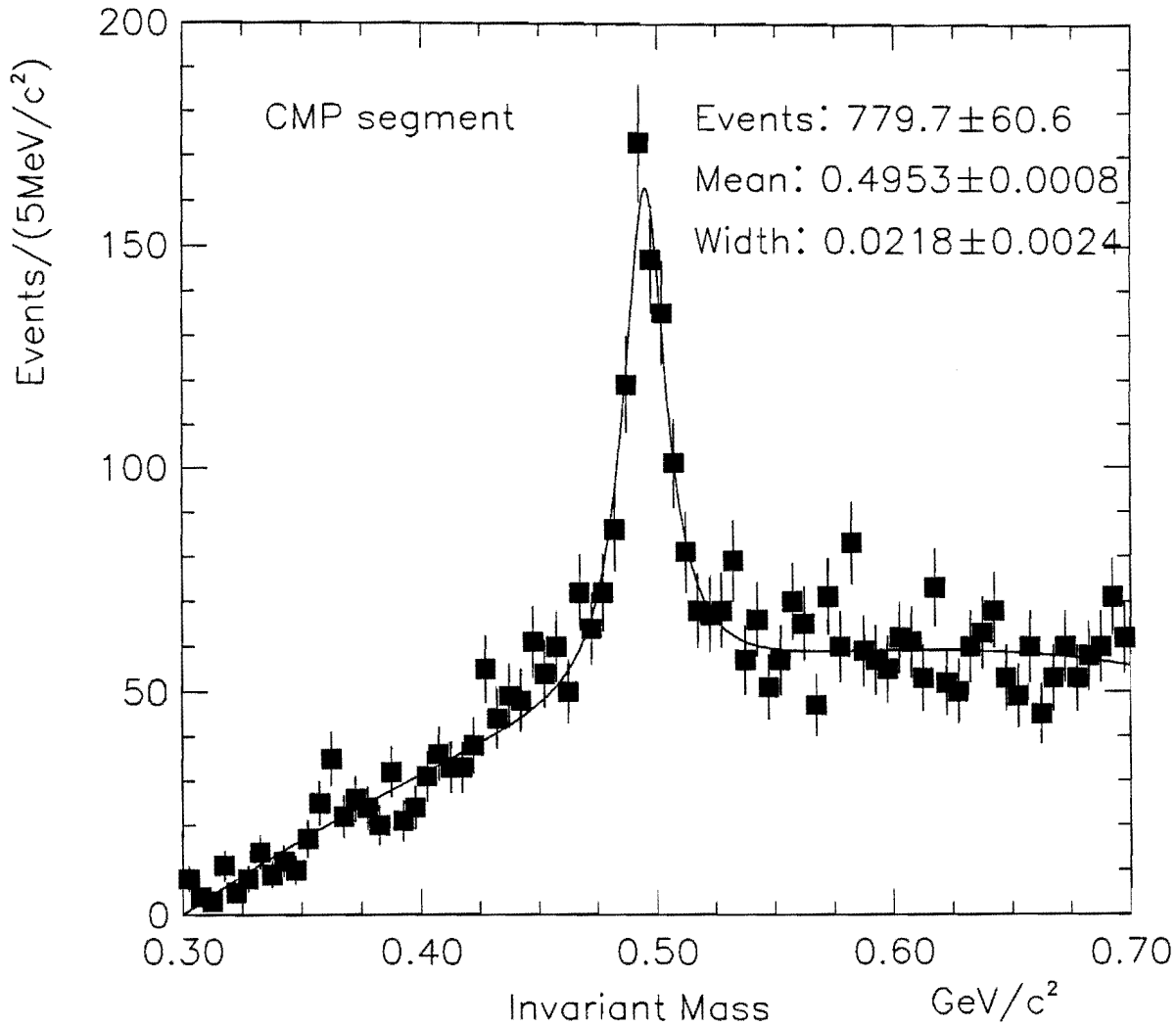

Figure 5.5: Invariant mass of a negatively charged muon and a positively charged track. A muon segment in the CMP detector is additionally required for a muon.

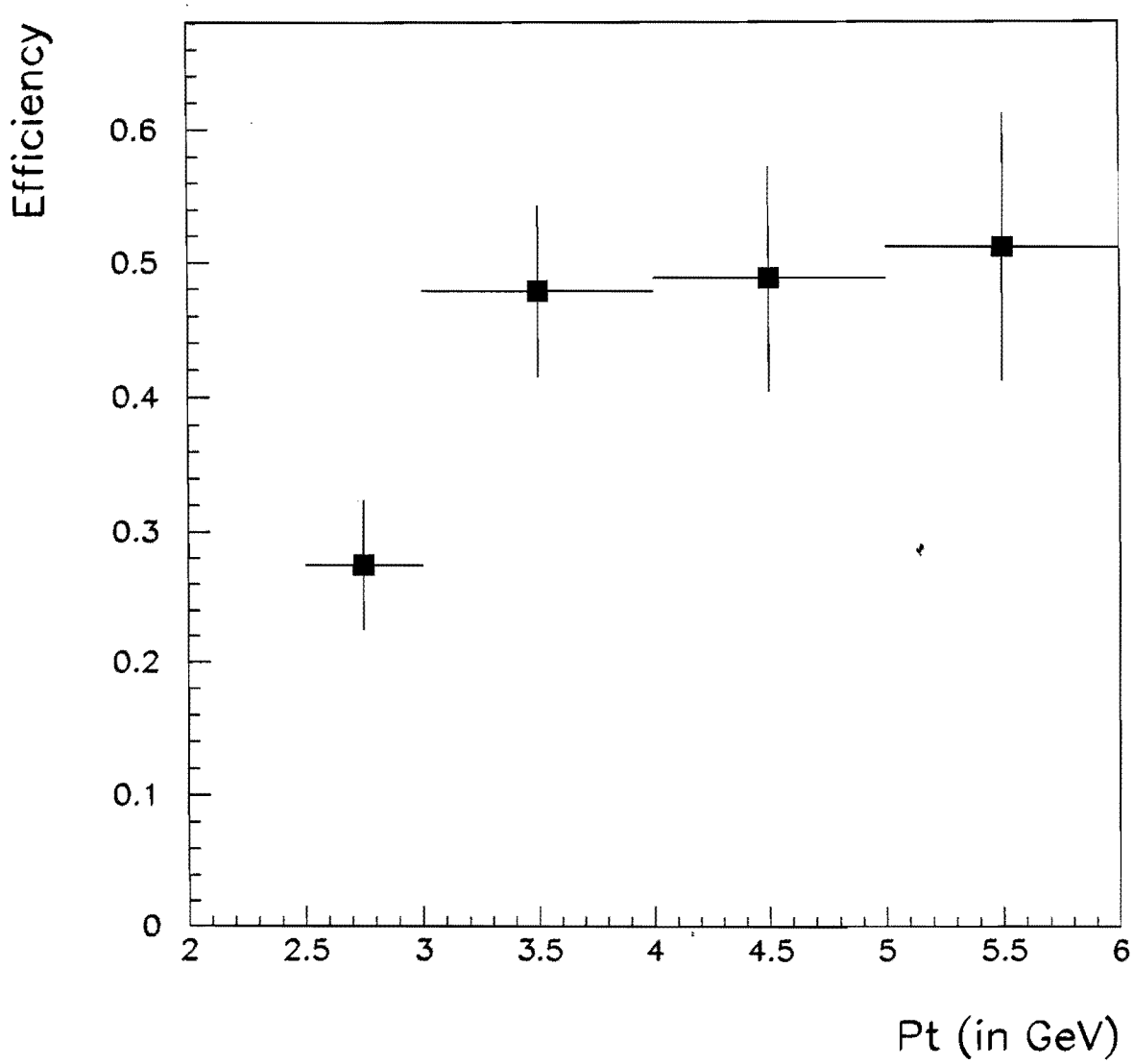

Figure 5.6: The CMP efficiency of pionic *fakes* from K_S^0 decays as a function of P_T.

muon	$P_T \geq 3.0 GeV/c$ CMU $\chi^2_{r-\phi} \leq 9.0$ CMU $\chi^2_z \leq 12.0$ CMP $\chi^2_{r-\phi} \leq 9.0$ CMU muon segment Geometrical coverage by the CMP detector negatively charged
track	CTC impact parameter$\geq$ 0.1cm positively charged
Vertex	$5.0cm \leq$ decay length $\leq$ 25.0cm

Table 5.2: K^0_S reconstruction cuts

decay pions which closely resemble prompt pions. Because of the large decay length of K^0_S ($\sim$2.7cm) [75], the impact parameter of the decay pions tends to be larger. Therefore the impact parameter cut is very effective in reducing the combinatorial backgrounds from prompt particles and keeping the K^0_S signal.

Figures 5.4 and 5.5 show the invariant mass distribution. In Figure 5.5, a CMP muon segment is required for a muon leg. The CMP efficiency of pionic *fakes* from K^0_S decays is measured by taking the ratio of the numbers of K^0_S events in both cases. The efficiency is shown as a function of P_T in Figure 5.6. In the Figure, it is noted that the efficiency is almost independent of P_T above 3 GeV/c within statistical uncertainties. For $P_T \geq$ 3GeV/c, the average CMP efficiency for pionic *fakes* from K^0_S decay is found to be 0.49 ± 0.04 where the error results from the statistical uncertainty of the K^0_S sample.

Now we turn to the question whether we can use the above CMP efficiency for ϵ_f. ϵ_f can be written as

$$\epsilon_f = f_{DIF}\epsilon_{DIF} + f_{HP}\epsilon_{HP} \tag{5.5}$$

where f's are normalized fractions of DIF muons or hadronic punchthrough and ϵ's are the corresponding CMP efficiencies.

To estimate the CMP efficiency of DIF muons, we use a Monte Carlo simulation mentioned in Chapter 3.4. In the simulation, we force kaons and pions to decay inside

the detector volume to get more statistics. Table 5.3 shows the results for each P_T bin. From the results, we conclude that $\epsilon^K_{DIF} \cong \epsilon^\pi_{DIF}$. The efficiencies are closer to

P_T of DIF muons	π DIF	K DIF
3-6GeV/c	0.71 ± 0.04	0.72 ± 0.08
6-9GeV/c	0.92 ± 0.04	0.89 ± 0.07
9-12GeV/c	0.92 ± 0.04	0.91 ± 0.07

Table 5.3: ϵ_{DIF}

ϵ_μ (~ 0.94) as P_T increases, which is explained by the fact that the decay angle (or kink) of DIF muons with respect to the parent meson direction becomes smaller, and DIF muons more closely resemble *real* muons of prompt origin as P_T increases. The punchthrough probability of a K^- is experimentally known to be almost equal to that of a π^-, which means that $\epsilon^{K^-}_{HP} \cong \epsilon^{\pi^-}_{HP}$.

The proper life time of the kaon is 2.1 times shorter than that of the pion [51, 52]. Also, the kaon mass is 3.54 times heavier than the pion mass, which means that for fixed P_T, the relativistic boost of the pion is 3.54 times larger than that of the kaon. Consequently the probability of kaon decay before the CMU detector is 7.4 times higher than that of pion decay. However the CDF offline tracking removes some of DIFs which have measurable kinks inside the CDF tracking system as discussed in Chapter 4.2. Because of the large Q value in kaon decays, the tracking algorithm is expected to be more effective in removing kaon DIFs. To study this effect, we employ Monte Carlo methods. In the Monte Carlo, we generate 100,000 pions and kaons at given P_T with uniform pseudo rapidity distribution [76] for $|\eta| < 0.8$. After the offline reconstruction and selection cuts for muons in Table 5.1, we find (from the Table 5.4) the decay probability of a kaon is expected to be higher than that of a pion while the punchthrough probabilities are almost same for a π^- and a K^- [77]. In other words, $f^{K^-}_{DIF} > f^{\pi^-}_{DIF}$, which means that the CMP efficiency of a K^- fake should be higher than that of a π^- fake. Therefore once we measure the CMP efficiency of π^- fakes, it provides a lower bound on ϵ_f. We can not apply the same argument to positively charged *fakes* since the the punchthrough of a K^+ is higher than that of a π^+. That

P_T	3 GeV/c	6 GeV/c	9 GeV/c
π	153	124	85
K	252	223	180

Table 5.4: Number of DIF muons after the selection

is the reason why only $\mu^-\mu^-$ events are used in this method.

In summary, we conclude that the CMP efficiency, which is measured using K_S^0 sample, serves as a lower bound on ϵ_f. Combined with the upper bound ($\cong 0.53$) obtained in Chapter 5.1,

$$\epsilon_f = 0.49 \pm 0.04$$

5.4 Result

Using the measured values of ϵ_μ and ϵ_f, we solve the dimuon equations (see Appendix A) and calculate the number of *real* dimuon events (or $b\bar{b}$ dimuon events), M, in $\mu^-\mu^-$ events. We obtain 736 ± 89 events for M where the uncertainty represents the statistical uncertainty in the data and the systematic uncertainty of the measured CMP efficiencies.

For a comparison with the result of the two-dimensional fitting method, we convert the above number to the number of $b\bar{b}$ events in the like-sign dimuon data sample where a muon is required to have a muon segment in the CMP detector and a track in the silicon vertex detector (SVX) as described in Chapter 4.3. From the assumption of charge symmetry for $b\bar{b}$ dimuon events, we can assume $M^{--} = M^{++}$. Therefore the number of $b\bar{b}$ events in the standard like-sign dimuon data, $N_{b\bar{b}}^{ls}$, can be calculated using the following relation.

$$N_{b\bar{b}}^{ls} = 2 \cdot M \cdot \epsilon_\mu^2 \cdot \epsilon_{svx} \cdot \epsilon_{imp} \tag{5.6}$$

where the CMP efficiency ϵ_μ is found to be 0.94 ± 0.01, track finding efficiency in the SVX for $b\bar{b}$ dimuons, ϵ_{svx}, is found to be 0.669 ± 0.024, and the impact parameter

cut efficiency for $b\bar{b}$ dimuons, ϵ_{imp}, is found to be 0.921 ± 0.006. The relevant SVX efficiencies will be discussed in Chapter 6. With these efficiencies, we obtain 801 ± 102 $b\bar{b}$ events in the standard like-sign dimuon events, which is in good agreement with the result of the impact parameter fit (838 ± 53 events from Chapter 4.2). The result independently confirms the validity of the two dimensional impact parameter fitting method.

Chapter 6

Total $b\bar{b}$ Cross Section

In this chapter, we present a measurement of the $b\bar{b}$ cross section with different P_T thresholds for the $\bar{b}$ quark in order to study the kinematic correlation in $b\bar{b}$ production. For the measurement, there are three exclusive data sets representing three distinct intervals in $P_T(\mu_{\bar{b}})$ with $P_T(\mu_b) \geq 3$ GeV/c: 3 GeV/c $\leq P_T(\mu_{\bar{b}}) \leq 5$ GeV/c, 5 GeV/c $\leq P_T(\mu_{\bar{b}}) \leq 7$ GeV/c, and $P_T(\mu_{\bar{b}}) \geq 7$ GeV/c. We assign the two muons in the event to the two bottom quarks in such a way that the assignment procedure introduces no kinematical bias. Specifically, we randomize the ordering of the muons so that the muons can be treated equally. Due to the kinematic symmetry of b and $\bar{b}$ quarks, we can assume that the first and the second muon are decayed from b and $\bar{b}$ respectively even though we do not tag the parent bottom quark explicitly. Each data set is used for a measurement of the total $b\bar{b}$ cross section with the corresponding P_T threshold for the $\bar{b}$ quark. The total $b\bar{b}$ cross section is given by

$$\sigma(p\bar{p} \rightarrow b\bar{b}X) = \frac{N_{b\bar{b}}}{L \cdot Br(b \rightarrow \mu)^2 \cdot \epsilon_{CDF} \cdot A} \tag{6.1}$$

where $N_{b\bar{b}}$ is the number of $b\bar{b}$ dimuon events and $Br(b \rightarrow \mu)$ is the branching ratio for the semileptonic decay of B hadron (0.103 ± 0.005) [49]. The integrated luminosity L for the data is $17.4 \pm 0.6 pb^{-1}$. A is the acceptance for $b\bar{b}$ dimuon events and ϵ_{CDF} is the combined detector and data selection efficiency.

6.1 $N_{b\bar{b}}$

In order to measure $N_{b\bar{b}}$, we use the two dimensional impact parameter fitting method discussed in chapter 4. In each data set, we perform the fit with the template histograms where the same P_T thresholds are applied for both muons. The fit results are listed in Table 6.1. For a comparison between the data and fitted distribution,

$P_T(\mu_b)$	$P_T(\mu_{\bar{b}})$	N_{bb}
$\geq$ 3GeV/c	3 - 5GeV/c	$1610 \pm 87(stat)^{+160}_{-113}(sys)$
	5 - 7GeV/c	$495 \pm 46(stat)^{+49}_{-35}(sys)$
	$\geq$ 7GeV/c	$368 \pm 36(stat)^{+36}_{-26}(sys)$

Table 6.1: Fit results

we plot the projections of the two dimensional histograms onto one axis in Figure 6.1 which show a good agreement over the whole range of the impact parameter. The systematic uncertainties in each fit are correlated as discussed in chapter 4.4.

6.2 Acceptance

The acceptance, A, is defined to be the probability of muon pairs from $b\bar{b}$ decay passing through the muon detectors and satisfying the muon P_T constraints which are described in chapter 6.1.

We define the corresponding P_T thresholds of bottom quarks, P_T^{min}, as the value such that 90% of muons satisfying the P_T requirements come from bottom decays with $P_T \geq P_T^{min}$. The values of P_T^{min} are estimated by a Monte Carlo simulation. The Monte Carlo program generates bottom quarks using the input spectra from the next-to-leading order QCD calculation of $b\bar{b}$ production [5]. The generated quarks are fragmented to B hadrons using the Peterson fragmentation function [60] with $\epsilon = 0.006$ [61]. The B hadron decays are generated by the CLEO Monte Carlo program QQ [62]. For $P_T(\mu_b) \geq 3$ GeV/c, the corresponding P_T^{min} for the b quark is found to be 6.5 GeV/c. The P_T^{min} values for the $\bar{b}$ quark are determined to be

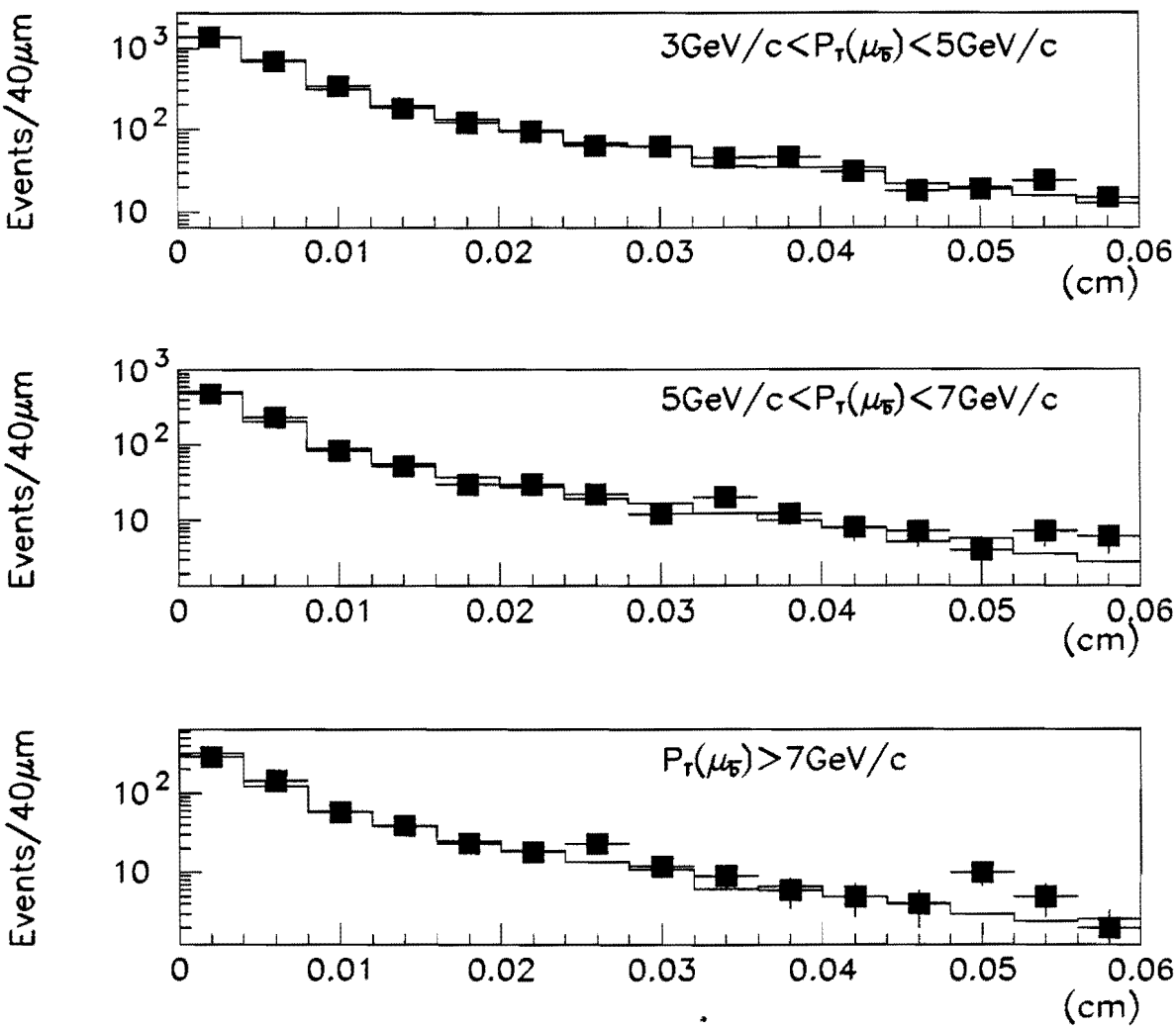

Figure 6.1: Projections of the two dimensional impact parameter distributions for each data sample. The solid line represents the fitted distribution and the filled boxes with an error bar represent the data distribution.

6.5, 8.75, and 12.25 GeV/c respectively for the P_T constraints on the $\mu_{\bar{b}}$: 3 GeV/c $\leq P_T(\mu_{\bar{b}}) \leq$ 5 GeV/c, 5 GeV/c $\leq P_T(\mu_{\bar{b}}) \leq$ 7 GeV/c, and $P_T(\mu_{\bar{b}}) \geq$ 7 GeV/c (see Figure 6.2). In addition, the rapidity of b and $\bar{b}$ quarks is required to be between -1.0 and 1.0 in order to include all of the bottom muons which pass through the CMU and CMP detectors as shown in Figure 6.3.

Following the definition of P_T^{min}, the dimuon acceptance, A, can be written as:

$$A = \frac{N_1}{N_2} \tag{6.2}$$

where N_1 is the number of $b\bar{b}$ dimuon events satisfying the muon P_T constraints and the CMU/CMP fiducial requirements and N_2 is the number of $b\bar{b}$ dimuon events with $P_T(b) \geq P_T^{min}(b)$, $P_T(\bar{b}) \geq P_T^{min}(\bar{b})$, and $|y(b)|, |y(\bar{b})| \leq 1$.

The same Monte Carlo program is used to estimate the acceptance. In the Monte Carlo simulation, muons from semileptonic decays of B hadrons, including sequential B muons are selected with the P_T requirements and propagated to the muon detectors. The results are shown in Table 6.2. The systematic uncertainty of the acceptance

$P_T(\mu_b)$	$P_T(\mu_{\bar{b}})$	A
$\geq$ 3GeV/c	3 - 5GeV/c	$1.32 \pm 0.13(sys)\%$
	5 - 7GeV/c	$0.55 \pm 0.05(sys)\%$
	$\geq$ 7GeV/c	$0.61 \pm 0.06(sys)\%$

Table 6.2: Acceptance

comes from the uncertainty of the fragmentation and the fraction of sequential B muons. Changing the Peterson fragmentation parameter [61] by ± 0.002 results in a $\pm 9\%$ uncertainty of the acceptance independent of P_T. The acceptance consists of three components depending on the sources of $b\bar{b}$ dimuon events: one with two direct decay muons, one with a sequential and a direct muon, one with two sequential decay muons. The fraction of sequential decay muons is estimated with the Monte Carlo simulation and found to be 0.123 ± 0.125 for $P_T(\mu_b) \geq$ 3GeV/c and 0.138 ± 0.017, 0.099 ± 0.012, and 0.073 ± 0.009 for 3GeV/c $\leq P_T(\mu_{\bar{b}}) \leq$ 5GeV/c, 5GeV/c $\leq P_T(\mu_{\bar{b}}) \leq$ 7GeV/c, and $P_T(\mu_{\bar{b}}) \geq$ 7GeV/c respectively where the errors come from

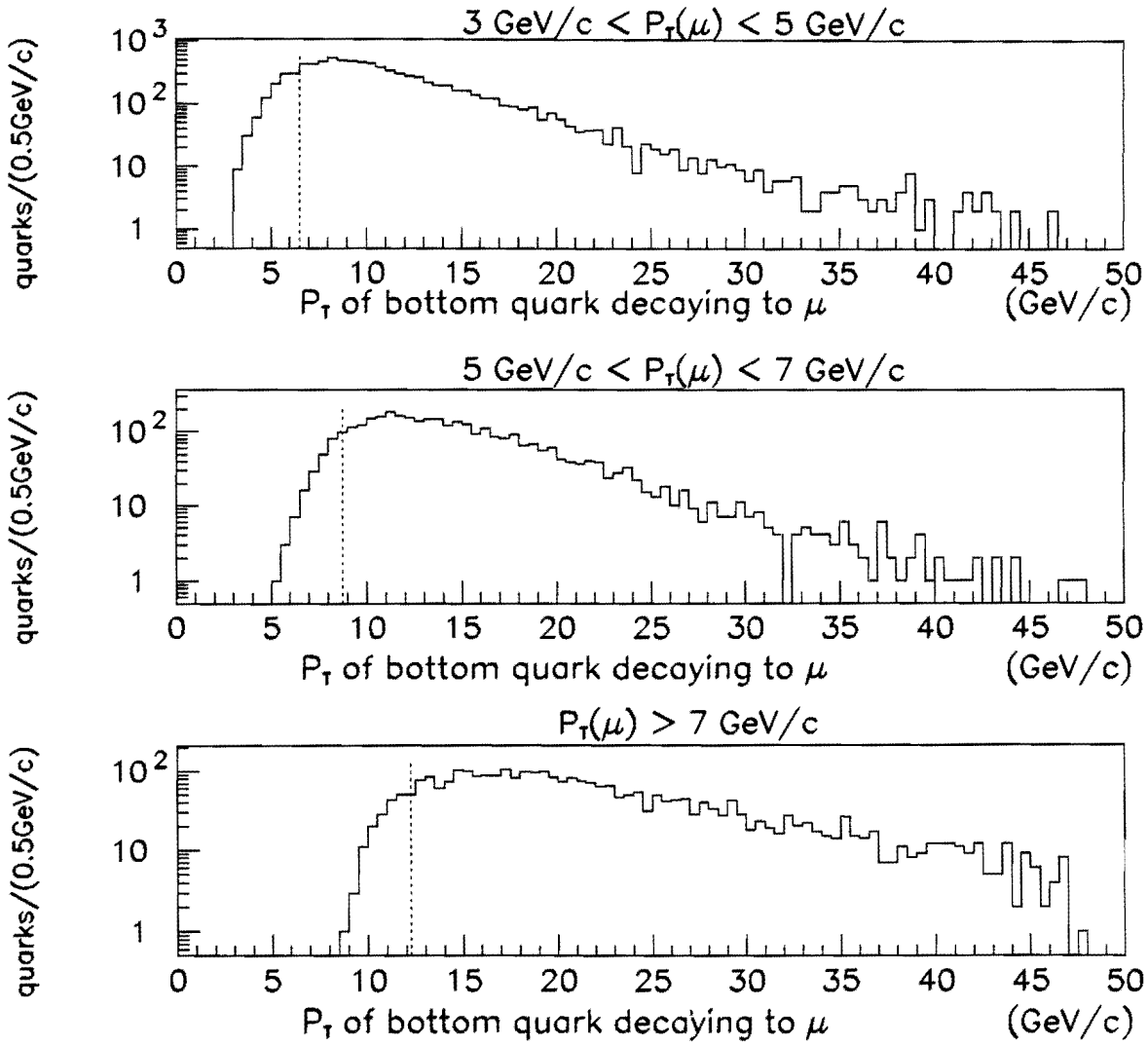

Figure 6.2: P_T distribution of $\bar{b}$ quarks decaying to μ with each P_T constraint on muon. The dotted line represents the value of P_T^{min}.

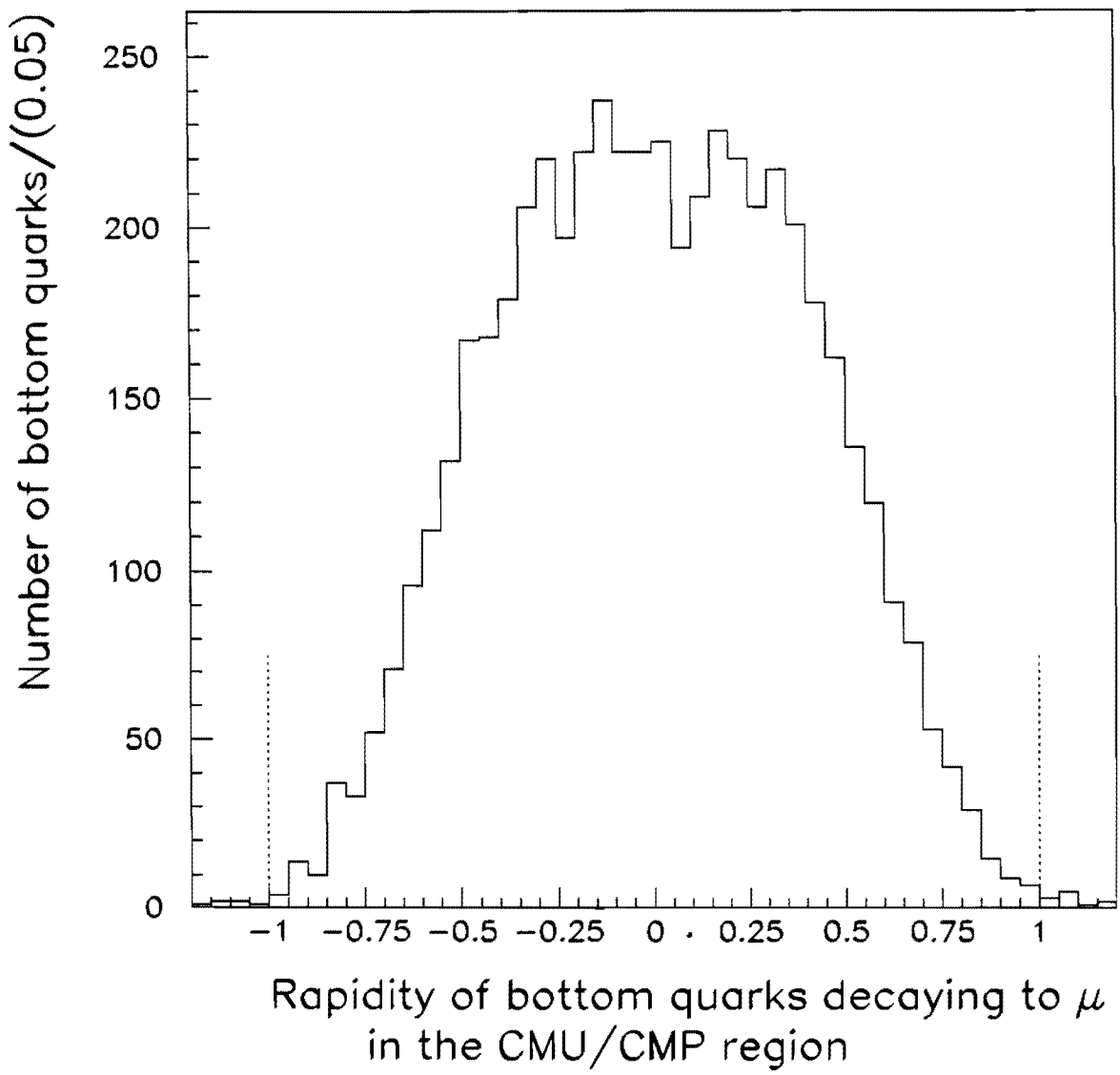

Figure 6.3: Rapidity, y, distribution of bottom quarks decaying to μ in the CMU/CMP fiducial region with $P_T \geq 3$ GeV/c.

the uncertainty in the relative branching ratio of bottom and charm semileptonic decays [49, 50] and the fragmentation, which will be discussed in chapter 8. The systematic uncertainty of the acceptance from sequential decay muons is measured to be $\pm 4\%$. In total, the systematic uncertainty of the acceptance is found to be $\pm 9.8\%$.

6.3 Efficiency

The efficiencies used in the data selection are defined to be multiplicative and the total efficiency, ϵ_{CDF}, can be factorized into the efficiencies of each of the data selection requirements as follows:

$$\epsilon_{CDF} = \epsilon_{z0} \cdot \epsilon_{ctc} \cdot \epsilon_{muon} \cdot \epsilon_{trig} \cdot \epsilon_{svx} \cdot \epsilon_{imp} \cdot \epsilon_{mass} \tag{6.3}$$

In this section, we describe the efficiencies of the individual selection requirements. The efficiencies of the trigger (ϵ_{trig}), impact parameter cut (ϵ_{imp}), and dimuon mass cut (ϵ_{mass}) exhibit a weak dependence on muon P_T as shown in Table 6.3. On the other hand, the CTC tracking (ϵ_{ctc}) and the muon identification efficiencies (ϵ_{muon}) are found to be independent of the muon P_T.

The efficiency of the event vertex requirement $|z_0| \leq 30$cm, ϵ_{z0}, is measured using a minimum bias data sample. The event vertex distribution in the data is parameterized with a Gaussian with a mean of $-1.48cm$ and width of $26.65cm$ [36]. The efficiency is found to be $74.2 \pm 2.1\%$ where the error results from the uncertainty in the longitudinal beam distribution [36].

The tracking efficiency in the CTC, ϵ_{ctc}, is determined by embedding the CTC hits of the Monte Carlo simulated muon tracks in the data sample and then counting the number of reconstructed muon tracks [78]. We measure the efficiency for $b\bar{b}$ dimuon events to be $96 \pm 2\%$.

This efficiency includes the efficiency of the muon matching and the muon detectors. The muon finding efficiency, ϵ_{muon}, is measured in a very similar way which is used for the measurement of the CMP efficiency in chapter 5.2. The dimuon invariant mass spectrum shows a Gaussian resonance peak at the value of the J/ψ mass with a flat background distribution as plotted in Figure 5.2. The number of J/ψ muons

is estimated by subtracting the side band (2.9 GeV/c^2 $\leq M_{\mu\mu} \leq$ 3.0 GeV/c^2, 3.2 GeV/c^2 $\leq M_{\mu\mu} \leq$ 3.3 GeV/c^2) from the J/ψ signal band (3.0 GeV/c^2 $\leq M_{\mu\mu} \leq$ 3.2 GeV/c^2). In order to determine the muon matching efficiency, we count the number of J/ψ muons before and after the matching requirements and, by taking the ratio of the two numbers, we measure the muon matching efficiency to be $98.7 \pm 0.2\%$. In a similar way, the muon reconstruction efficiency in the central muon detector [79, 80] including the CMP efficiency is determined to be $92.1 \pm 2.2\%$ where the uncertainty represents the statistical error only. The combined efficiency for dimuons is estimated $82.6 \pm 4.4\%$.

We also measure the trigger efficiency, ϵ_{trig}, using the side-band subtracted J/ψ sample. The measured trigger efficiency at each level is parameterized as a function of muon P_T [48], as shown in Figures 3.1 and 3.2, and convoluted with the P_T distribution of bottom muons to obtain the trigger efficiency for bottom muons. The combined Level 1, Level 2, and Level 3 dimuon trigger efficiencies are listed in Table 6.3 for each dimuon data set where the error comes from the uncertainty in the trigger parameterization.

The track finding efficiency in the SVX detector, ϵ_{svx}, is measured by subtracting distributions of like-sign dimuon events from those of opposite-sign events. In the sign-subtracted distributions, only the contributions of events from $b\bar{b}$ and $c\bar{c}$ decay, the Drell Yan process, and Υ decay remain and the contribution from *fake* dimuon events is not included since they equally contribute to opposite-sign and like-sign dimuons. From a Monte Carlo study, this efficiency is shown to be independent of event topology and represents the efficiency for $b\bar{b}$ dimuon events. This also represents a combined efficiency of the SVX track reconstruction and the SVX geometrical coverage for dimuons with $|z_0| \leq 30$cm. The dimuon track finding efficiency in the SVX detector is found to be $66.9 \pm 2.4\%$. The uncertainty results from the statistics of the data sample.

The efficiencies of the impact parameter requirement $|d| \leq 0.06$cm, ϵ_{imp}, are estimated by the Monte Carlo simulation discussed in Chapter 3.4. The results are shown in Table 6.3 and the errors are from the uncertainty of the average B lifetime [64], one of the input parameters of the Monte Carlo simulation.

$P_T(\mu_b)$ $P_T(\mu_{\bar{b}})$	$\geq$ 3GeV/c 3 - 5 GeV/c	$\geq$ 3GeV/c 5 - 7 GeV/c	$\geq$ 3GeV/c $\geq$ 7GeV/c
Event vertex	$74.2 \pm 2.1\%$	$74.2 \pm 2.1\%$	$74.2 \pm 2.1\%$
CTC track finding	$96.0 \pm 2.0\%$	$96.0 \pm 2.0\%$	$96.0 \pm 2.0\%$
Muon identification	$82.6 \pm 4.4\%$	$82.6 \pm 4.4\%$	$82.6 \pm 4.4\%$
SVX track finding	$66.9 \pm 2.4\%$	$66.9 \pm 2.4\%$	$66.9 \pm 2.4\%$
Trigger	$83.2 \pm 3.7\%$	$84.7 \pm 3.8\%$	$84.8 \pm 3.8\%$
Impact parameter cut	$91.7 \pm 0.6\%$	$92.5 \pm 0.6\%$	$93.0 \pm 0.6\%$
Dimuon mass cut	$90.6 \pm 0.1\%$	$94.0 \pm 0.1\%$	$95.2 \pm 0.1\%$
Combined Efficiency	$27.2 \pm 2.3\%$	$29.0 \pm 2.5\%$	$29.6 \pm 2.5\%$

Table 6.3: Efficiencies

The efficiency of the dimuon mass requirement $M_{\mu\mu} \geq 5\text{GeV}/c^2$, ϵ_{mass}, is obtained by the Monte Carlo simulation which is based on the next-leading-order MNR calculation [5] and is shown in Table 6.3.

6.4 Result

We measure the $b\bar{b}$ cross section for $P_T(b) \geq P_T^{min}(b)$, $P_T(\bar{b}) \geq P_T^{min}(\bar{b})$, and $|y_b|, |y_{\bar{b}}| \leq 1$ and the results are shown in Table 6.5. The systematics are summarized in Table 6.4. As seen in Table 6.5, the systematic errors are dominant and they are correlated for different measurements of $b\bar{b}$ cross section. The prediction of the next-to-leading

Source	Systematics
Impact Parameter Fit	$\pm^{9.9\%}_{7.0\%}$
Luminosity	$\pm 3.6\%$
Br(b$\rightarrow \mu$)	$\pm 9.7\%$
Acceptance	$\pm 9.8\%$
Efficiencies	$\pm 8.5\%$
Total	$\pm^{19.3\%}_{18.0\%}$

Table 6.4: Systematics of the cross section measurement

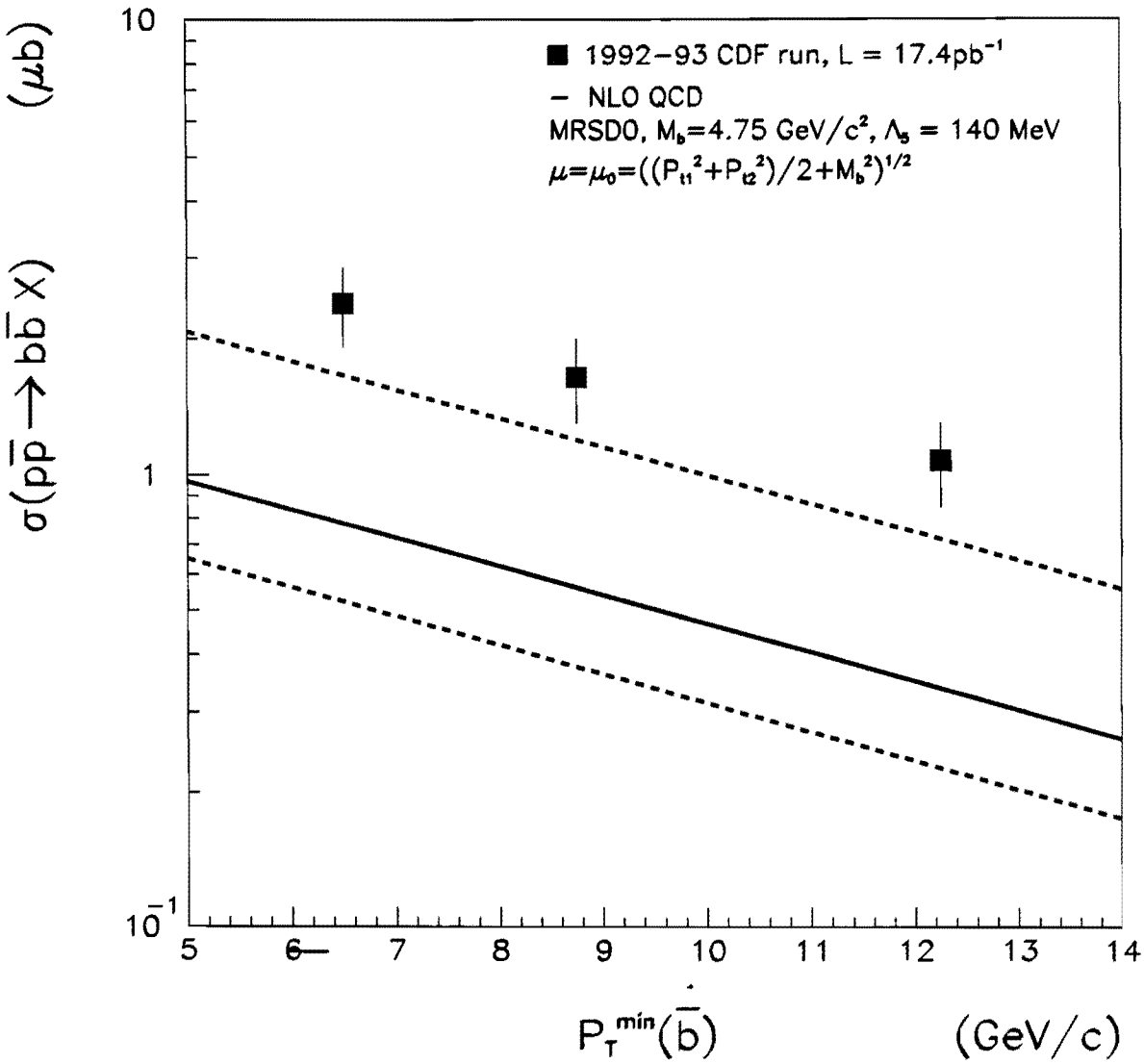

Figure 6.4: Total $b\bar{b}$ cross section with $P_T(b) \geq 6.5$ GeV/c, $|y_b|, |y_{\bar{b}}| \leq 1$, and $P_T(\bar{b}) \geq P_T^{min}(\bar{b})$. The uncertainty of the NLO QCD prediction (dashed line) comes from the variation of QCD parameters: $\mu = \mu_0/2 \sim 2\mu_0$, $\Lambda_5 = 100 \sim 300$ MeV, and $M_b = 4.5 \sim 5\ GeV/c^2$.

$P_T^{min}(b)$	$P_T^{min}(\bar{b})$	$\sigma_{b\bar{b}}(\mu b)$
6.5GeV/c	6.5GeV/c	$2.42 \pm 0.13(stat)^{+0.45}_{-0.42}(sys)$
6.5GeV/c	8.75GeV/c	$1.68 \pm 0.15(stat)^{+0.31}_{-0.29}(sys)$
6.5GeV/c	12.25GeV/c	$1.10 \pm 0.11(stat)^{+0.20}_{-0.19}(sys)$

Table 6.5: Total $b\bar{b}$ Cross Sections

order QCD is given by the MNR calculation of $b\bar{b}$ production [5]. In the calculation, we use the MRSD0 structure function [81], the renormalization scale $\mu = \mu_0 \equiv \sqrt{m_b^2 + (P_T(b)^2 + P_T(\bar{b})^2)/2}$, and $\Lambda = 140$ MeV with $m_b = 4.75 GeV/c^2$. Figure 6.4 shows the comparison between the measured $b\bar{b}$ cross sections and the MNR prediction. The uncertainty of the QCD prediction in the figure is obtained by varying the QCD parameters within the range of acceptable values [82]: $\mu = \mu_0/2 \sim 2\mu_0$, $\Lambda = 100 \sim 300$ MeV, and $m_b = 4.5 \sim 5 GeV/c^2$. The shape of the $b\bar{b}$ cross section agrees with the theoretical prediction although the values of the measured cross section are consistently higher.

Chapter 7

$\mu - \mu$ Correlations

We also investigate correlations between $b\bar{b}$ muons. The geometrical correlation is studied by examining the opening angle, $\delta\phi_{\mu\mu}$, distribution between $b\bar{b}$ muons in the transverse plane. The two-dimensional impact parameter fit is performed in each $\delta\phi$ bin to obtain the number of $b\bar{b}$ events. For a comparison with the theoretical prediction, the number of the $b\bar{b}$ events in each bin is divided by the integrated luminosity L and the normalized dimuon cross sections are listed in Table 6.6. The $P_T(\mu_{\bar{b}})$ distribution with $P_T(\mu_b) \geq 3$ GeV/c is also obtained using the impact parameter fitting method in each P_T bin for the study of the kinematic correlation. The results are shown in Table 7.1 and the errors include both statistical and systematic uncertainties of the fit and the luminosity [47]. For the predictions of $\mu - \mu$ correlations, we use a model based on the MNR calculation [5] which gives the exact parton cross section at order of $O(\alpha_s^3)$. The model consists of the MNR calculation and several mappings to simulate $b \rightarrow \mu$ decays. The mappings generate the momentum of a B hadron from the momentum of a bottom quark using the Peterson fragmentation function, and the muon momentum from the momentum of the hadron using the momentum distributions of muons in the rest frame of B hadrons. This model of the $b\bar{b} \rightarrow \mu\mu$ process is discussed in detail in Appendix B. We obtain the dimuon cross section with various constraints applying the model with weights including the branching ratio of $B \rightarrow \mu$ decay [49] and the efficiencies of the detector and data selection described in Chapter 6.3. Figures 7.1 and 7.2 show the results from data and the predictions of the model.

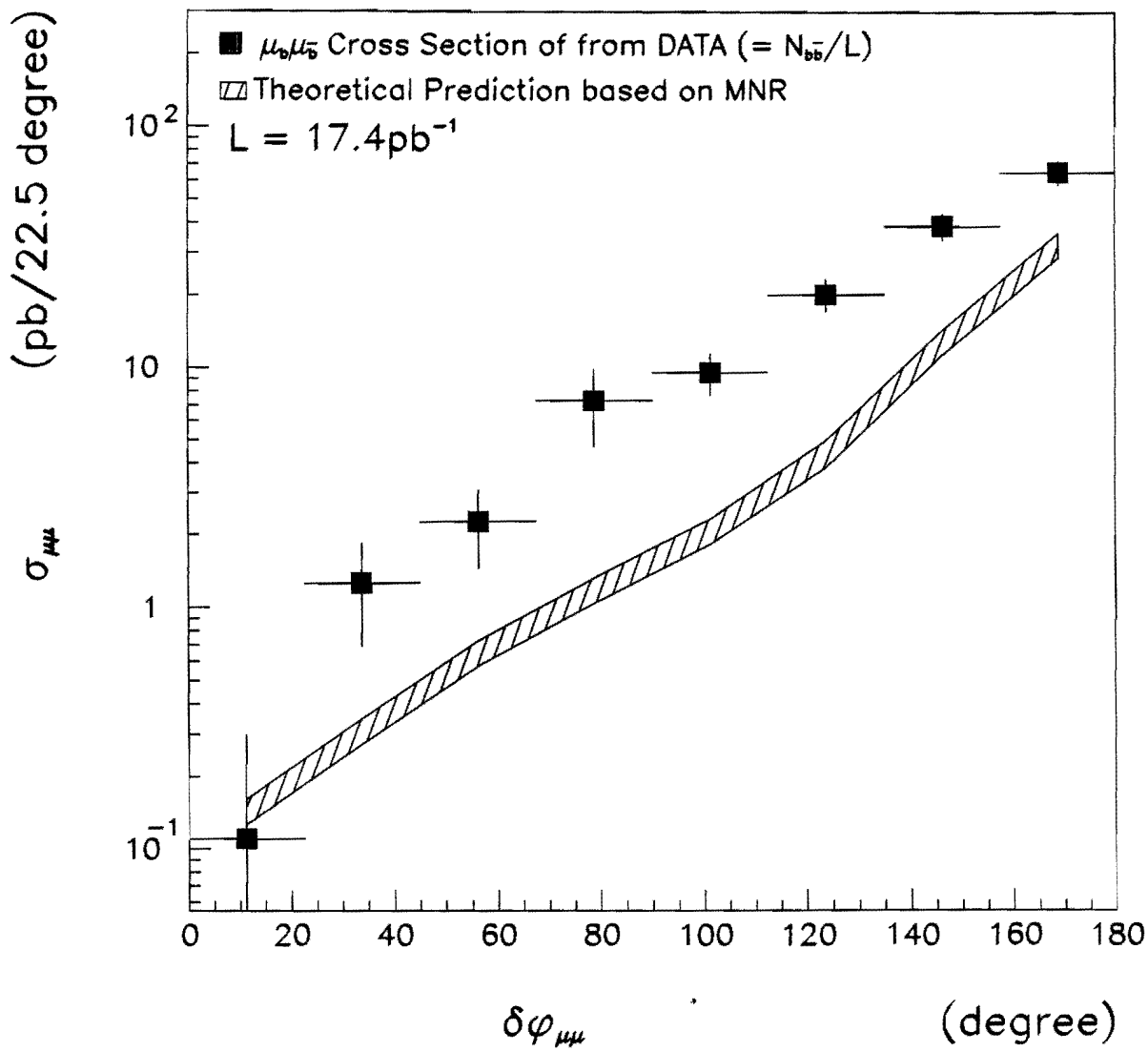

Figure 7.1: Opening angle distribution between $b\bar{b}$ muons. The data points have a common systematic uncertainty of the fit (+9.9% − 7.0%) and of the luminosity (±3.6%). The uncertainties of the theoretical prediction are from the efficiencies, branching ratio of $B \to \mu$, and the Peterson fragmentation parameter.

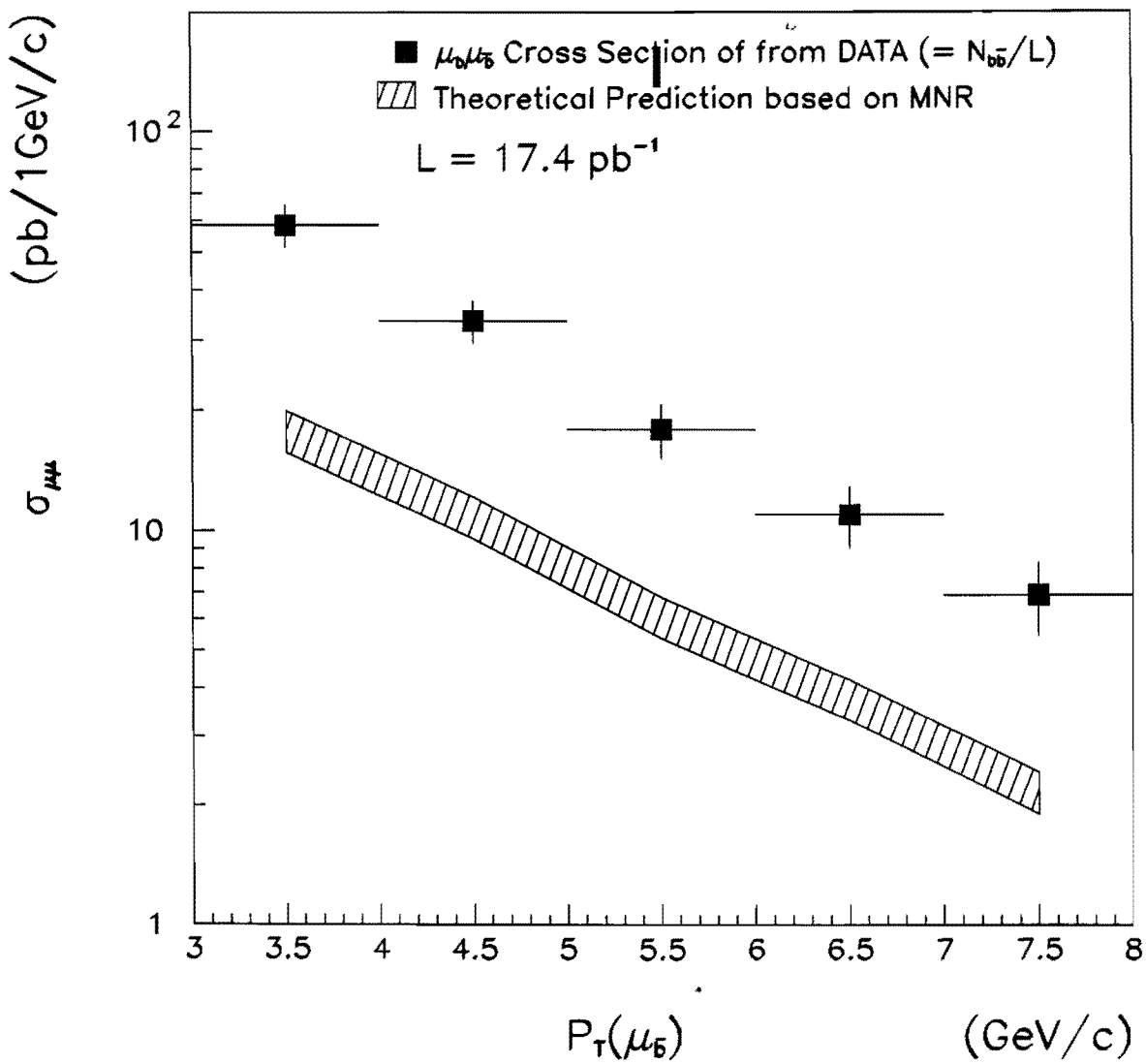

Figure 7.2: $P_T(\mu_{\bar{b}})$ for $P_T(\mu_b) \geq 3$ GeV/c. The data points have a common systematic uncertainty of the fit (+9.9% − 7.0%) and of the luminosity (±3.6%).The uncertainties of the theoretical prediction are from the efficiencies, branching ratio of $B \rightarrow \mu$, and the Peterson fragmentation parameter.

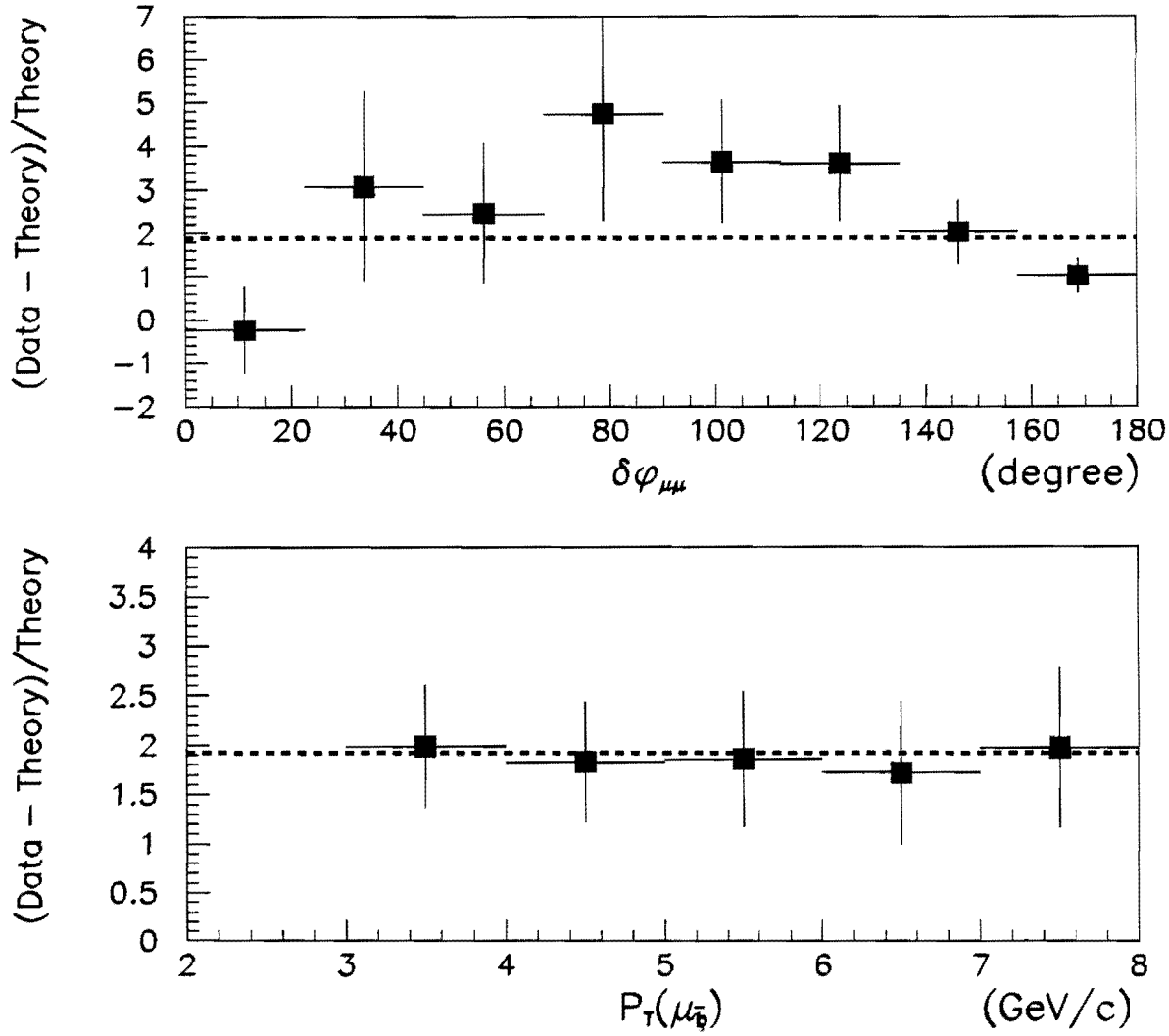

Figure 7.3: (Data-Theory)/Theory distributions of the opening angle between $b\bar{b}$ muons (top) and $P_T(\mu_{\bar{b}})$ (bottom). The uncertainties include the uncertainties of the data point and of the theoretical prediction. The systematic uncertainties are correlated. The dashed line represents the average value summed over all bins.

$\delta\phi_{\mu\mu}$	dimuon cross section (pb)
$0-\pi/8$	$0.11^{+0.19}_{-0.11}$
$\pi/8-\pi/4$	$1.26^{+0.57}_{-0.56}$
$\pi/4-3\pi/8$	$2.25^{+0.81}_{-0.80}$
$3\pi/8-\pi/2$	$6.72^{+2.60}_{-2.54}$
$\pi/2-5\pi/8$	$9.48^{+1.87}_{-1.77}$
$5\pi/8-3\pi/4$	$19.94^{+3.00}_{-2.65}$
$3\pi/4-7\pi/8$	$38.40^{+4.87}_{-4.06}$
$7\pi/8-\pi$	$64.19^{+7.48}_{-5.98}$
$P_T(\mu_{\bar{b}})(GeV/c)$	dimuon cross section (pb)
3 - 4	$58.39^{+7.07}_{-5.77}$
4 - 5	$33.64^{+4.09}_{-3.35}$
5 - 6	$18.03^{+2.79}_{-2.49}$
6 - 7	$11.01^{+1.92}_{-1.76}$
7 - 8	$6.92^{+1.46}_{-1.38}$

Table 7.1: Dimuon cross section as a function of $\delta\phi_{\mu\mu}$ and $P_T(\mu_{\bar{b}})$. The common systematic uncertainties (+9.9% —7.0%) of the fit and of the luminosity (±3.6%) are included in addition to statistical error.

The QCD calculation in the model uses the MRSD0 structure function [81], the renormalization scale $\mu = \mu_0$, and $\Lambda = 140$ MeV with $m_b = 4.75 GeV/c^2$. The uncertainty of the model predictions includes the systematic uncertainties of the weights and the uncertainty of the Peterson fragmentation ($\epsilon = 0.006 \pm 0.002$) [61]. Figure 7.3 shows that the shape of P_T distribution for $\mu_{\bar{b}}$ agrees well with the prediction although the normalization is significantly higher in the data as expected from the $b\bar{b}$ cross section measurement. The $\delta\phi$ distribution from the data also seems to agree with the model prediction within the errors in addition to a higher normalization as shown in Figure 7.3.

Chapter 8

Average $B^0\bar{B}^0$ Mixing Parameter

As discussed in Chapter 1.4, the time integrated mixing parameter $\bar{\chi}$ can be measured by studying charge correlations in dilepton data. In this analysis, $B^0\bar{B}^0$ mixing is studied by measuring the ratio, R, of the number of $b\bar{b}$ like-sign (LS) events and that of $b\bar{b}$ opposite sign (OS) events since $B^0\bar{B}^0$ mixing gives rise to the like-sign pairs.

8.1 Sequential Decays

In addition to the mixing, sequential decays of B hadrons ($b \to c \to \mu$) also contribute to R. The fraction of sequential decay muons, f_{seq}, is estimated using the Monte Carlo simulation described in Chapter 3.4, and can be written as:

$$f_{seq} = \frac{Br(b \to c \to \mu)}{Br(b \to \mu)} \frac{A_{seq}}{A_{dir}} \tag{8.1}$$

where A_{seq} and A_{dir} are the acceptances of sequential and direct muons respectively. From the Monte Carlo simulation based on the next-to-leading order QCD, the ratio of A_{seq} and A_{dir} is found to be 0.124 ± 0.007 where the error represents the uncertainty of the Peterson fragmentation parameter ϵ (0.006 ± 0.002) [61]. For the estimation of the branching ratio, $Br(b \to c \to \mu)$, the branching ratios of semileptonic decays of charm hadrons are set from the Particle Data Group such that $Br(D^0 \to \mu) = 0.089 \pm 0.014$ [65], $Br(D^\pm \to \mu) = 0.172 \pm 0.019$ [66], $Br(D_s^\pm \to \mu) = 0.076 \pm 0.008$ [67], and $Br(\Lambda_c^\pm \to \mu) = 0.045 \pm 0.017$ [68]. Assuming that B hadrons are produced by the

fragmentation with the production fractions, $B_d : B_u : B_s : \Lambda_b = 0.375 : 0.375 : 0.15 : 0.12$, we obtain the branching ratio, $Br(b \to c \to \mu) = 0.102 \pm 0.010$. Combined with the branching ratio, $Br(b \to c) = 0.103 \pm 0.005$ [49], f_{seq} is measured to be 0.123 ± 0.015.

8.2 Measurement

In $b\bar{b}$ dimuon events, there are several possible sources of LS and OS events as follows:

1. If both B hadrons mix, which occurs with a probability of $\bar{\chi}^2$, one direct and one sequential decay muon will have like-sign charges and two direct or two sequential decay muons will have opposite-sign charges.

2. If neither of B hadron mixes, which occurs with a probability of $(1-\bar{\chi})^2$, one direct and one sequential decay muon will have like-sign charges and two direct or two sequential decay muons will have opposite-sign charges.

3. If only one B hadron mixes, which occurs with a probability of $2\bar{\chi}(1-\bar{\chi})$, one direct and one sequential decay muon will have opposite-sign charges and two direct or two sequential decay muons will have like-sign charges.

Therefore the ratio, R, of the number of like-sign events, N_{ls}, to that of opposite-sign events, N_{os}, is related to the time integrated mixing parameter $\bar{\chi}$ in the following way.

$$R = \frac{N_{ls}}{N_{os}} = \frac{2f_{seq}(\bar{\chi}^2 + (1-\bar{\chi})^2) + 2\bar{\chi}(1-\bar{\chi})(1+f_{seq}^2)}{(\bar{\chi}^2 + (1-\bar{\chi})^2)(1+f_{seq}^2) + 4f_{seq}\bar{\chi}(1-\bar{\chi})} \tag{8.2}$$

where f_{seq} is the fraction of sequential B muons.

The two dimensional impact parameter fitting method is used to determine the number of $b\bar{b}$ events in the like-sign and opposite-sign data sample. The log likelihood functions and the fit results in LS and OS dimuon events are described in Chapter 4.3 where we obtain 838 ± 53 like-sign (LS) and 1669 ± 88 opposite-sign

(OS) events. Figure 8.1 shows the projections of the two dimensional impact parameter distributions onto one axis for a comparison of the data and the fitted distributions. In opposite-sign (OS) events, the inclusion of $c\bar{c}$ events results in a $\pm 4.7\%$ uncertainty in the fit fraction for $b\bar{b}$ events as described in Chapter 4.4. Other sources of systematic uncertainties cancel out in the ratio R which is measured to be $0.502 \pm 0.041(stat) \pm 0.024(sys)$. In the absence of mixing, R would be 0.242 ± 0.029, which is inconsistent with the measured value.

Using the observed value of R and the value of f_{seq} from the Monte Carlo, the $B^0\bar{B}^0$ mixing parameter $\bar{\chi}$ is measured to be $0.131 \pm 0.020(stat) \pm 0.016(sys)$ consistent with previous measurements [83, 84, 85, 86, 87] as shown in Figure 8.2. The sources of the main systematics are listed in Table 8.1. The mixing parameter, $\bar{\chi}$ is

Source	Systematics
Charm fraction	$\pm 9.2\%$
$\mathrm{Br}(b \to c \to \mu)/\mathrm{Br}(b \to \mu)$	$\pm 7.6\%$
Fragmentation	$\pm 3.7\%$
Total	$\pm 12.5\%$

Table 8.1: Systematics of the measurement of $\bar{\chi}$

a value averaged over all B hadrons including B_d and B_s mesons. In the expression (1.9) for $\bar{\chi}$, there are two components represented by $f_d\chi_d$ and $f_s\chi_s$ where f_d and f_s are the fractions of B_d and B_s mesons respectively. Assuming that $f_s = 0.15$ and $f_d = 0.375$, we plot the region constrained by the result on the $\chi_d - \chi_s$ plane in Figure 8.3. The CLEO and ARGUS combined result for χ_d [88] and the ALEPH result for χ_s [28] are also plotted for a comparison.

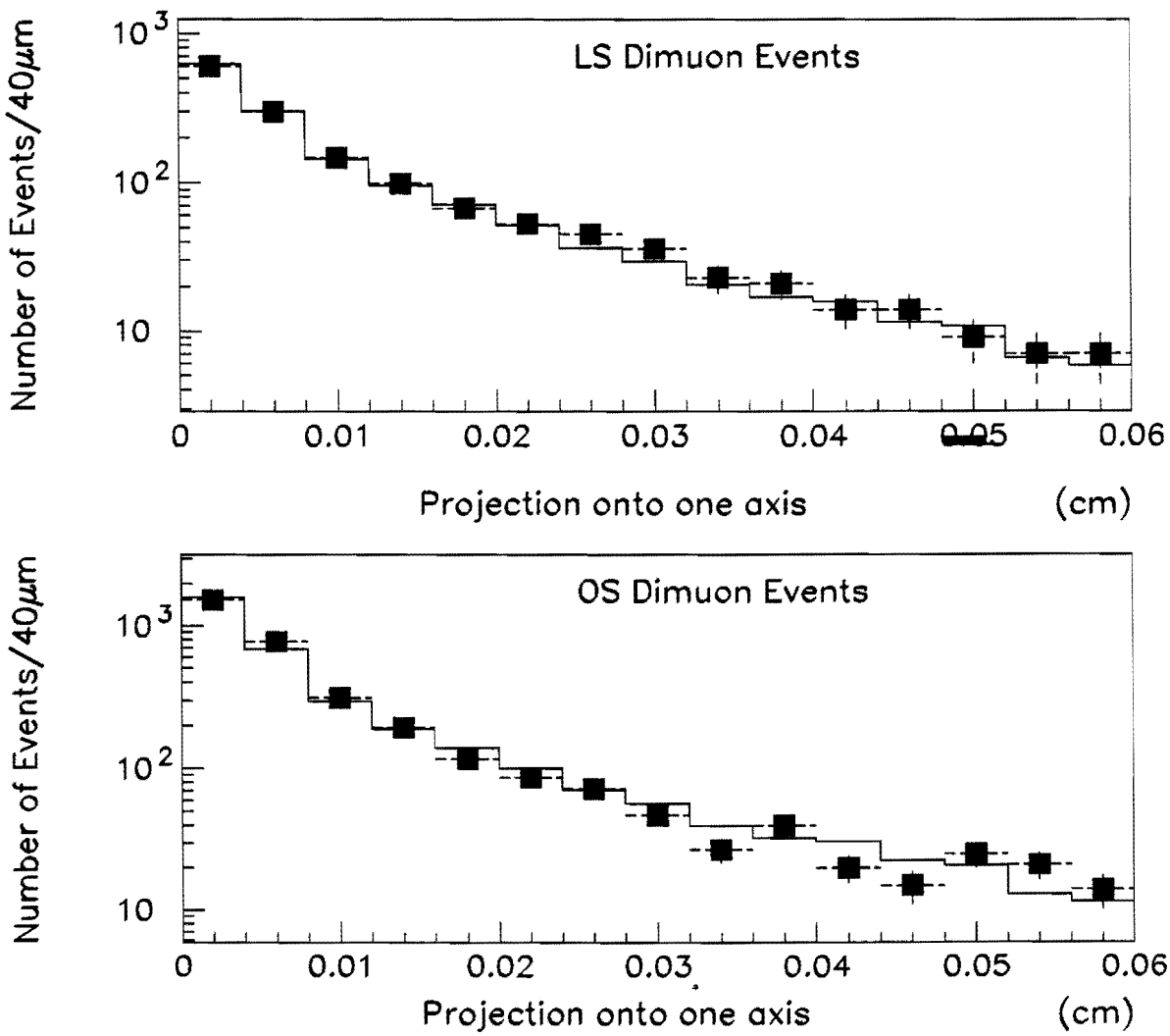

Figure 8.1: Projections of the two dimensional impact parameter distributions in LS and OS events. The solid line represents the fitted distribution and the filled boxes with an error bar represent the data distribution.

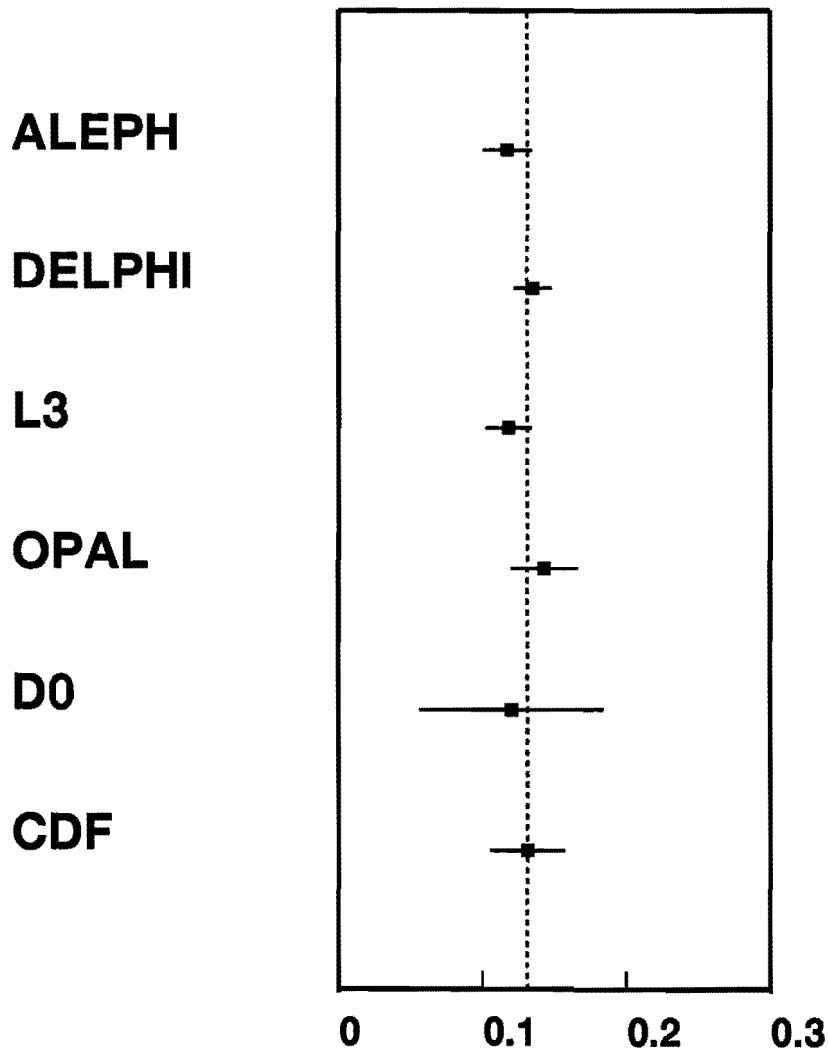

Figure 8.2: Comparison with measurements of $\bar{\chi}$ from other experiments. The dotted line represents the world average value of $\bar{\chi}$ (0.133) from Particle Data Group.

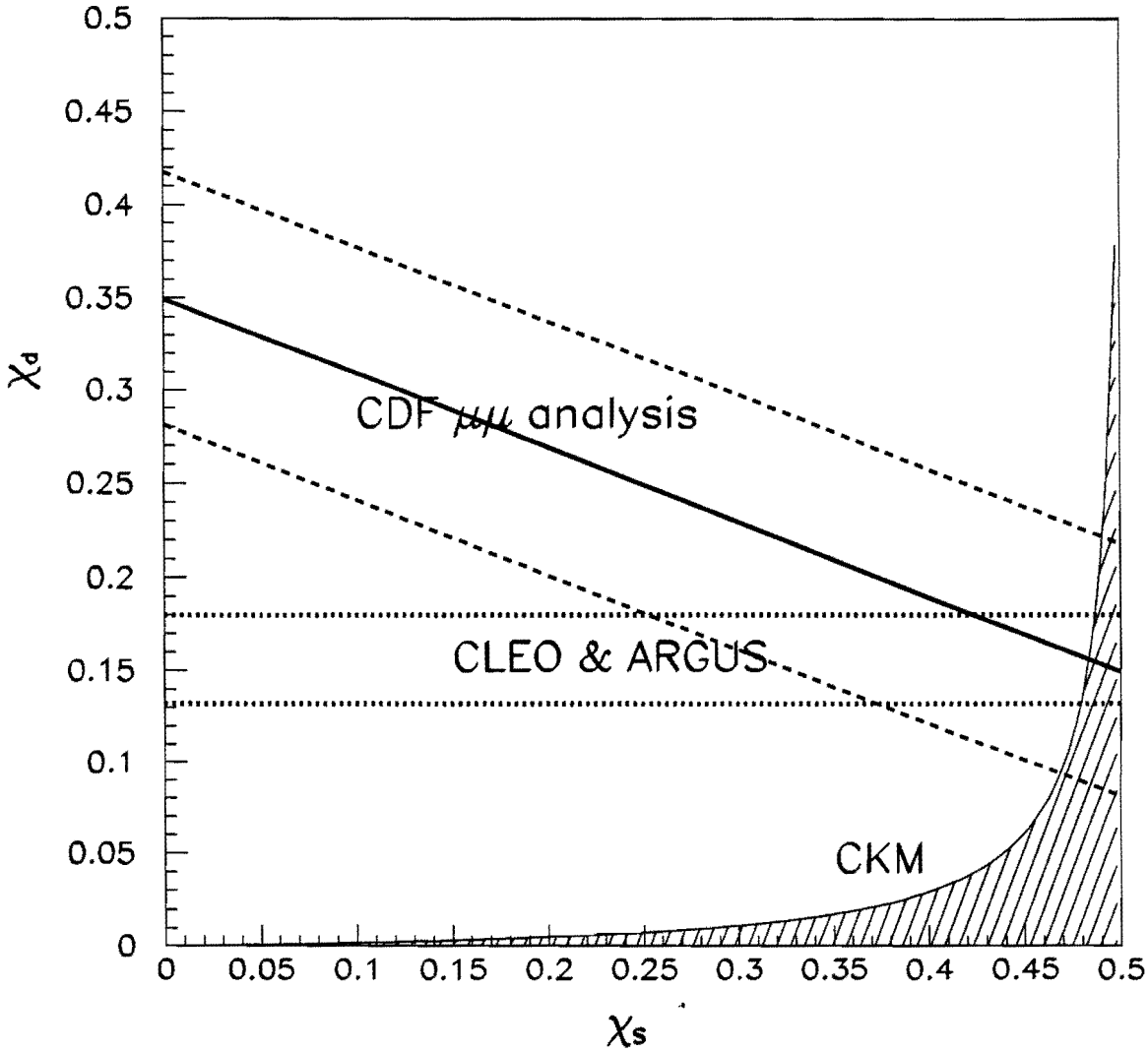

Figure 8.3: χ_d vs χ_s. The bands represents $\pm 1\sigma$ uncertainty of the measurement assuming that f_d and f_s are 0.375 and 0.15 respectively. The χ_d range represents the CLEO and ARGUS combined result (0.156 ± 0.024). The hatched region is allowed by the Standard Model.

Chapter 9

CP Violating Asymmetry

CP violation in the B system gives rise to the different mixing probabilities for B^0 and $\bar{B}^0$ meson [29]. In the dimuon events from $B\bar{B}$ decay, the effect of CP violation in $B^0\bar{B}^0$ mixing would appear as an asymmetry between $\mu^+\mu^+$ and $\mu^-\mu^-$ events where one of the neutral B mesons is mixed. By measuring the dimuon asymmetry we can constrain the real part of the CP violating parameters ϵ_d and ϵ_s [29] where the subscript of ϵ represents the flavor of the corresponding neutral B mesons.

9.1 Principle

From (1.30) in Chapter 1.5, the charge asymmetry in dimuon data from CP asymmetry, A_{cp}, is written as:

$$A_{cp} = \frac{P(l^+l^+) - P(l^-l^-)}{P(l^+l^+) + P(l^-l^-)} = \frac{8f_d\chi_d(1-\bar{\chi})}{D}\frac{Re\epsilon_d}{1+|\epsilon_d|^2} + \frac{8f_s\chi_s(1-\bar{\chi})}{D}\frac{Re\epsilon_s}{1+|\epsilon_s|^2} \quad (9.1)$$

$$D = 2\bar{\chi}(1-\bar{\chi}) \quad (9.2)$$

In reality, bottom muons arise from sequential decays as well as from direct decays as described in Chapter 8.2. If both B mesons mix or neither mixes, events with one direct decay muon and one sequential decay muon are of like-sign. From Equation (1.20)-(1.23), we infer that the effects of CP asymmetry cancel out in these LS events. Consequently, sequential decay muons affect the normalization of the expression (9.2)

only. Including sequential decay muons, the normalization factor D is rewritten as follows:

$$D = 2\bar{\chi}(1-\bar{\chi}) + 2f_{seq}\{\bar{\chi}^2 + (1-\bar{\chi})^2\} \tag{9.3}$$

where f_{seq} is the fraction of sequential decay muons (0.123 ± 0.015, see Chapter 8.1 for details).

9.2 Charge Asymmetry in Dimuon Data

The method used to estimate the number of $b\bar{b}$ dimuons in $\mu^+\mu^+$ and $\mu^-\mu^-$ events is a two dimensional SVX impact parameter fit as described in Chapter 4. Using the log likelihood function for LS events defined in Chapter 4.3, one performs the fit and obtains 428 ± 37 $b\bar{b}$ events for $\mu^+\mu^+$ and 410 ± 37 $b\bar{b}$ events for $\mu^-\mu^-$. Figure 9.1 graphically shows the results of the fit. From the fit results, the charge asymmetry in the dimuon sample, A_{fit}, is calculated.

$$\frac{N_{b\bar{b}}^{++} - N_{b\bar{b}}^{--}}{N_{b\bar{b}}^{++} + N_{b\bar{b}}^{--}} \equiv A_{fit} = (2.15 \pm 6.30(stat)) \times 10^{-2}$$

9.3 Systematic Uncertainty in Charge Asymmetry

In order to extract the dimuon charge asymmetry due to CP violation (A_{cp}) from the the value of A_{fit}, we must take into account any instrumental or reconstruction bias in the measured asymmetry in the number of $\mu^+\mu^+$ and $\mu^-\mu^-$ events.

Focusing on the ratio of $b\bar{b}$ events, many systematic uncertainties discussed in the $b\bar{b}$ correlation analysis such as the B lifetime, the resolution difference between Monte Carlo and data, etc. cancel out. The main sources of the systematic uncertainty in the charge asymmetry are a charge bias of the CDF tracking and the trigger system.

The charge bias of the tracking can be obtained from minimum bias data. By applying the same cuts on the data (except muon cuts), 3157 positively charged tracks and 3135 negatively charged tracks are found in the data. From these numbers, the charge asymmetry of tracks ($(N_+ - N_-)/(N_+ + N_-)$) is estimated to be $(0.35 \pm 1.27) \times 10^{-2}$ where the error is from statistics in the minimum bias data. The dimuon

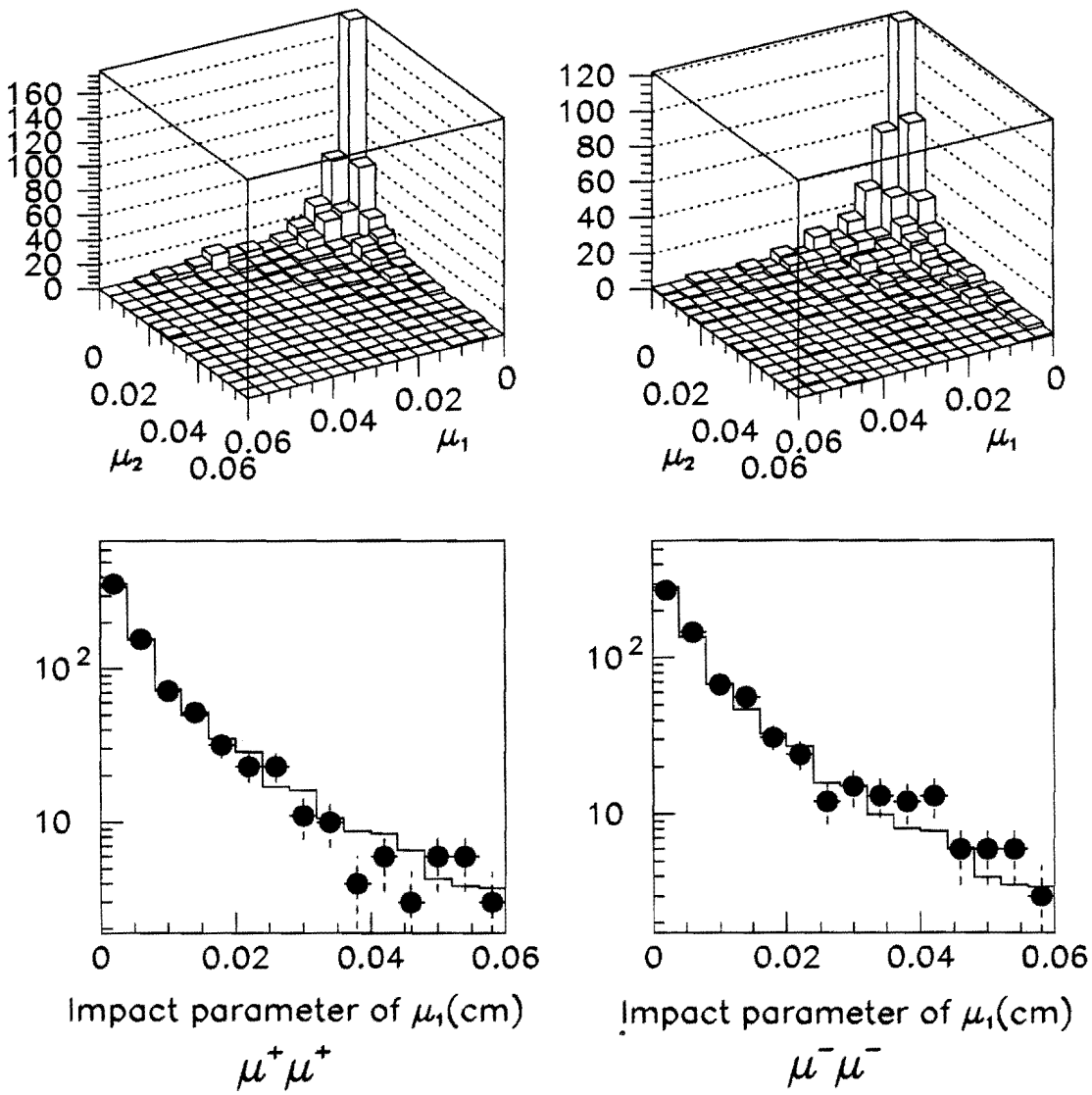

Figure 9.1: Comparison between the data and fitted distributions in LS events. The upper two histograms are two dimensional impact parameter distributions in $\mu^+\mu^+$ and $\mu^-\mu^-$ data. In the lower histograms, the solid line represents the projection onto μ_1 axis of the two dimensional distribution which is a sum of 3 components in the fit and the filled circle with error bar represents the projection of the upper distribution.

charge asymmetry due to the tracking is 2 times the single track charge asymmetry (there are two muon tracks in an event) and is found to be $(0.70 \pm 2.54) \times 10^{-2}$.

The dimuon trigger efficiency can be measured using J/ψ muons as discussed in Chapter 6.3. Using the side-band subtracted sample, the trigger efficiencies for μ^+ and μ^- are separately parameterized as a function of P_T at each level. A least squares fit is used to find the parameterization. Figures 9.2 and 9.3 show the parameterized efficiency curves at level 1 and level 2 respectively [48]. In order to extract the charge asymmetry in dimuon data due to the trigger, the P_T distribution of bottom muons from the Monte Carlo simulation (ISAJET+CDFSIM) [59, 63] is convoluted with parameterized trigger curves separately for each charge. By comparing the P_T distributions for μ^+ and μ^-, we obtain $(-0.90 \pm 2.07) \times 10^{-2}$ for the asymmetry of the dimuon trigger where the error results from the uncertainty in the parameterization.

To summarize, the total dimuon asymmetry due to instrumental and offline bias is estimated to be $(-0.24 \pm 3.28(sys)) \times 10^{-2}$.

9.4 Result

The charge asymmetry due to CP violation A_{cp} is estimated by subtracting the instrumental and offline bias from the measured asymmetry.

$$A_{cp} = (2.39 \pm 6.30(stat) \pm 3.28(sys)) \times 10^{-2}$$

From Equation (9.1) for A_{cp} and the world average value of $\bar{\chi}$ (0.133 ± 0.011) from the Particle Data Group [89], we obtain one constraint for four quantities - $Re\epsilon_d$, $Im\epsilon_d$, $Re\epsilon_s$, and $Im\epsilon_s$ as follows:

$$f_d\chi_d\frac{Re\epsilon_d}{1+|\epsilon_d|^2} + f_s\chi_s\frac{Re\epsilon_s}{1+|\epsilon_s|^2} = (1.45 \pm 3.81(stat) \pm 1.99(sys)) \times 10^{-3}$$

Using the values of f_d, f_s, χ_d, and χ_s from the Particle Data Group [89], one can plot the region constrained by the above result in $\frac{Re\epsilon_d}{1+|\epsilon_d|^2}$ - $\frac{Re\epsilon_s}{1+|\epsilon_s|^2}$ space in Figure 9.4. The result on $\frac{Re\epsilon_d}{1+|\epsilon_d|^2}$ from the CLEO experiment [26] is also plotted in the same figure. Figure 9.4 shows that the result of this analysis is sensitive to a few$\times 10^{-2}$ at 1σ level for $Re\epsilon$.

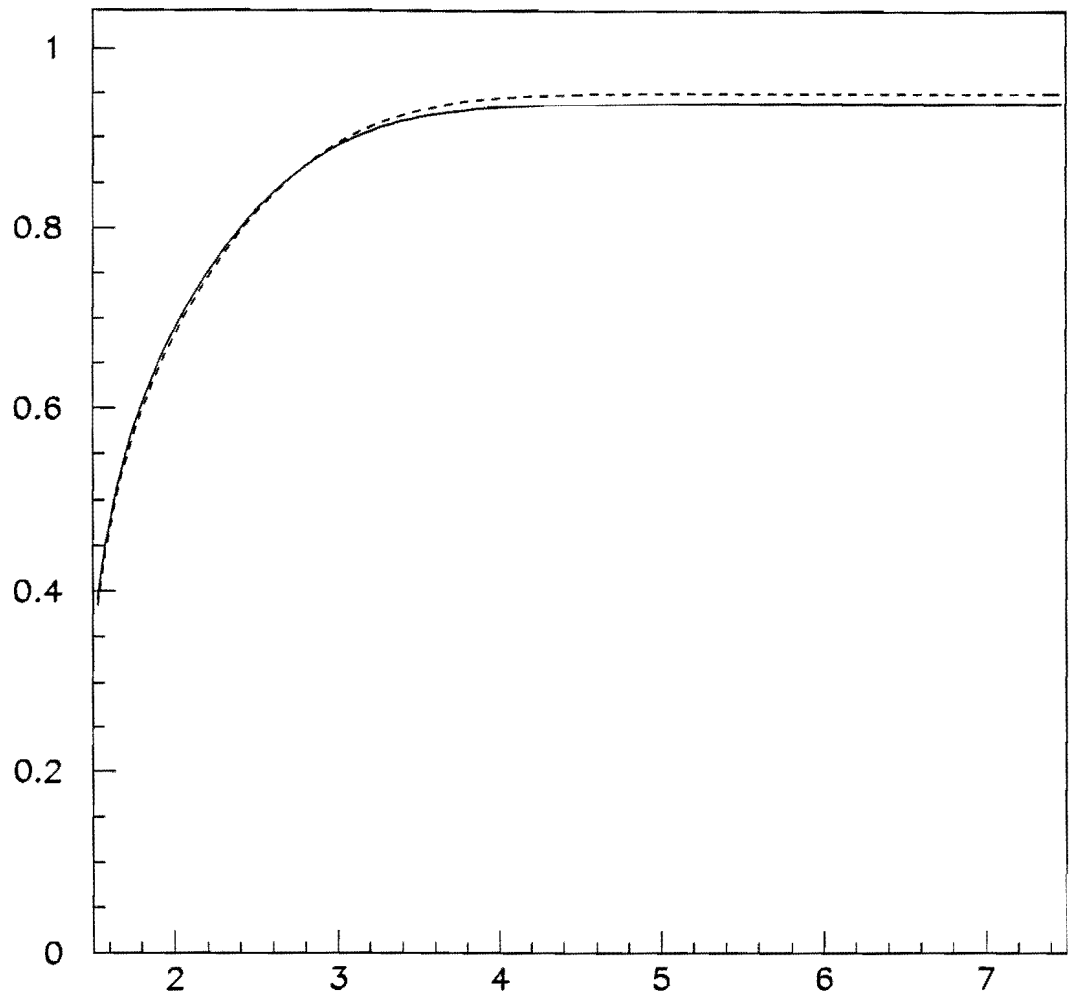

Figure 9.2: Level 1 trigger efficiency as a function of P_t. The solid line represents the parameterized efficiency of μ^+ and the dashed line represents the parameterized efficiency of μ^-.

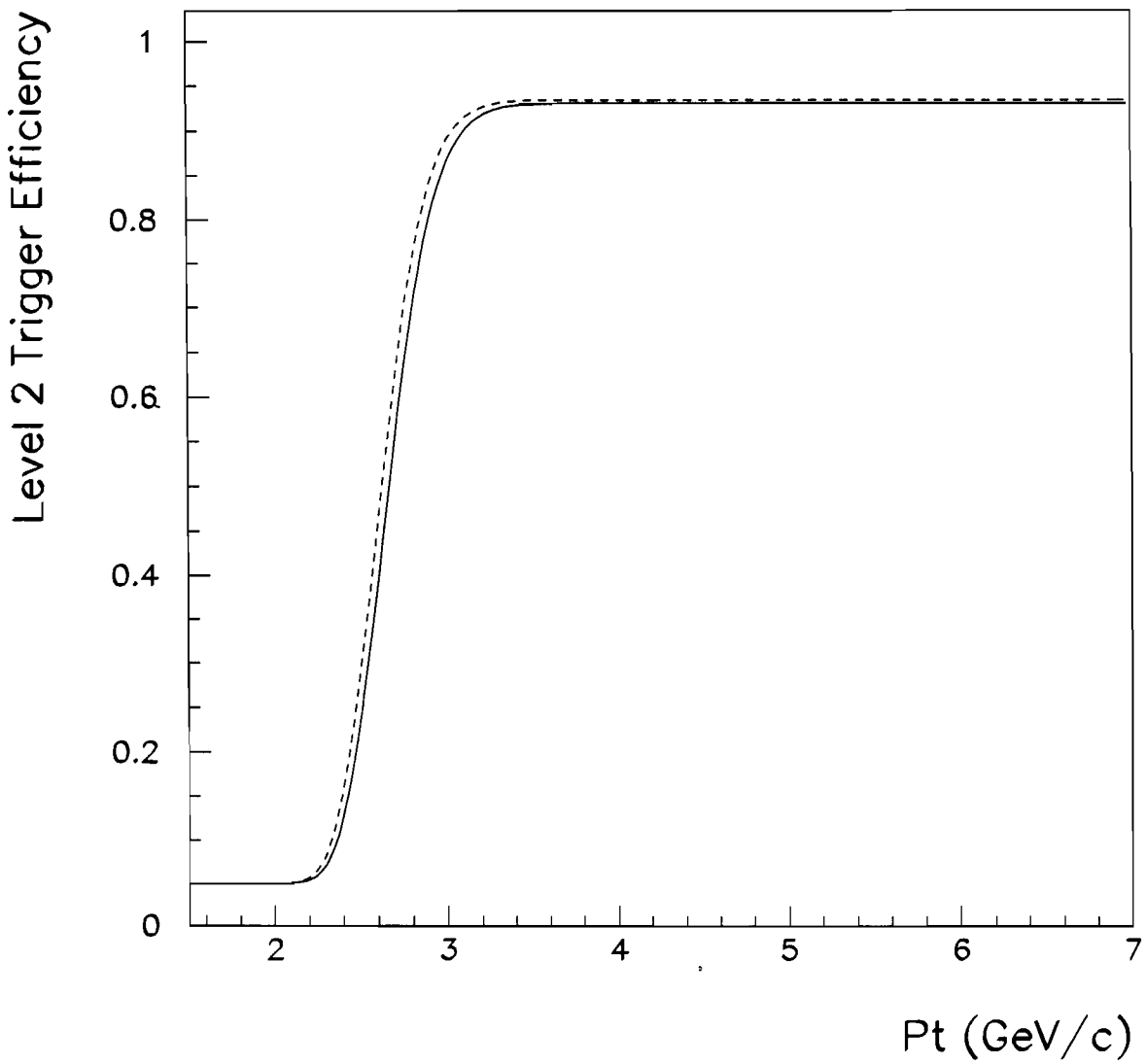

Figure 9.3: Level 2 trigger efficiency as a function of P_t. The solid line represents the parameterized efficiency of μ^+ and the dashed line represents the parameterized efficiency of μ^-.

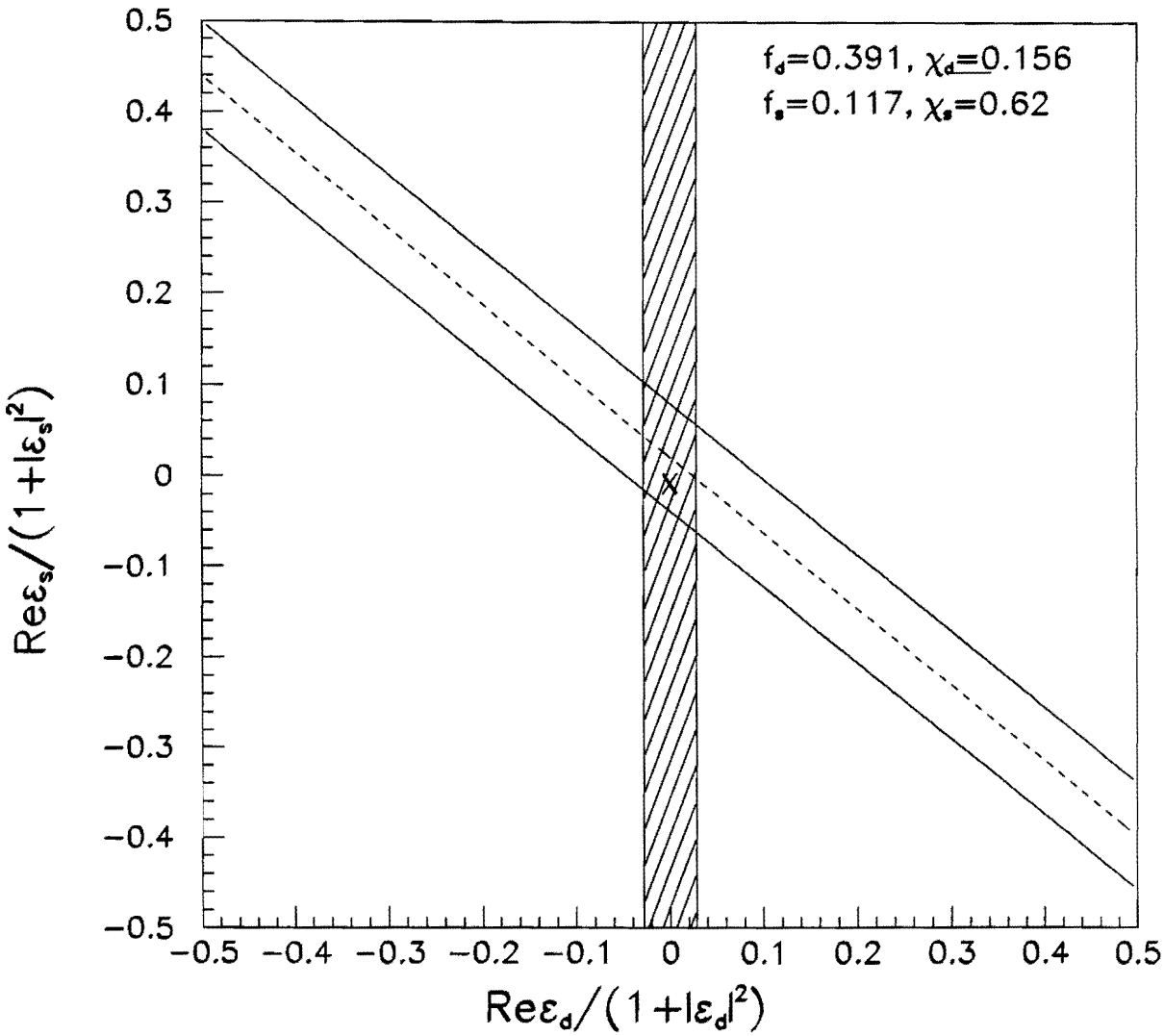

Figure 9.4: $\frac{Re\epsilon_d}{1+|\epsilon_d|^2}$ vs $\frac{Re\epsilon_s}{1+|\epsilon_s|^2}$. The solid lines represent the $\pm 1\sigma$ uncertainties and the dashed line represents the measured value of the asymmetry. The hatched region is from the CLEO measurement in $B_d^0\bar{B}_d^0$ sample. The marker X represents the prediction of the standard model.

Chapter 10

Conclusion

We have presented results on $b\bar{b}$ production correlations, the average $B^0\bar{B}^0$ mixing, and the CP asymmetry parameter ϵ_B using dimuon events from the semileptonic decays of a $b\bar{b}$ pair.

For the studies of $b\bar{b}$ correlations, we have measured the $b\bar{b}$ cross section as a function of $P_T(\bar{b})$, the azimuthal opening angle distribution between the two muons from $b\bar{b}$ decays, and the P_T distribution of a bottom muon with a P_T constraint on the other bottom muon. These results show consistently higher normalization than the predictions of the next-to-leading order (NLO) QCD theory which uses the MRSD0 proton structure function, the renormalization scale $\mu = \mu_0$, $\Lambda = 140$ MeV, and $m_b = 4.75 GeV/c^2$. Accounting for the uncertainties of the above QCD parameters ($\mu = \mu_0/2 \sim \mu_0$, $\Lambda = 100 \sim 300$MeV, and $m_b = 4.5 \sim 5.0 GeV/c^2$), an upper and a lower bound of the QCD prediction have been compared to the results on the $b\bar{b}$ cross section. The results are about 30% higher than the upper bound of the theory as shown in Figure 6.4. However, taking into account a $20 \sim 30\%$ uncertainty of the measurements, the data show consistency with the NLO QCD prediction. A qualitative picture of $b\bar{b}$ production has been obtained by the studies of $\mu - \mu$ correlations. The shape of the P_T distribution of bottom muons agree well with the theory (Figures 7.2 and 7.3). The shape of the opening angle distribution between the two bottom muons is also found to be consistent with the theory within the uncertainties (Figures 7.1 and 7.3). The conclusion we can derive from the above measurements is that the

comparison of data and NLO predictions for $b\bar{b}$ production favors small values of the b quark mass and large values of Λ and the functional shapes of the $\mu\mu$ cross section agree with the theoretical prediction.

Using muon charge correlations, we have also studied various electroweak phenomena such as $B^0\bar{B}^0$ mixing and CP violation. Comparing like-sign and opposite-sign dimuon events, the average $B^0\bar{B}^0$ mixing parameter, $\bar{\chi}$, has been measured to be $0.131 \pm 0.020(stat) \pm 0.016(sys)$ which is consistent with the other measurements [83, 84, 85, 86, 87]. The measurement of an asymmetry between $\mu^-\mu^-$ and $\mu^+\mu^+$ events has provided a constraint on the real part of the CP asymmetry parameter ϵ_B. The result on $Re(\epsilon_B)$ (a few$\times 10^{-2}$) is not sensitive to detect CP violation predicted by the Standard Model ($\sim 10^{-3}$). We need at least hundred times more data in order to begin probing of of CP violation arising from the Standard Model in this way. Meanwhile the present results serve to place constraints on the amount of CP violation which may be induced from physics beyond the Standard Model.

Appendix A

Solutions of Dimuon Equations

From section 5.1, we have 3 equations for $\mu^-\mu^-$ events.

$$N_{0cmp} = a_1 M + a_2 F_1 + a_3 F_2$$

$$N_{1cmp} = b_1 M + b_2 F_1 + b_3 F_2$$

$$N_{2cmp} = c_1 M + c_2 F_1 + c_3 F_2$$

where

$a_1 = (1-\epsilon_\mu)^2$, $a_2 = (1-\epsilon_\mu)(1-\epsilon_f)$, $a_3 = (1-\epsilon_f)^2$

$b_1 = 2\epsilon_\mu(1-\epsilon_\mu)$, $b_2 = \epsilon_\mu(1-\epsilon_f) + \epsilon_f(1-\epsilon_\mu)$, $b_3 = 2\epsilon_f(1-\epsilon_f)$

$c_1 = \epsilon_\mu^2$, $c_2 = \epsilon_\mu\epsilon_f$, $c_3 = \epsilon_f$

The above three equations are linear and solved for M, F_1, and F_2.

$$M(\epsilon_\mu, \epsilon_f) = \frac{(N_{1cmp} - b_2 N_{tot})(c_3 - c_2) - (N_{2cmp} - c_2 N_{tot})(b_3 - b_2)}{(b_1 - b_2)(c_3 - c_2) - (c_1 - c_2)(b_3 - b_2)}$$

$$F_1(\epsilon_\mu, \epsilon_f) = \frac{(N_{1cmp} - b_1 N_{tot})(c_3 - c_1) - (N_{2cmp} - c_1 N_{tot})(b_3 - b_1)}{(b_2 - b_1)(c_3 - c_1) - (c_2 - c_1)(b_3 - b_1)}$$

$$F_2(\epsilon_\mu, \epsilon_f) = \frac{(N_{1cmp} - b_1 N_{tot})(c_2 - c_1) - (N_{2cmp} - c_1 N_{tot})(b_2 - b_1)}{(b_3 - b_1)(c_2 - c_1) - (c_3 - c_1)(b_2 - b_1)}$$

where $N_{tot} = N_{0cmp} + N_{1cmp} + N_{2cmp}$. In section 5.1, we have 592 events for N_{0cmp}, 1430 events for N_{1cmp}, 1401 events for N_{2cmp}, 0.94 for ϵ_μ. Given these numbers, Figure 5.1 plots M, F_1, and F_2 as a function of ϵ_f.

Appendix B

$\mu - \mu$ Correlations from the MNR Calculation

B.1 Introduction

The Monte Carlo method of Mangano, Nason, and Ridolfi calculates the fully exclusive parton cross section for heavy quark production at order of $O(\alpha_s^3)$. For the integration over a certain region of phase space which includes divergences, the Monte Carlo generates an event and the corresponding counter-events with appropriate weights. The problem with this method is that, depending on the kinematics, some counter-events may have negative weight and the parton cross section for a certain range of parton variable may become negative. In principle, we can solve this problem by generating an infinite number of events and counter-events and cancelling out the negative contributions from counter-events by the positive weights of real events. In reality, we generate very large statistics (typically 10^8) and create a histogram for a parton variable and rebin the histogram so that any fluctuation between events and counter-events can be summed and smoothed out. In this way, the cross section for heavy quark-antiquark production for various kinematic constraints can be calculated from the MNR Monte Carlo.

In order to obtain the prediction of $\mu - \mu$ correlations from the MNR calculation,

the fragmentation of bottom quarks and the decay of bottom hadrons needs to be implemented in an appropriate way. The direct inclusion of the Peterson fragmentation and $B \rightarrow \mu$ decay (for example, via the CLEO decay package) within the MNR Monte Carlo greatly enhances fluctuations between events and the corresponding counter-events. Event and counter-events are no longer close to each other in phase space of muon variables so that the rebinning method can not be used to obtain smooth distributions of muon variables.

We describe a model to generate theoretical predictions of $\mu - \mu$ correlation directly from the MNR code. The idea of this model is that the fragmentation of b quark and B decays are replaced by a set of mappings and the same mapping generated by the same random seeds is used for events and counter-events. In this way, we can minimize the jitter between events and counter-events even at the muon level and smooth distributions of muon variables can be obtained by rebinning.

B.2 Mapping

In the model, the mapping means the parameterization of the fragmentation and B decay. We find independent parameters with which the bottom meson momentum and muon momentum can be calculated. These parameters are generated using a random number generator with weights. We obtain weight distributions of parameters from the Peterson fragmentation function and the CLEO Monte Carlo package.

By using the same parameters (or the same random seeds), we expect the jitter between events and counter-events in muon phase space to be minimized.

- Fragmentation ($b \rightarrow B$)

We use the Peterson fragmentation function to get the fragmentation mapping. From the function, we select three parameters which are generated by random seeds.

(1) Z

The energy of meson from the fragmentation is calculated by the parameter Z. If

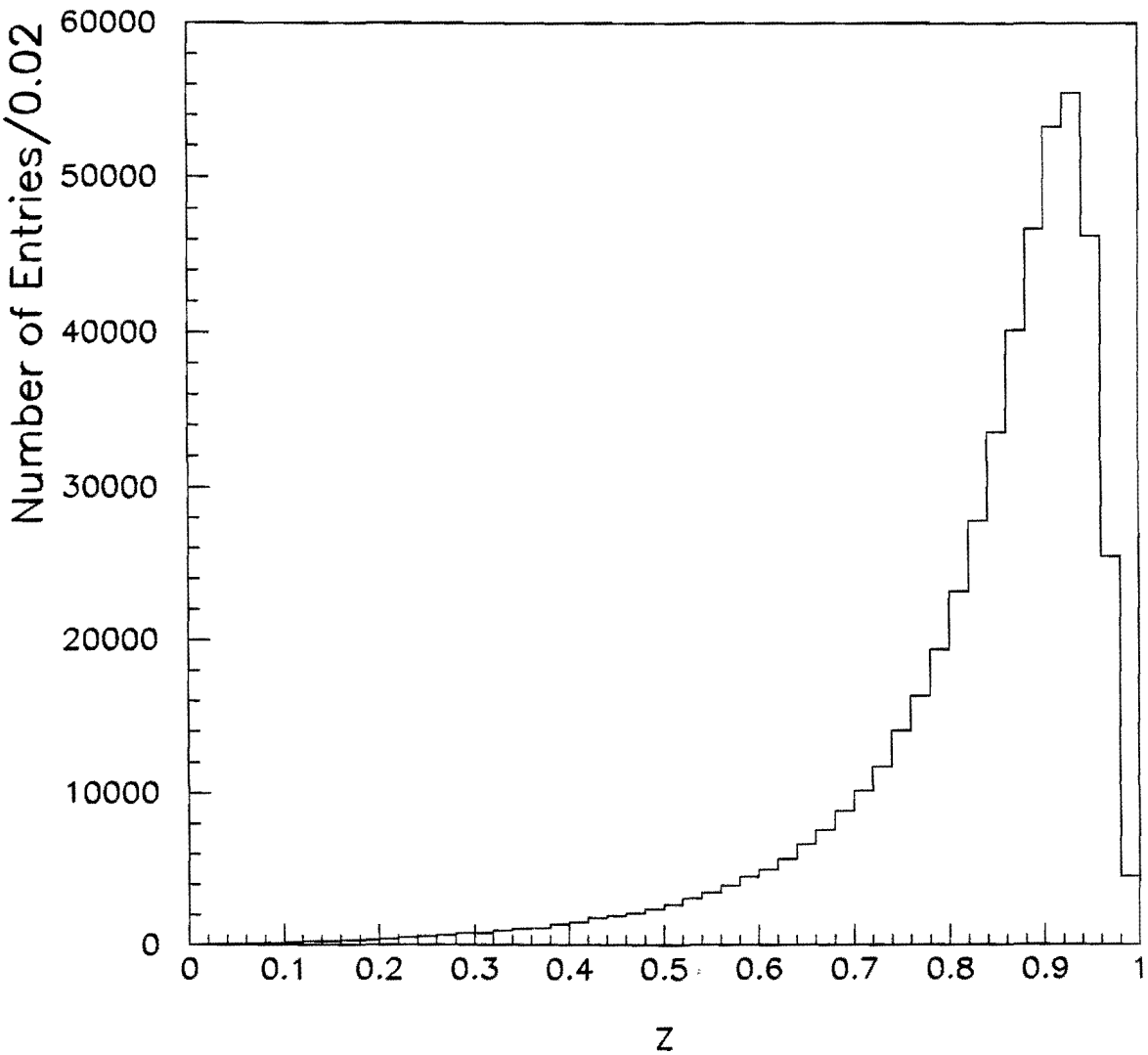

Figure B.1: The distribution of Z variable of the Peterson fragmentation. The distribution is plotted for $\epsilon = 0.006$.

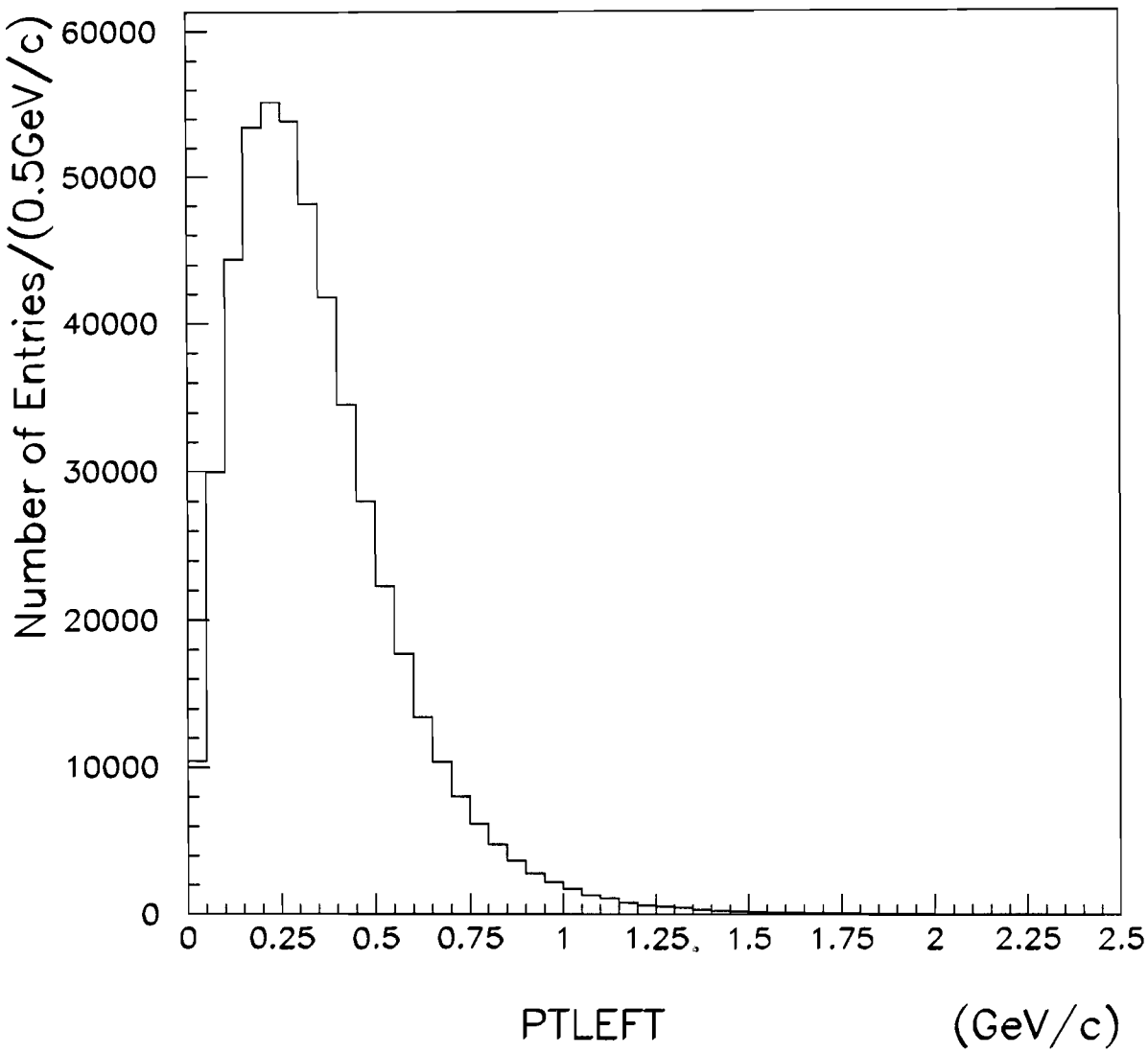

Figure B.2: Momentum of B hadron perpendicular to the quark direction.

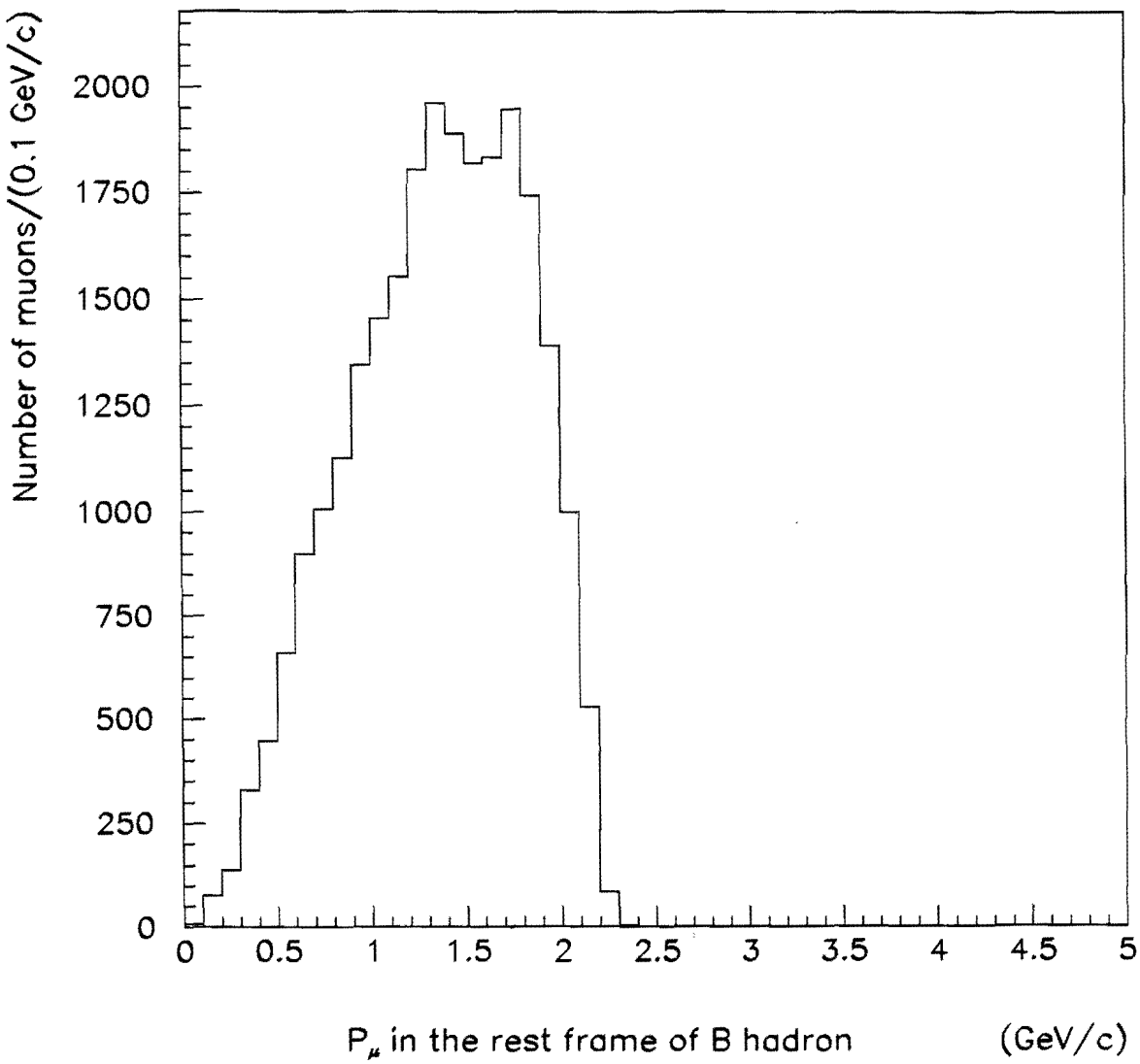

Figure B.3: Total momentum of muon in the rest frame of B hadron.

the energy of meson is greater than that of b quark, another random seed is tried to create the same Z for events and counter-events. The distribution of Z is shown in Figure B.1.

(2) Meson momentum perpendicular to the quark momentum
The parameter PTLEFT is the magnitude of meson momentum perpendicular to the b quark momentum. The distribution of PTLEFT is shown in Figure B.2.

(3) Direction of meson momentum vector perpendicular to the b quark direction
In the transverse plane perpendicular to the quark direction, the meson direction is isotropic and uniformly distributed in azimuthal angle.

We use the same random seeds for the above parameters to apply the same fragmentation mapping to events and counter-events. The P_T distribution of B hadrons from the mapping are plotted in Figure B.4.

• B Decay ($B \rightarrow \mu$)

The mapping for B decays to muons can be found by studying muon momentum distribution in the rest frame of the B hadron. In the rest frame of the hadron, there are only three parameters to be determined for generation of muon momentum - $|P_\mu|$, ϕ and $\cos(\theta)$. They are not correlated to each other and generated by separate random seeds. From the CLEO Monte Carlo program, we plot the distributions of $|P_\mu|$ in the rest frame of B hadrons in Figure B.3. The distributions of ϕ and $\cos(\theta)$ are uniform as expected from the isotropy of decay process.

Within the MNR code, we apply the same mapping for B decay generated by the same random seeds and the Lorentz transformation from the rest frame of B hadron to the lab frame to events and counter-events. We also keep track of muon cut variations by applying the cuts to events and counter-events at the same time. The P_T distributions of muons from the fragmentation and $B \rightarrow \mu$ mapping are shown in Figure B.5.

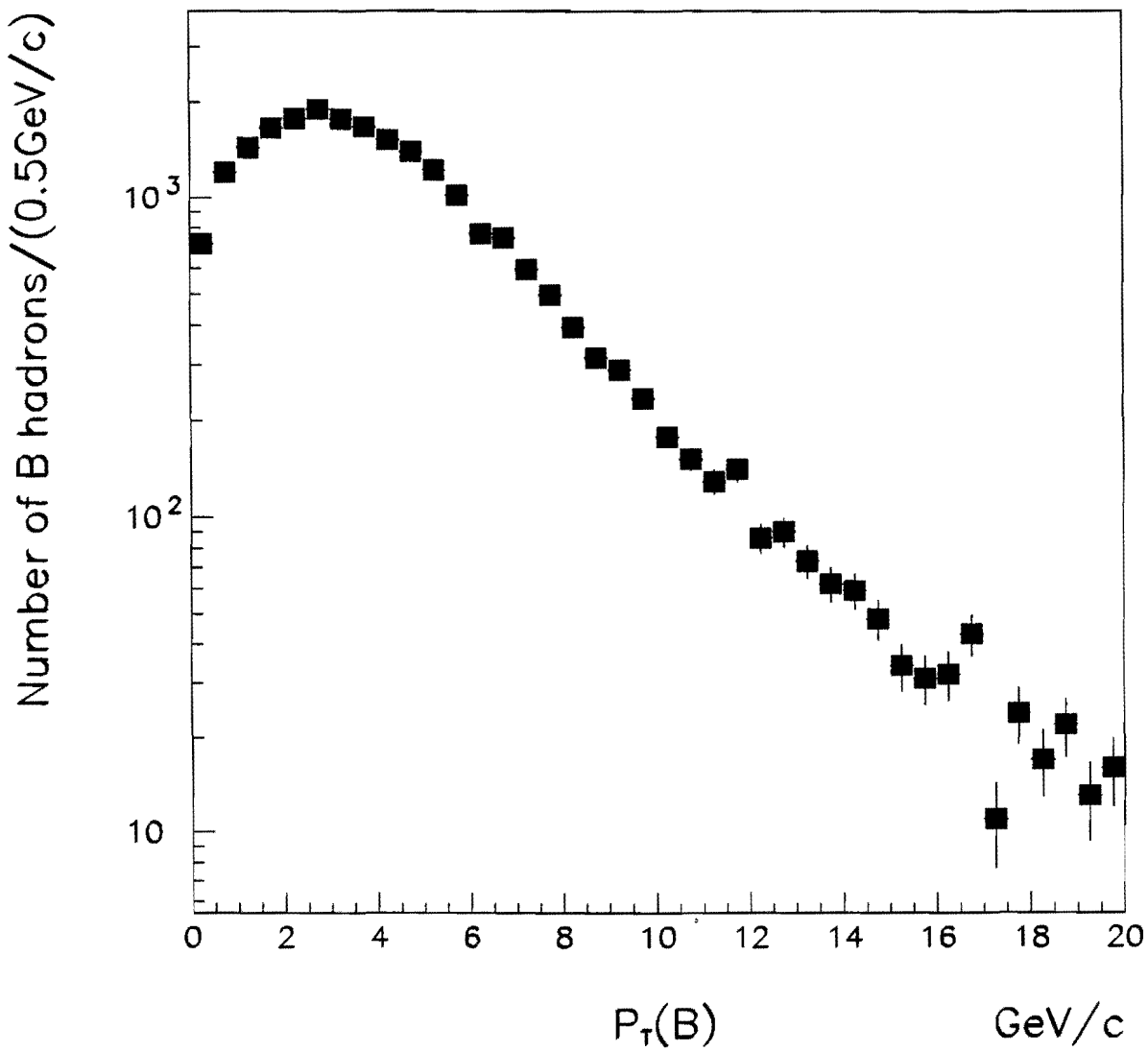

Figure B.4: P_T of B hadron from the fragmentation mapping.

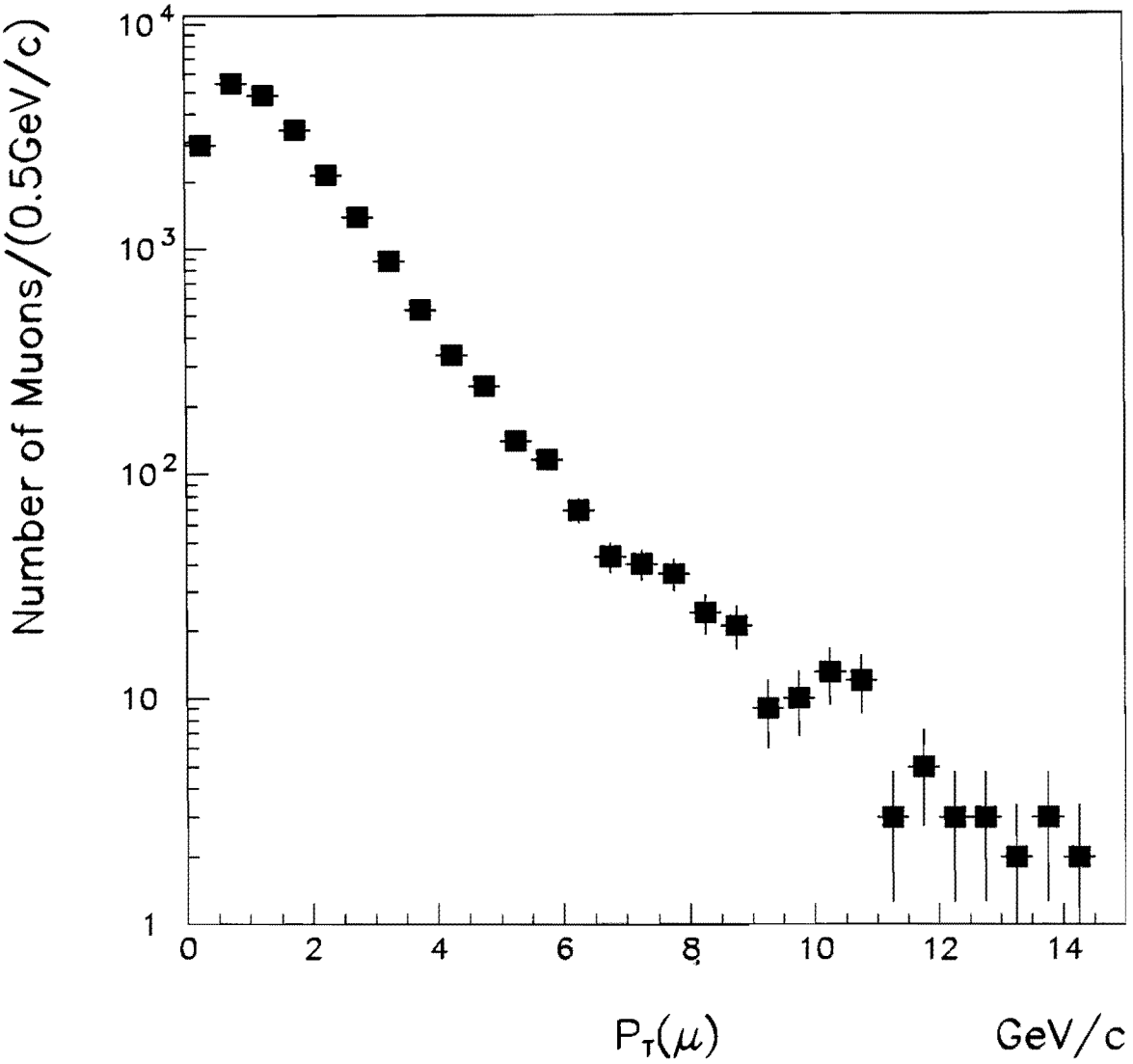

Figure B.5: P_T of muon from the fragmentation and $B \rightarrow \mu$ decay mapping.

In conclusion, only six parameters (or six random seeds) are necessary to create the muon momentum from the b quark momentum. By applying the same mapping generated by the same random seeds to events and counter-events, we expect the jitter to be minimized so that we can get reliable predictions of $\mu - \mu$ correlations from the MNR calculation.

B.3 Result

The predictions of $\mu - \mu$ correlations are given by a model consisting of the MNR calculation on $b\bar{b}$ production and the fragmentation and decay mapping. In the calculation, we use the MRSD0 structure function [81] and renormalization scale $\mu = \mu_0 = \sqrt{m_b^2 + (P_T(b)^2 + P_T(\bar{b})^2)/2}$ with $m_b = 4.75 GeV/c^2$. The Peterson fragmentation parameter $\epsilon = 0.006$ is used for the fragmentation mapping and the CLEO decay package for the decay mapping.

Figure B.6 shows the $\delta\phi$ distribution between b muons and $\bar{b}$ muons with $P_T \geq 3$ GeV/c for both muons. The distribution shows a smaller peak around 0 from gluon splitting process and a larger peak around 180° from the direct production of $b\bar{b}$ quark pair. The $\delta\phi$ distribution after a dimuon mass requirement ($M_{\mu\mu} \geq 5$GeV) is also shown in Figure B.6. We plot the P_T distribution of a bottom muon with the P_T of the other bottom muon greater than 3 GeV/c in Figure B.7.

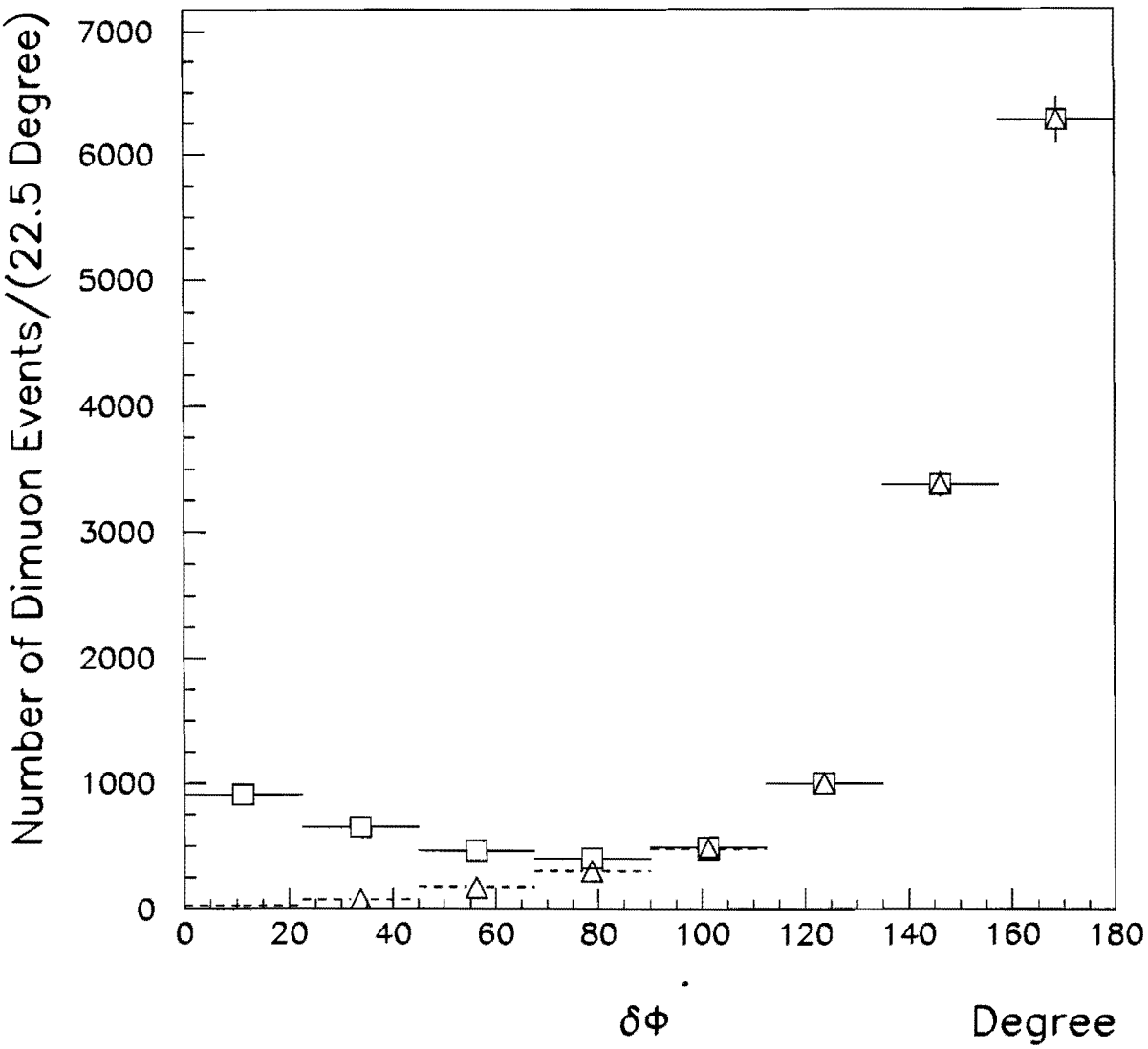

Figure B.6: Opening angle distributions between b muon and $\bar{b}$ muon with $P_T \geq$ 3 GeV/c for both muons. The distribution with $M_{\mu\mu} \geq 5GeV/c^2$ is also shown (triangle).

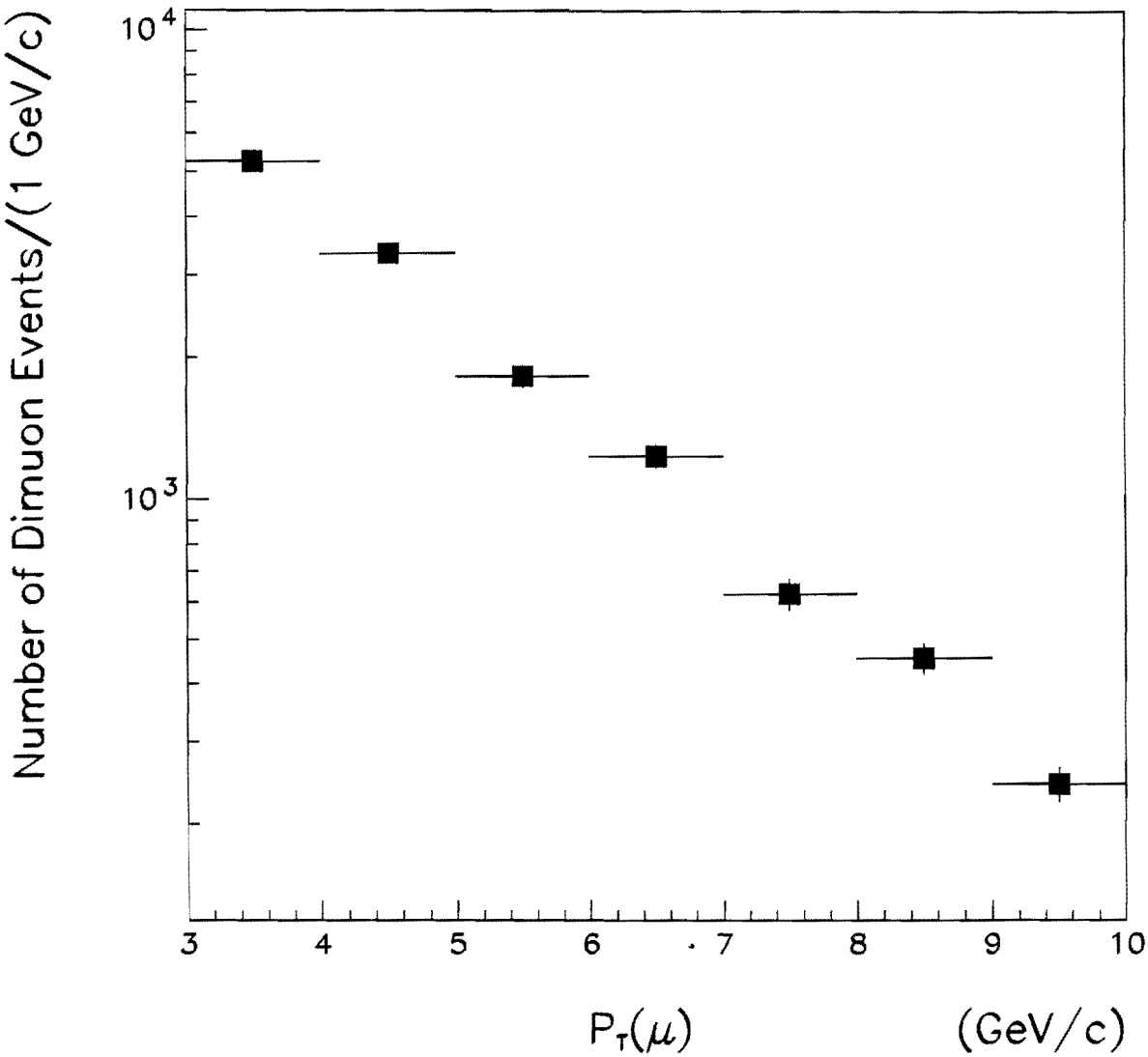

Figure B.7: P_T distribution for bottom muons with P_T of the other bottom muon $\geq$ 3 GeV/c.

Bibliography

[1] S.W. Herb, *et al.* Phys. Rev. Lett. **39**, 252 (1977).

[2] F. Abe, *et al.*, Phys. Rev. Lett. **74**, 2626 (1995).

[3] S. Abachi, *et al.*, Phys. Rev. Lett. **74**, 2632 (1995).

[4] M. Kobayashi and T. Maskawa, Prog. Theor. Phys. **49**, 652 (1973).

[5] M. Mangano, *et al.*, Nucl. Phys. **B373**, 295 (1992).

[6] C. Quigg, *Gauge Theories of the Strong, Weak, and Electromagnetic Interactions*, Addison-Wesley Publishing Company (1993).

[7] S. Glashow, Nucl. Phys. **22**, 579 (1961).

[8] A. Salam, *Weak and Electromagnetic Interactions in Elementary Particle Theory*, W. Svartholm, *ed.*, Almquist and Wiksell, Stockholm (1968).

[9] S. Weinberg, Phys. Rev. Lett. **219**, 1264 (1967).

[10] 't Hooft, Phys. Lett. **37B**, 195 (1971).

[11] G. Arnison, *et al*, Phys. Lett. **122B**, 103 (1983): **126B**, 398 (1983).

[12] J. Collins and D. Soper, Annu. Rev. Nucl. Part. Sci. **35**, 107 (1985).

[13] P. Nason, S. Dawson, and R. K. Ellis, Nucl. Phys. **B327**, 49 (1988).

[14] C. Albajar, *et al.*, Phys. Lett. **256B**, 530 (1991).

[15] F. Abe, *et al.*, submitted to Phys. Rev. D., FERMILAB-PUB-95/289-E.

[16] F. Abe, *et al.*, Phys. Rev. **D50**, 2966 (1994).

[17] L. Wolfenstein, Phys. Rev. Lett. **51**, 1945 (1984).

[18] N. Cabbibo, Phys. Rev. Lett. **10**, 531 (1963).

[19] Particle Data Group, *Review of Particle Properties*, Phys. Rev. **D50**, 1315 (1994).

[20] A. Ali and D. London, CERN-TH-94-7408, Proceedings of the ICHEP94 Conference, Glasgow, Scotland.

[21] D. Buskulic, *et al.*, Phys. Lett. **B322**, 441 (1994).

[22] D. Buskulic, *et al.*, Phys. Lett. **B313**, 498 (1993).

[23] R. Akers, *et al.*, Phys. Lett. **B327**, 441 (1994).

[24] R. Akers, *et al.*, Phys. Lett. **B336**, 585 (1994).

[25] P. Abreu, *et al.*, Phys. Lett. **B338**, 409 (1994).

[26] J. Bartelt, *et al.*, Phys. Rev. Lett. **71**, 1680 (1993).

[27] Particle Data Group, *Review of Particle Properties*, Phys. Rev. **D50**, 1632 (1994).

[28] D. Buskulic, *at al.*, Phys. Lett. **B356**, 409 (1995).

[29] I.I. Biggi, *et al.*, *CP Violation*, C.Jarlskog, *ed.*, World Scientific, Singapore (1989).

[30] A. Pais and S. Treiman, Phys. Rev. **D12**, 2744 (1975).

[31] F. Abe, *et al.*, Nucl. Instrum. Methods A271, 387(1988).

[32] K. M. Ankoviak, 8th Topical Workshop on Proton-Antiproton Collider Physics, 537(1988).

[33] D. Mohl, *et al.*, Physics Reports, C58, 73(1980).

[34] D. Amidei, *et al.*, Nucl. Instrum. Methods A350, 73 (1994).

[35] F. Bedeschi, *et al*, Nucl. Instrum. Methods A268, 51 (1988).

[36] W. Badget, *et al.*, CDF Internal Note 2527, 1994 (unpublished).

[37] L. Balka, *et al*, Nucl. Instrum. Methods A267, 272 (1988).

[38] S. Bertolucci, *et al*, Nucl. Instrum. Methods A267, 301 (1988).

[39] G. Ascoli, *et al.*, Nucl. Instrum. Methods A268, 33 (1988).

[40] J. Chapman, *et al.*,to be submitted to Nucl. Instrum. Methods.

[41] D. Amidei, *et al.*, Nucl. Instrum. Methods A269, 51 (1988).

[42] D. Amidei, *et al.*, IEEE Trans. Nucl. Sci. NS-33, 817 (1988).

[43] P. Billoir, *et al.*, Nucl. Instrum. Methods A241, 115 (1985).

[44] G. Foster, *et al.*, Nucl. Instrum. Methods A269, 93 (1988).

[45] E. Barsotti, *et al.*, Nucl. Instrum. Methods A269, 82 (1988).

[46] N. Amos, *et al.*, Phys. Rev. Lett. **68**, 2433 (1992).

[47] S. Belforte, *et al.*, CDF Internal Note 2535, 1994 (unpublished).

[48] R. Hans, *et al.*, CDF Internal Note 1999, 1993 (unpublished).

[49] Particle Data Group, *Review of Particle Properties*, Phys. Rev. **D50**, 1611 (1994).

[50] S. Henderson, *et al.*, Phys. Rev. **D45**, 2212 (1992).

[51] Particle Data Group, *Review of Particle Properties*, Phys. Rev. **D50**, 1446 (1994).

[52] Particle Data Group, *Review of Particle Properties*, Phys. Rev. **D50**, 1523 (1994).

[53] Particle Data Group, *Review of Particle Properties*, Phys. Rev. **D50**, 1356 (1994).

[54] Particle Data Group, *Review of Particle Properties*, Phys. Rev. **D50**, 1662 (1994).

[55] Particle Data Group, *Review of Particle Properties*, Phys. Rev. **D50**, 1573 (1994).

[56] V. Barger and R. Philips, *Collider Physics*, Addision-Wesley Publishing Company (1988).

[57] F. Abe, *et al.*, Phys. Rev. Lett. **67**, 3351 (1991).

[58] D. Frei, CDF Internal Note 1430, 1991 (unpublished).

[59] F. Paige and S.D. Protopopescu, BNL Report No. 38034, 1986 (unpublished).

[60] C. Peterson, *et al.*, Phys. Rev. **D27**, 105 (1983).

[61] J. Chrin, Z. Phys. **C36**, 165 (1987).

[62] P. Avery, *et al.*, Cornell Internal Note CSN-212, 1985 (unpublished).

[63] G. Sganos, private note *Tutorial on CDFSIM*, 1992 (unpublished).

[64] F. Abe, *et al.*, Phys. Rev. Lett. **67**, 3351 (1991).

[65] Particle Data Group, *Review of Particle Properties*, Phys. Rev. **D50**, 1582 (1994).

[66] Particle Data Group, *Review of Particle Properties*, Phys. Rev. **D50**, 1572 (1994).

[67] Particle Data Group, *Review of Particle Properties*, Phys. Rev. **D50**, 1596 (1994).

[68] Particle Data Group, *Review of Particle Properties*, Phys. Rev. **D50**, 1783 (1994).

[69] R. Hollerbeek, MKII Note, *Distance of Closest Approach Distributions for Vertex Studies*, 1982 (unpublished).

[70] H. Wenzel, CDF Internal Note 1924, 1993 (unpublished).

[71] P. Derwent, CDF Internal Note 2188, 1994 (unpublished).

[72] F. Abe, *et al.*, Phys. Rev. **D50**, 2966 (1994).

[73] P. Straub, *et al.*, Phys. Rev. **D45**, 3030 (1992).

[74] F. James and M. Ross, CERN Preprint, CERN-D506 (1989).

[75] Particle Data Group, *Review of Particle Properties*, Phys. Rev. **D50**, 1534 (1994).

[76] T. Huffman, CDF Internal Note 1822, 1992 (unpublished).

[77] S. Denisov, *at al.*, Nucl. Phys. **B61:62** (1973).

[78] A. Canner, *et al.*, CDF Internal Note 2363, 1993 (unpublished).

[79] T. Lecompte, *et al.*, CDF Internal Note 2700, 1994 (unpublished).

[80] C. Anway-Wiese, *et al.*, CDF Internal Note 1986, 1993 (unpublished).

[81] A. D. Martin, R. G. Roberts, and W. J. Sterling, RAL-92-021 (1992).

[82] M. Mangano, CERN-TH-95-191, Proceedings of the 6th International Symposium on Heavy Flavor Physics, Pisa, Italy.

[83] F. Abe, *et al.*, Phys. Rev. Lett. **67**, 3351 (1991).

[84] C. Albajar, *et al.*, Phys. Lett. **B262**, 171(1991).

[85] P. Acton, *et al.*, Phys. Lett. **B276**, 379(1992).

[86] B. Adeva, *et al.*, Phys. Lett. **B288**, 395(1992).

[87] P. Abreu, *et al.*, Phys. Lett. **B301**, 145(1993).

[88] Particle Data Group, *Review of Particle Properties*, Phys. Rev. **D50**, 1632 (1994).

[89] Particle Data Group, *Review of Particle Properties*, Phys. Rev. **D50**, 1640 (1994).